Title
Image-guided therapeutic intervention in autoimmune diseases

Author
Chen, Bao Ying

Publication Date
2022

UNIVERSITY OF CALIFORNIA

Los Angeles

Image-guided therapeutic intervention in autoimmune diseases

A dissertation submitted in partial satisfaction of the
requirements for the degree Doctor of Philosophy in
Physics and Biology in Medicine

by

Bao Ying Chen

2022

ABSTRACT OF THE DISSERTATION

Image-guided therapeutic intervention in autoimmune diseases

by

Bao Ying Chen
Doctor of Philosophy in Physics and Biology in Medicine
University of California Los Angeles, 2022
Professor Peter M. Clark, Chair

Multiple sclerosis (MS) affects more than 1 million Americans every year and is a chronic, demyelinating, neurodegenerative disease of the central nervous system. MS is a challenging disease to diagnose and treat as it can be a heterogenous in both its biological aspects and clinical presentation. Standard of care for diagnosing patients with MS is through the use of magnetic resonance imaging (MRI). While this technique is informative about anatomical structures, an imaging modality that can provide functional information about the disease will help to elucidate the complex mechanisms involved. Furthermore, current therapies for MS can have significant side effects on patients and/or only target a certain subset of patients. New therapies are needed to not only help MS patients but also patients with other autoimmune diseases.

Chapter one of this dissertation will be a review about the current state of MS, introduction into positron emission tomography (PET) and the current radiotracers that have been

developed to image different aspects of MS, and the deoxyribonucleoside salvage pathway in autoimmunity.

Chapter two describes the first project that I worked on in which I utilize [^{18}F]FAC to image brain-infiltrating leukocytes in the experimental autoimmune encephalomyelitis (EAE), a mouse model of MS. Brain-filtrating leukocytes contributes to MS pathology and have been shown to contribute to pathology in other neurological diseases including autoimmune encephalomyelitis. Because of its role in disease pathology, it is of importance that a strategy is available to image these pathogenic immune cells.

Chapter three will talk about understanding the functional aspect of the deoxyribonucleoside salvage in EAE and the broader implications of this pathway for MS disease. Through our previous work on imaging this pathway in EAE, we found that this pathway is upregulated during disease onset and progression. I show that in this chapter the deoxyribonucleoside salvage is functionally-relevant for EAE and that specifically targeting this pathway in EAE leads to improvement of clinical symptoms in MS. Discoveries made here can be translated into understanding and developing therapies for other autoimmune diseases. The result of this work demonstrates the potential of targeting the deoxyribonucleoside salvage in autoimmune diseases and the success of this target in MS mouse models support further evaluation into the clinical for patients with autoimmune diseases.

In chapter 4, I draw conclusions to my work during this PhD and in chapter 5, I highlight some of the works that I have contributed to during my time at UCLA.

The dissertation of Bao Ying Chen is approved.

Harvey R. Herschman

Allan Mackenzie-Graham

Oluwatayo Ikotun

Peter M. Clark, Committee Chair

University of California, Los Angeles

2022

I dedicate this dissertation to my loving and supportive parents who made the choices and sacrifices to ensure that my siblings and I would have a better future. I would like to also dedicate this to my siblings, Andrew and Clara, and my husband Moe, for all their love and support throughout this process.

Table of Contents

LIST OF FIGURES

LIST OF TABLES

ACKNOWLEDGEMENTS

First, I would like to thank my mentor, Dr. Peter Clark, for all his patience and mentorship throughout my graduate school experience. Peter graciously accepted me into his lab when I first started my graduate school in 2016 despite my lack of knowledge and experience in PET imaging, autoimmunity, and basically everything science-related. Working with Peter and the lab not only helped me to acquire the technical science skills, but also has shaped the way that I think, write, and communicate my science. I am forever grateful to Peter for taking time out of his day to help me improve my science, my writing skills, communication skills, and to let me know of opportunities. I am always thankful that I can go to Peter for help whenever I feel I am stuck on a science question or am stuck troubleshooting an experiment. If it was not for Peter and his mentorship, I don't think I would have had the opportunities that I did and be where I am in my professional life today. I am forever grateful that Peter have and always will continue to instill a love for science into his trainees.

I am also thankful to have such a great thesis committee to help me during my graduate studies. Dr. Harvey Herschman, Dr. Allan Mackenzie-Graham, and Dr. Tayo Ikotun. Going through those presentations can be terrifying but the experiences have been so much more meaningful and fun because of you guys.

I would also like to thank my lab members for their support throughout my PhD. While the lab was always growing and evolving, it was through this experience that I was able to meet many wonderful and extremely smart people in science. I would like to thank Dr. Chiara Ghezzi for her technical and emotional support when she was working in the lab as a project scientist. There were so many times when I did not know what I was doing and her knowledge and experience definitely saved me from falling. I would also like to thank Jess, Stefani, Alyssa, and Evelyn for their support. Sometimes, experiments can be long and having them in the lab during those times made it easier to finish. I also really appreciate their optimism and their spirit for adventures. It is rare to find a team of people who can get along with each other. I am grateful to have had such a great lab to work with during my time in my PhD.

During my time at Crump, I also made many friends who have had a positive impact on my graduate school experience. Ksenia, Jia, and Philip from the van Dam lab. I really enjoyed going to conferences together and going on the next food adventure in the San Gabriel Valley. Their support has been immense and they let me tag along in their lab outings and adventures. I would also like to thank Gaoyuan, Ray, and Jay from the Murphy lab. Not only did they always answer my chemistry questions but also always gave me great advice about graduate school and life. I'd also like to thank Arely and Kaitlin from the Ikotun lab for their continuous support. While they are always busy with an experiment, I really appreciate that they take time out of their day to say hi. Also, I would like to thank Felix Bergara from the Wu lab. He taught me a lot of techniques during my time at Crump and he is also the reason why I was able to get a postdoc position at Dr. Anna Wu's lab. I am forever grateful for having the opportunity to learn from Felix and am looking forward to working with him in the Wu lab at City of Hope. At the imaging center, I'd like to thank Charles, Dishan, and Mikayla for their support. I never really knew what Charles was up to but he was always the person I went for life/science advice because he just seemed to know and do everything. Dishan and Mikayla were really supportive during my imaging studies. Those days are really stressful and their priority to make help make that time as least stressful as possible is something I am always thankful for. It was also so nice to drink coffee with them and chat about everything with them. I would also like to thank Brendon Villegas for all his support and help throughout my PhD as he was not only a graduate of PBM but he also worked on PET imaging. I am forever grateful for the time he took out of his day to give me advice on how to navigate graduate school, teach me how to do autoradiography, and how to design my experiments. I'd also like to thank Arion, Mike, Tayo, and Shili for all the advice they have given me throughout my graduate studies.

I would like to also thank those who were not in the Crump Institute but were really supportive during my time in graduate school. I am extremely grateful to my PBM friends, Nyasha and Fadil, for their continued love, support, and laughter throughout our graduate studies, especially when the pandemic first started. I would also like to thank members of the JCCC Flow core facility, Miriam, Salem, Iris, and Zoran. While I was not always the best user and didn't always know what I was doing, I really appreciate the time and patience they put into helping me. I would also like to thank all of my collaborators who I had the opportunity to learn from. Having the chance to collaborate with you guys was a great learning experience and it has definitely made my graduate experience more fun. I am also thankful to my middle school best friend, Susan for her support and finally visiting me in mainland America after asking her to visit me for the past 10 years.

I would like to thank the UCLA service workers and department staff for all of their hard work in making sure that operations are running smoothly at UCLA. Thank you to Kerry, Hoff, and Pierre for always helping out with package deliveries and autoclaving. I'd also like to thank Jorge and Karen for their help in approving and ordering supplies. I thank Emily Fitch for always helping me with administrative paperwork related to my graduate studies and for organizing really fun pharmacology retreats for the whole department. Furthermore, thank you Dr. McNitt-Gray for always being so kind and supportive to the students of PBM. Thank you to Alondra and Reth for their administrative support on the PBM side.

Lastly, I want to thank my family for their endless love and support throughout my time in graduate school. It was not always easy to explain to my parents what graduate school is or even what is a PhD but I am forever grateful that, at the end of the day, they continue to support me and always called me to tell me to remember to eat and get some rest. I am forever grateful for the sacrifices they made for my siblings and I to ensure that we have better opportunities for our futures. Because of my parents, I learned the meaning of perseverance, hard work, being responsible, and respecting others around you. I thank my siblings for being spontaneous and always keeping the laughter going whether it be on text, over the phone, or whenever I visited Hawaii. Last but not least, I want to thank my husband, Moe, for all of his friendship, love, support, and laughter throughout this journey.

VITA

Education

March 2022	PhD (expected), Physics and Biology in Medicine, UCLA
May 2014	BA, Biological Chemistry, Grinnell College

Award and fellowships

2020	Young Investigator Award Finalist, WMIC
2020	Women in Molecular Imaging Scholar Award, WMIC
2020	Brain Research Institute Knaub Fellowship in Multiple Sclerosis, UCLA
2019	Women in Molecular Imaging Scholar Award, WMIC
2019	World Molecular Imaging Travel Award, WMIC
2016-2020	Eugene V. Cota-Robles Fellowship

Peer-reviewed publications

Chen BY, Ghezzi C, Villegas B, et al. ^{18}F-FAC PET Visualizes Brain-Infiltrating Leukocytes in a Mouse Model of Multiple Sclerosis. J Nucl Med. 2020;61(5):757-763.

Fajardo VM, Feng I, Chen BY, et al. GLUT1 overexpression enhances glucose metabolism and promotes neonatal heart regeneration. Sci Rep. 2021;11(1):8669.

Lisova K, Chen BY, Wang J, Fong KMM, Clark PM, van Dam RM. Rapid, efficient, and economical synthesis of PET tracers in a droplet microreactor: application to O-(2-[^{18}F]fluoroethyl)-L-tyrosine ([^{18}F]FET). EJNMMI Radiopharm Chem. 2019;5(1):1.

Ghezzi C, Wong A, Chen BY, Ribalet B, Damoiseaux R, Clark PM. A high-throughput screen identifies that CDK7 activates glucose consumption in lung cancer cells. Nat Commun. 2019;10(1):5444.

Salas JR, Chen BY, Wong A, et al. ^{18}F-FAC PET Selectively Images Liver-Infiltrating CD4 and CD8 T Cells in a Mouse Model of Autoimmune Hepatitis. J Nucl Med. 2018;59(10):1616-1623.

Salas JR, Chen BY, Wong A, et al. Noninvasive Imaging of Drug-Induced Liver Injury with ^{18}F-DFA PET. J Nucl Med. 2018;59(8):1308-1315.

Oral presentations

Chen BY, Clark PM. Targeting metabolic vulnerabilities in autoimmune diseases UCLA Department of Molecular and Medical Pharmacology Retreat (2021). Santa Monica, CA.

Chen BY, Clark PM. [^{18}F]FAC PET can image immune activation and reveals potential functional role of deoxyribonucleoside salvage pathway in EAE mouse model of MS. World Molecular Imaging Congress (2020). Virtual, CA.

Chen BY, Clark PM. Non-invasive imaging of brain-infiltrating leukocytes using Positron Emission Tomography (PET). World Molecular Imaging Congress: Workshop: Inflammation, Immunology, and Infection (2019). Montreal, Canada.

Chen BY, Clark PM. Non-invasive imaging of brain-infiltrating leukocytes using Positron Emission Tomography (PET). World Molecular Imaging Congress (2019). Montreal, Canada.

Chen BY, Clark PM. Non-invasive imaging of brain-infiltrating leukocytes using Positron Emission Tomography (PET). Crump Institute for Molecular Imaging (2019). Los Angeles, CA.

Poster presentations

Chen BY, Clark PM. Targeting deoxycytidine kinase improves clinical symptoms in models of multiple sclerosis. UCLA Stem Cell Symposium (2022). Virtual, CA.

Chen BY, Clark PM. [^{18}F]FAC PET images immune activation in a B cell dependent model of multiple sclerosis mouse model. World Molecular Imaging Congress (2021). Virtual, CA.

Chen BY, Clark PM. Non-invasive PET Imaging of Brain-infiltrating Lymphocytes in Experimental Autoimmune encephalomyelitis (EAE), a Mouse Model of Multiple Sclerosis. UCLA Stem Cell Symposium (2020). Los Angeles, CA.

Chen BY, Clark PM. Non-invasive PET Imaging of Brain-infiltrating Lymphocytes in Experimental Autoimmune encephalomyelitis (EAE), a Mouse Model of Multiple Sclerosis. UCLA Department of Molecular and Medical Pharmacology Retreat (2018). Huntington Beach, CA.

Chen BY, Clark PM. Non-invasive monitoring of stem cell derived human hepatocyte homing and engraftment in vivo using PET (2018). Los Angeles, CA.

Chen BY, Clark PM. [^{18}F]FAC and [^{18}F]DFA can be used to quantify hepatic infiltrating lymphocytes and hepatocellular function in a preclinical mouse model of autoimmune hepatitis UCLA Department of Molecular and Medical Pharmacology Retreat (2017). Huntington Beach, CA.

Chapter 1: Introduction

1.1 Overview of multiple sclerosis (MS)

1.1.1 **Epidemiology of MS**

Multiple sclerosis (MS) affects over a million people in the United States (*1*) and over 2.3 million people around the world (**Fig. 1.1**) and has an onset of between 20-40 years old ((*2*,*3*)). This disease is characterized demyelination and neurodegeneration in the central nervous system. MS can lead to lifelong symptoms including physical disability, cognitive impairment, and a decrease in the quality of life. Factors that lead to an increase risk of MS includes environmental, lifestyle, and genetics. In studies where the prevalence of MS is mapped out, it has been suggested that MS prevalence increases with increasing latitude(*4*). Individuals of European descent are more prone to having MS (*5*).

Several factors can contribute to MS. For example, the presence of HLA-DR1*15:01 allele is one of the genetic factors most associated with MS (*6*). Childhood obesity, cigarette smoking, and previous infection with Epstein-Barr virus have all been associated with increased risk of MS (*7–9*) (**Table 1**).

MS is more prevalent in females than males (*2*). females with MS are more likely to have a better prognosis than males and their disease severity tends to be lower. For example, females diagnosed with remitting-relapsing MS have less severe of MS when compared to males, with longer time to reach severe disability. based on the expanded disability status scale criteria or secondary progressive MS (*10*,*11*).

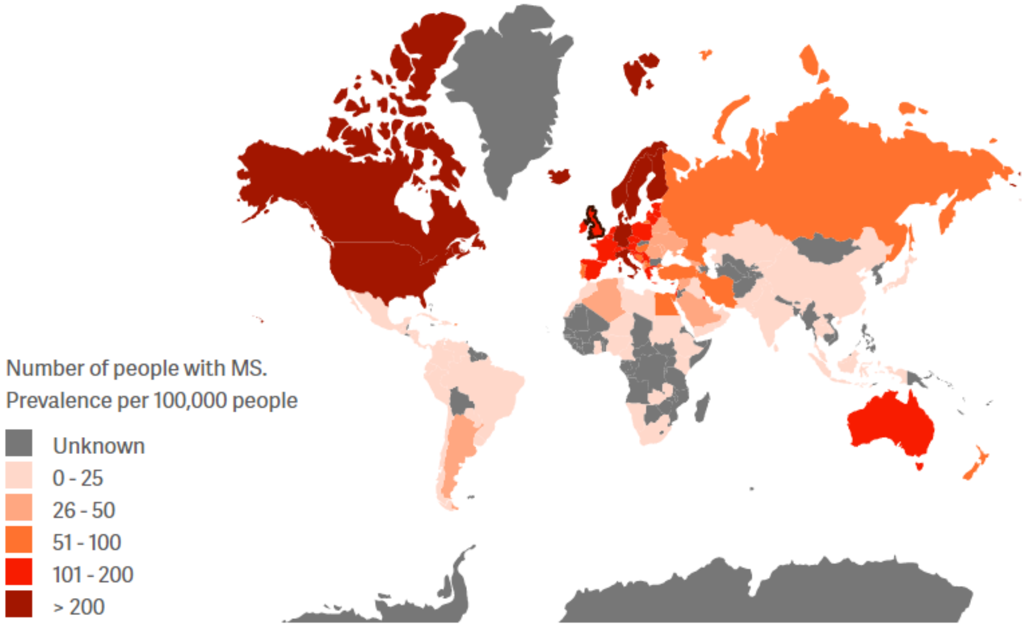

Figure 1.1. Prevalence of MS worldwide.
The MS international Federation’s Atlas of MS. 2013.

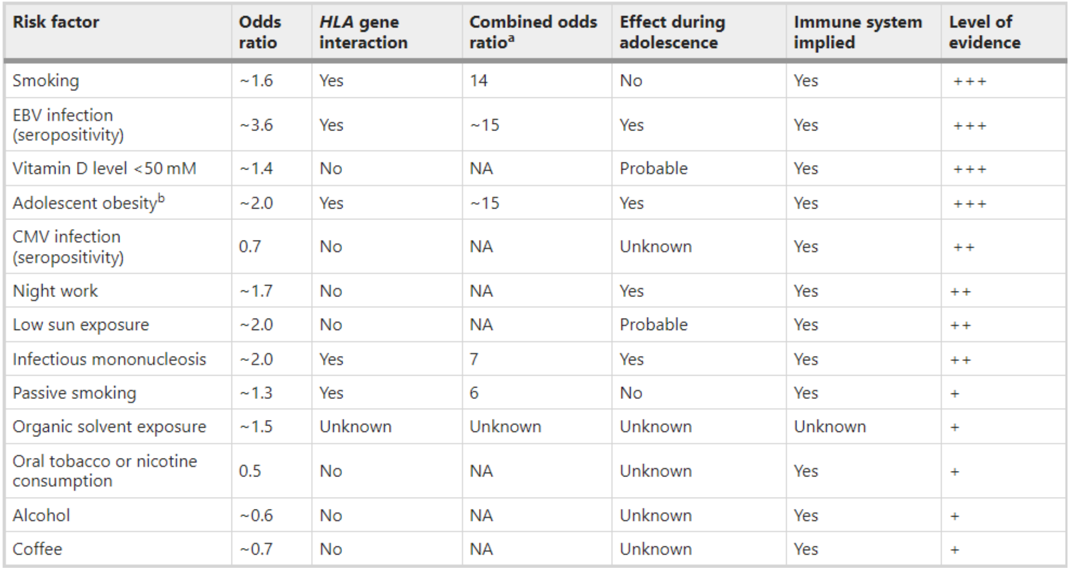

Risk factor	Odds ratio	*HLA* gene interaction	Combined odds ratio[a]	Effect during adolescence	Immune system implied	Level of evidence
Smoking	~1.6	Yes	14	No	Yes	+++
EBV infection (seropositivity)	~3.6	Yes	~15	Yes	Yes	+++
Vitamin D level <50 mM	~1.4	No	NA	Probable	Yes	+++
Adolescent obesity[b]	~2.0	Yes	~15	Yes	Yes	+++
CMV infection (seropositivity)	0.7	No	NA	Unknown	Yes	++
Night work	~1.7	No	NA	Yes	Yes	++
Low sun exposure	~2.0	No	NA	Probable	Yes	++
Infectious mononucleosis	~2.0	Yes	7	Yes	Yes	++
Passive smoking	~1.3	Yes	6	No	Yes	+
Organic solvent exposure	~1.5	Unknown	Unknown	Unknown	Unknown	+
Oral tobacco or nicotine consumption	0.5	No	NA	Unknown	Yes	+
Alcohol	~0.6	No	NA	Unknown	Yes	+
Coffee	~0.7	No	NA	Unknown	Yes	+

Table 1. Lifestyle and environmental risk factors for MS.

1.1.2 **Types of MS**

Clinically, MS is displayed in patients in two forms: relapsing or progressive. The relapsing form of MS (RRMS) is characterized by discrete episodes of neurological dysfunction followed by complete, partial, or no remission. Relapses can occur and these relapsing episodes can last for over days or weeks, reach peak severity, and remit either to some recovery or complete recovery (*12*). Typically, most MS patients present with a relapsing-remitting course of disease and, eventually, about 50% of those patients will develop the secondary, progressive form of MS (SPMS). However, in 15% of MS cases, patients will present a primary progressive course (PPMS) in which neurological dysfunctions continually get worse with time and with no remission (*13*). Some patients will present clinical isolated symptoms (CIS), in which a single episode of MS-like symptoms will appear but is unclear whether those symptoms will happen again. Figure 1.2 shows an overview of the clinical course for MS disease. The length of disease and the timing of relapses can vary between patients.

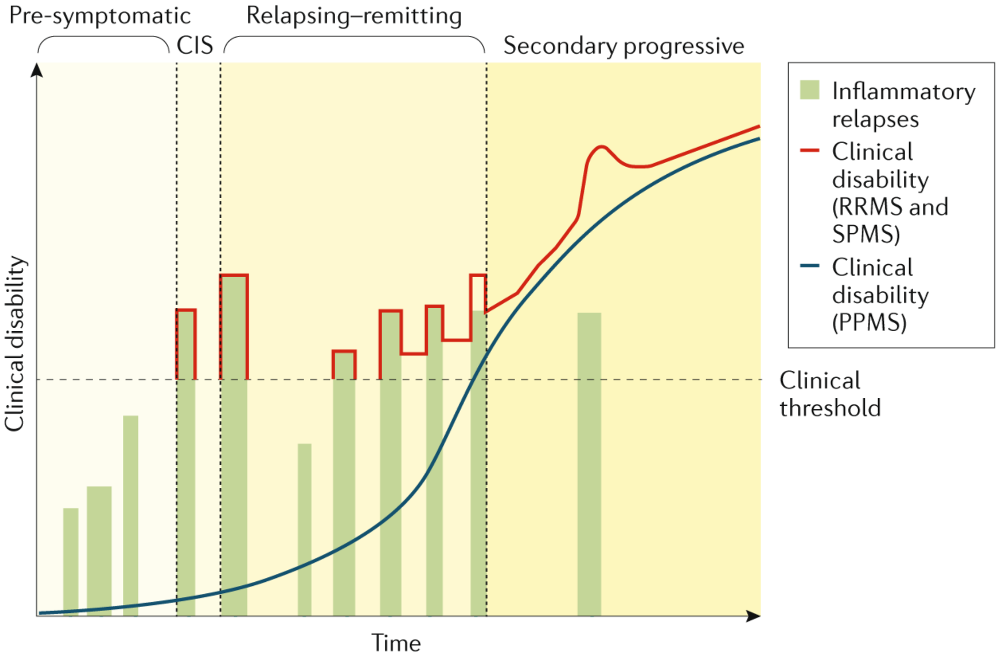

Figure 1.2. Clinical course of MS: relapsing-remitting (RRMS), secondary progressive MS (SPMS), primary progressive MS (PPMS), and progressive-relapsing MS (PRMS) Clinically isolated symptoms (CIS) (*13*).

1.1.3 **Clinical presentation of MS**

The clinical symptoms of MS are often heterogenous and can depend on the location of the demyelinating lesions in the central nervous system and the severity of the lesions. Onset of MS is defined as an episode of neurological dysfunction due to demyelination areas in the central nervous system (such as the optic nerve, spinal cord, and brain). Optic neuritis, one of the first symptoms experienced by over 25% of MS patients, is characterized by either partial or complete vision loss, loss of color vision, or eye pain (*14–16*). Other symptoms that can also arise with initial MS onset include sensory symptoms (such as numbness and pinks-and-needles feeling), motor symptoms (e.g. muscular weakness and spasticity), and cognitive impairment.

Focal plaques are a standard MS phenotype, characterized as demyelination. These plaques can occur in white and gray matter and can be found throughout the brain, optic nerve, and spinal cord (*17–19*). In early stages of MS, active demyelinating lesions, defined as significant leukocyte infiltration, activated microglia and macrophages, and reactive astrocytes, are present in patients with CIS or RRMS. In contrast, PPMS or SPMS patients have more inactive lesions that are better-defined, less densely populated by infiltrating immune cells, less dense axons, astrocytic gliosis, inconsistent microglial activation (*20–24*). Other forms of plaques can also exist in MS including chronic active plaques and slow expanding lesions. Chronic plaques tend to be more frequent in MS patients with longer disease course and can be characterized by more macrophages at the edge rather than the center of the lesion (**Fig. 3**). Slower-expanding plaques have an inactive center containing demyelination and transected axons (*20*,*22–24*).

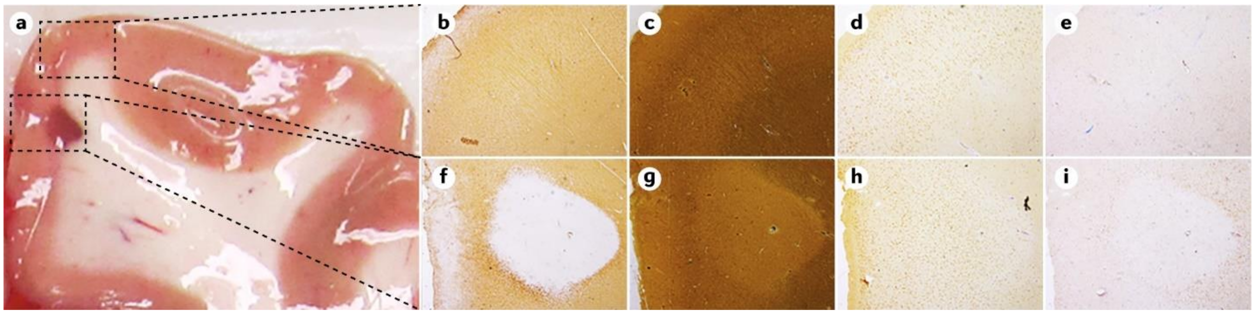

Figure 1.3. Brain tissue of MS patient with secondary progressive multiple sclerosis (*25*).

(A) Top box: normal- appearing grey and white matter. Lower box: mixed grey and white matter lesions. (B)- (E): sections stained of normal appearing grey and white matter. (F)-(I): sections stained from grey and white matter lesions. (B and F): Proteolipid protein staining to quantify myelin, (C and G): Bielchowsky staining to determine axonal injury. (D and H): NeuN staining to identify neuronal shrinkage and loss. (E and I): ionized calcium binding receptor molecule 1, a marker for microglia.

1.1.4 **Immunobiology of MS**

MS is an autoimmune disease characterized by an immune attack on healthy tissues and cells in the central nervous system. Hallmarks of the MS disease includes demyelination in areas located around post-capillary venules, axonal loss leading to neurodegeneration, and breakdown of the blood-brain barrier. The mechanisms of how the blood brain barrier is broken down are not well-understood, but studies suggest that proinflammatory cytokines and chemokines from residential immune cells, endothelial cells, as well as the cytokine-dependent and chemokine-dependent leukocyte mediated injury may have some effects on the breakdown of the blood brain barrier (*4*,*5*). Post-breakdown of the blood-brain barrier leads to migration of infiltrating activated-leukocytes into the central nervous system, causing further inflammation and demyelination and eventual oligodendrocyte loss, reactive gliosis, and axonal degeneration (*28*,*29*).

The traditional understanding of MS is that it is a T-cell mediated disease, but current understanding includes the involvement of several different immune types including B cells, T cells, myeloid cells, microglia, and (*30*). Immune cells in the periphery and resident- immune cells in the CNS secrete pro-inflammatory cytokines to recruit inflammatory cells into the CNS. This leads to inflammation and demyelination in the CNS. Residential innate immune cells, microglial cells and astrocytes, can release neurotoxic inflammatory cytokines that promote axonal damage and neurodegeneration in MS disease (*31*). It is also thought that aberrant T cell activation during MS is also due to an insufficiency in regulatory T cell functions in which regulatory T cells become effector-like T cells with loss of function (*32*). Due to success in therapies against CD20+

B cells in MS, a role for B cells in development of MS has been implicated (*33*). While patients treated with CD20 therapy showed reduced relapse rate, no differences in B cell produced immunoglobulin profiles in the cerebrospinal fluid were observed in these patients (*34*,*35*), psuggesting that MS relapses do not depend on B cell-produced antibodies. However, patients treated with anti-CD20 therapy have reduced pro-inflammatory responses and B cells that reemerge after discontinuing the therapy have a more anti-inflammatory profile including increased IL-10 secretion which is a regulatory cytokine (*36*–*38*).

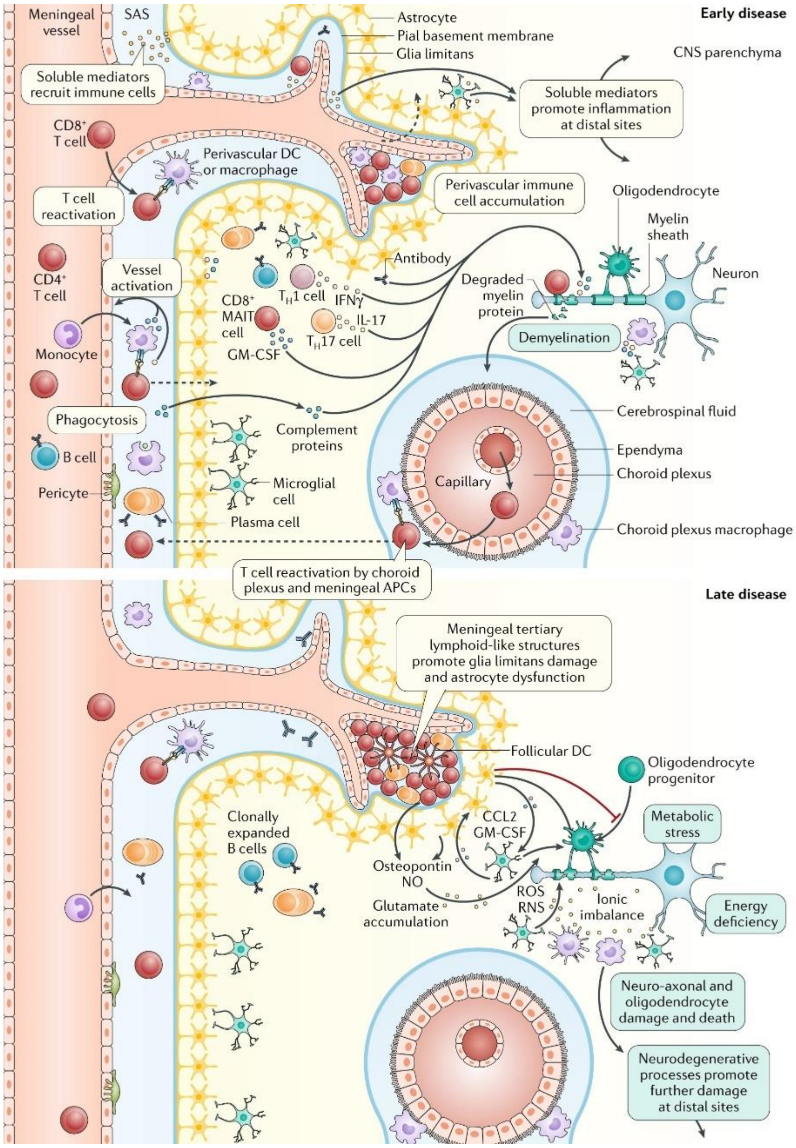

Figure 1.4. Complex immune system regulation in early and late stages of MS within the central nervous system (*25*).

Most recently, Epstein-Barr virus (EBV has been thought to play an important role in priming the immune system to attack the central nervous system, leading to the development of MS.. Anti-EBV antibody titers in 99% of MS patients suggestsan epidemiological link between MS and EBV. A longitudinal study comprising of more than 10 million young adults in the US military active duty found nearly 955 individuals who were diagnosed with MS during their period of service. These individuals had increased levels of neurofilament light chain, a biomarker for neuroaxonal degeneration and that was only after infection with EBV and not with other viruses (*39*). A more recent study found that EBNA1 protein of the Epstein-Barr virus mimics the GlialCAM protein, that is expressed on glial cell adhesion molecules (*40*). A part of the EBV protein mimics the host protein, GlialCAM, that is found in insulating sheath on nerves. As a result of this molecular mimicry, immune cells that attacking the EBV virus to clear it out of the body, also end up targeting the GlialCAM cells in the myelin (*40*).

1.1.5 **Current standard of care for MS diagnosis**

Current clinical practice to diagnose MS uses 2017 McDonald Criteria. In these criteria, the main evidence needed to distinguish MS from other neurological conditions is assessing central nervous system damage that has been disseminated in time and space. In other words, if damage in the CNS happened across different dates and time, then that will differentiate MS from other conditions. Details on the specifics of the diagnostic criteria for MS are compiled below (Table 2).

Current standard of care for diagnosing MS and monitoring the course of the disease is through MRI. Abnormal lesions as identified through MRI in patients with MS usually appear multifocal and egg-shaped on T-2 weighted images. Gadolinium-based contrast agents and acquiring T1-weighted images can be used to distinguish active from inactive lesions. Hypointense lesions on T-1 weighted images are associated with more severe tissue damage; this hypointensity may indicate demyelination and axonal loss (*41*).

The 2017 revised criteria for the diagnosis of MS
Relapsing–remitting MS
• At least two clinical relapses and objective clinical evidence on neurological examination of at least two lesions with distinct anatomical location, or at least two clinical relapses and objective clinical evidence of one lesion and clear-cut historical evidence of a prior relapse involving a lesion in a distinct anatomic location
• At least two clinical relapses and objective clinical evidence of one lesion; in addition, dissemination in space should be demonstrated by either a second clinical relapse implicating a different central nervous system site or using MRI.
• One clinical relapse and objective clinical evidence of two or more lesions; in addition, dissemination in time should be demonstrated by a second clinical relapse, or using MRI or demonstration of cerebrospinal fluid-specific oligoclonal bands.
• One clinical relapse and objective clinical evidence of one lesion; in addition, dissemination in space should be demonstrated by a second clinical relapse implicating a different central nervous system site or using MRI, whereas dissemination in time should be demonstrated by a second clinical relapse, or using MRI or demonstration of cerebrospinal fluid-specific oligoclonal bands.
Primary progressive MS
• A disease course characterized by progression from onset, 1 year of disability progression (retrospectively or prospectively determined) independent of clinical relapse and two of the following criteria below:
o One or more T2-hyperintense lesions in at least one area in the brain characteristic of MS (periventricular, cortical and/or juxtacortical or infratentorial)
o Two or more T2-hyperintense lesions in the spinal cord with no distinction between symptomatic or asymptomatic lesions
o Demonstration of cerebrospinal fluid-specific OCBs

Table 2. 2017 McDonald Criteria for MS diagnosis (*25*).

1.1.6 **Current therapies used to treat MS patients**

Disease-modifying treatments (DMTs) are usually prescribed once a patient is diagnosed with RRMS or CIS to help reduce the risk of disease progression. The first-line of DMTs include IFN-beta and glatiramer acetate. IFN-beta is thought to activate the STAT transcription factors and modulate the immune system through downregulating major histocompatibility complex (MHC) expression and block T cell migration (*42*). Glatiramer acetate can induce anti-inflammatory T cell responses (*43*). These DMTs have low risk for severe adverse drug reactions, but are only moderately effective and often have poor tolerability. Patients often develop flu-like symptoms and injection site inflammation.

The treatment strategy for RRMS is to use escalation therapy in which patients are first given safe but moderately effective therapies such as IFN-beta and glatiramer acetate. If the patient is not able to tolerate the first line of therapy, then another form of first-line of DMT is given such as fingolimod. If new relapses occur or new lesions are present in a MRI scan, then second and third-line therapies are used (*44*). Patients who no longer respond to therapy and have more severe disease will be given an autologous hematopoietic stem cell transplant (*45*).

Another treatment strategy to help patients with RRMS is induction therapy in which patients are treated earlier with more effective DMTs such as alemtuzumab (binds to CD52 to prevent lymphocytes from circulating in the periphery) and ocrelizumab (anti-CD20 therapy that depletes circulating B cells) to help prevent severe CNS damage and clinical disability. This approach is often given to patients who have a negative prognosis and are likely to have high disease activity and frequent relapses. While this therapeutic approach can rapidly eradicate cells associated with inflammation in MS and possibly shift towards a more tolerogenic immune system, DMTs used here have more adverse side effects that include respiratory infections, malignancy, and decreased number of platelets (*46*). The same DMTs used for patients with RRMS cannot be used for patients who have PPMS and SPMS, as most of those therapies are not effective. So far, only anti-CD20 therapies such as Rituximab have shown some promise in reducing signs of active inflammation in younger patients and reduced disability progression in PPMS patients.

1.2 Positron Emission Tomography (PET) imaging of autoimmunity

1.2.1 **Introduction to PET**

Positron emission tomography (PET) is a qualitative, non-invasive imaging modality that images biological processes *in vivo*. Molecules are radiolabeled with a positron emitting radioisotope, such as fluoride-18 (F-18), emitting positrons that can travel short distances and interact with a neighboring electron. This interaction leads to the generation of two 511-keV photons that can be detected in a PET scanner.

PET imaging is an informative way to identify, study, and diagnose a disease in its early stage, and throughout its course. ^{18}F-FDG, a radiolabeled analogue of glucose, has been used to study alterations in glucose consumption in Alzheimer's, cardiovascular disease, and cancer (*47*). ^{18}F-FDG is transported into the cells through glucose transporters and is phosphorylated by hexokinases. The product FDG-6-PO$_4$ cannot be used for downstream reactions and is retained in the cell, in proportion to the rate of glycolysis (**Fig 1.5**).

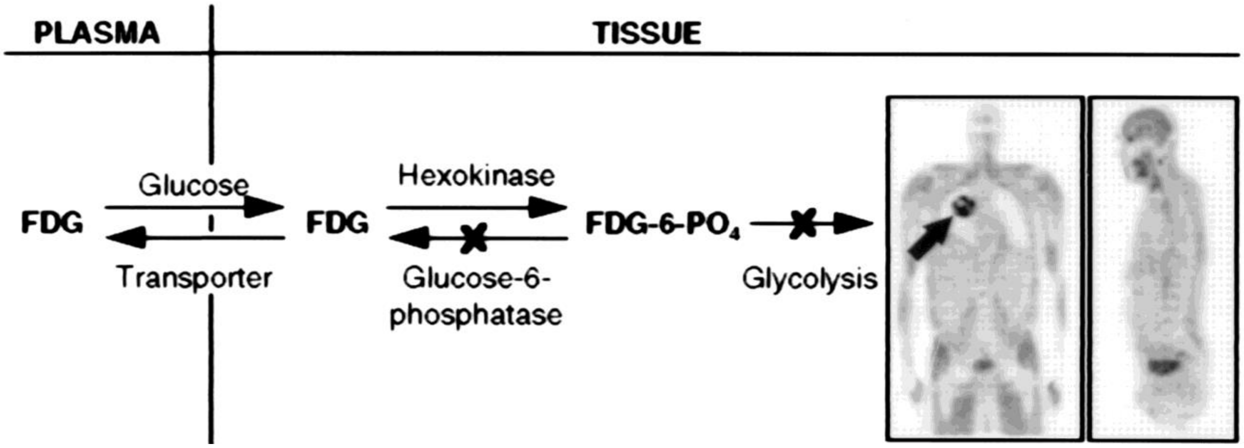

Figure 1.5. ^{18}F-FDG transport into tissues (*47*).

1.2.2 **PET imaging to study different aspects of MS**

MS is a chronic disease that affects the brain and spinal cord and results in multifocal lesions and damages to what would be normally-appearing tissues. Relapsing and remitting MS is characterized by inflammatory activity in the CNS and the progressive form is defined as neurodegeneration that will result in clinical progression and accumulation of disability. Neurodegeneration is a complex process in MS and is defined as an interplay between extraneuronal processes and intraneuronal mechanisms. Activation of the innate and adaptive immune system underlie the neurodegeneration in MS. Mitochondrial damage combined with the energy needed for nerve conduction in demyelinated state leads to hypoxia within the neurons, leading to chronic necrosis (*48*).

Important biological processes in MS all suggest potential therapeutic targets to stop disease progression of MS. However, many of these processes have been identified in post-mortem studies or in animal models. PET imaging can provide important functional information regarding neuroinflammation, demyelination, remyelination, and mitochondrial dysregulation and neuronal damage. In the following sections, I will review some the work in the PET imaging side to image MS *in vivo*.

Neuroinflammation

One aspect of MS is understanding how macrophages and microglia contribute to neurodegeneration in MS. 18-kDa translocator protein (TSPO) is located on the outer membrane of the mitochondria; higher expression levels of TSPO is associated with activated macrophages and microglia (*49*,*50*). Several generations of TSPO-based radiotracers were developed to asses activated macrophages and microglia *in vivo* such as ^{11}C-PK11195 and ^{18}F-PBR06 and ^{11}C-PBR28 (*51*,*52*). Important insights were learned from TSPO-based PET imaging. Microglia and macrophages are not only important in progressive phases of disease but also crucial to pathology starting at disease onset (*49*,*53–55*). Increased TSPO tracer binding was observed in lesions, perilesional areas, and normal-looking white and gray matter in MS patients during all stages of disease (*49*,*53–56*) (**Fig. 1.6**). TSPO-based PET have also shown that inflammation also exist in white matter area outside of visible lesions (*57*). This suggests that being able to image innate immune activation using PET in MS can predict clinical progression of disease (*58*). Furthermore, TSPO PET also has provided insights into the heterogenous nature of innate immune infiltration into lesions and healthy-looking tissues, an advantage in which techniques like MRI cannot do. However, TSPO has its limitations, including sensitivity to polymorphism, lack of specificity for microglia and macrophages, and lack of ability to differentiate between pro and anti-inflammatory innate immune cells. Radiotracers that bind to novel targets and are specific for specific types of immune cells are needed.

On the preclinical level, new radiotracers are currently being developed and tested to image different aspects of radiotracers such as ^{64}Cu Rituximab to image B cells (*59*), ^{11}C-CPPC to image colony-stimulating factor 1 receptor on microglia cells, and ^{64}Cu-TREM1 mAb for infiltrating myeloid cells.

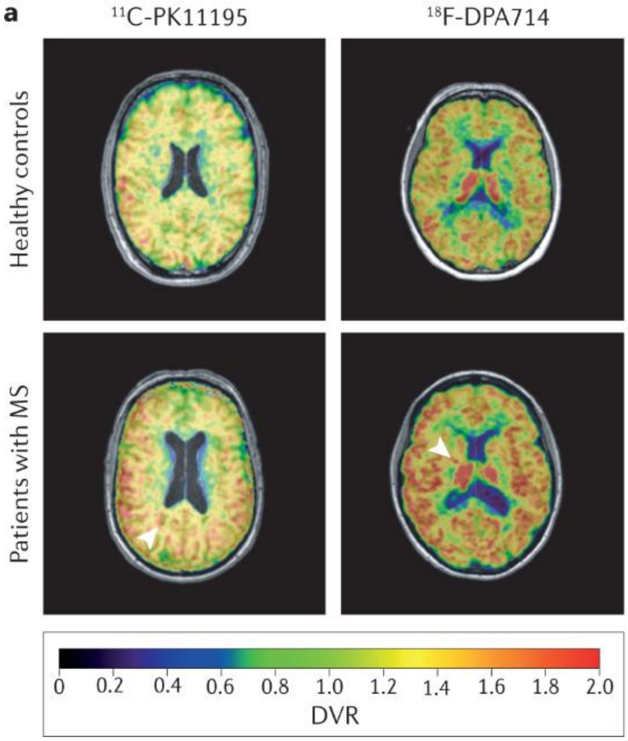

Figure 1.6. Example PET/MR imaging of healthy and MS patients injected with TSPO-based radiotracers ^{11}C-PK11195 and ^{18}F-DPA714.

Astrocytes

Astrocytes are involved in the innate immune system in MS pathology and can promote neurodegeneration and inflammation through activation of microglia and neurotoxic activities (*60*). Current PET imaging strategies to image and quantify astrocytes in humans are in development. One method that has been tested for imaging astrocytes is ^{11}C-acetate, which is supposedly taken up by astrocytes and readily accumulates in white and gray matter of MS patients compared to healthy controls, suggesting that this could reflect activation of astrocytes (*61*,*62*).

Another target for imaging astrocytes is monoamine oxidase B (MAO-B). MAO-B is an enzyme that resides in the outer membrane of mitochondria and is preferentially expressed on astrocytes (*63*,*64*). ^{18}F-THK5351 and ^{11}C-deuterium-L-deprenyl are PET radiotracers that inform MAO-B expression in activated astrocytes. These PET radiotracers were accumulated in a subset of inactivate plaques in MS patients, potentially suggesting that these radiotracers can be used to discriminate between gliotic and non-gliotic lesions in the brain(*63*,*64*).

Other PET approaches include imaging A2A purinergic receptor (A2AR) with ^{11}C-TMSX. A2AR I, expressed in brains of MS patients, is associated with reactive astrocytes in chronic active lesions (*65*). Other approaches include using ^{11}C-BU99008 to target imidazoline 2 binding site (I2BS), a protein that is localized in the outer membrane of the mitochondria on glial cells and can be overexpressed in activated astrocytes (*66*).

Demyelination and remyelination

Various techniques using MRI have been suggested for quantification of myelin content in MS. However, pathological features of MS cannot always be visualized with MRI. Using PET to image demyelination or remyelination will provide a more direct and specific measures of the myelin content in MS. Several Pet radiotracers have been developed to image myelin content. Stilbene and benzothiazole-derived PET tracers are examples of that bind to myelin (*67–70*). The stilbene compound ^{11}C-BMB interacts with beta sheets of myelin proteins but more studies need to be done to further confirm this (*67*). Another radiotracer that can bind to myelin is a thioflavin derived ^{11}C-PiB in which it has been shown that in a mouse model of demyelination, accumulation of ^{11}C-PiB was decreased and increased with myelin recovery (*71*). Newer generations of radiotracers such as ^{18}Fflorbetapir and ^{18}F-florbetaben have greater selectivity for myelin (*72*). These radiotracers have shown promise in that accumulation of these radiotracers were reduced in MS patients when compared to healthy controls. PET imaging of myelin can be informative but these radiotracers have limitations. Some radiotracers that are used to image myelin are repurposed beta-amyloid tracers which suggests that signal from the images may also reflect white matter signal and not exclusively myelin.

Neurodegeneration

In MS, secondary to inflammation and demyelination is neurodegeneration, a process in which there is axonal loss that leads to permanent clinical disability. PET imaging can help provide important information regarding neurodegeneration in MS. One of the first radiotracers that was used to understand neuronal function was ^{18}F-FDG. Patients with MS showed decreased accumulation of ^{18}F-FDG in the gray matter areas of the brain which has been associated with fatigue and cognitive dysfunction, suggesting that there may be some loss in neuronal function(*73*,*74*). Another tracer that provides information on neuronal function is flumazenil (FMZ), which is an antagonist of $GABA_A$ receptor and is located throughout the gray matter in axosomatic and axodendritic synapses. MS patients with ^{11}C-FMZ show neuronal damage at the cortical level and in the deep parts of the gray matter (*75*). Newer radiotracers such as ^{11}C-UCB-J bind to glycoprotein 2A (SV2A) that is expressed in presynaptic vesicles. Quantification of ^{11}C-UCB-J can provide information about the early stages of neurodegeneration through the dysfunction or loss of neuronal synapses (*76*). This imaging technique has been used to study Alzheimer disease, Parkinson disease, epilepsy, depression, and schizophrenia.

Another aspect of neurodegeneration is virtual hypoxia, a process in which neurons go through before leading to irreversible damage. ^{18}F-BCPP-EF is a PET radiotracer that aims to image mitochondrial complex 1 (MC1), an early component of oxidative phosphorylation (*77*).

1.3 Deoxyribonucleoside salvage in autoimmunity

1.3.1 **What is deoxyribonucleoside salvage**

Deoxyribonucleotide triphosphates (dNTP) are needed for DNA replication and synthesis. These dNTPs can be produced through two pathways, either through the de novo pathway or the deoxyribonucleoside salvage (*78*). During deoxyribonucleoside salvage, extracellular deoxyribonucleosides are transported into the cell for intracellular metabolism for biosynthesis of dNTPs (*78*). In the salvage pathway, deoxyribonucleosides are transported through the cell membrane by concentrative and equilibrative nucleoside transporters. Purines and pyrimidines are phosphorylated by deoxycytidine kinase (dCK), the rate-limiting enzyme in this pathway (*78–81*) (Fig 1.7). dCK is one of the two important enzymes that controls deoxyribonucleoside flux in the salvage pathway (*78*). The other enzyme is thymidine kinase 1 (TK1) (*82*).

dCK, a dimer in cells, can phosphorylate deoxycytidine, deoxyadenosine, and deoxyguanosine. dCK is also important for activating several nucleoside analogue drugs for cancer including cladribine and gemcitabine(*83*,*84*). In response to ionizing radiation and DNA damage, dCK is activated in cancer cells through phosphorylation of serine 74 by ataxia telangiectasia mutated (ATM) and ataxia telangiectasia and Rad3-related (ATR) enzymes. dCK activation is required for DNA damage repair and G2/M checkpoint (*85*,*86*).

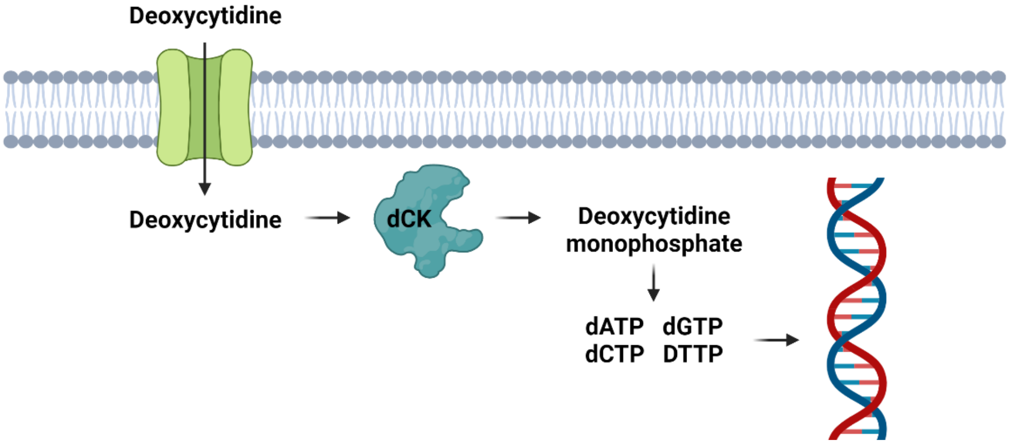

Figure 1.7. Deoxyribonucleoside salvage schematic.

1.3.2 **Deoxyribonucleoside salvage in development and autoimmunity**

Deficiencies in purine and pyrimidine metabolism are responsible for a variety of diseases that include effects on the immune system (*87*). For example, mutations in adenosine deaminase enzyme and purine nucleoside phosphorylase can lead to severe T lymphocyte deficiency and recurrent infections(*88*,*89*). Disorders related to pyrimidine metabolism such as orotic aciduria and pyrimidine nucleotide depletion syndrome lead to increased susceptibility to infections (*87*).

Deoxyribonucleoside salvage is utilized in lymphoid organs and rapidly proliferating tissues even though most other tissues using the *de novo* pathway (*90*). Deoxyribonucleoside salvage is enriched in lymphoid organs such as bone marrow, spleen, and the lymph nodes (*91*). Loss of dCK function in mice leads to impairment of T and B lymphocyte development in mice but embryogenesis and development of other organs were not affected (*81*). Furthermore, lack of dCK function results in depletion of (deoxycytidine triphosphate) dCTP pools, replication stress, and cell cycle arrest in mice (*92*). In vitro results suggest that deoxyribonucleoside salvage is increased in T cells when activated and in lymphoid organs of various mouse models including autoimmune hepatitis (*93*), systemic lupus erythematosus (*94*), inflammatory bowel disease (*95*), and anti-tumor immunity (*91*).

1.3.3 **PET imaging of deoxyribonucleoside salvage**

Monitoring immune function with PET imaging can have an important impact on diagnosing and treatment for disorders related to the immune system, such as autoimmune diseases. 1-(2′-deoxy-2′-18F-fluoroarabinofuranosyl) cytosine (^{18}F-FAC) is a radiolabeled analogue of deoxycytidine that measures deoxyribonucleoside salvage, a pathway that is enriched in leukocytes and accumulates at high levels in lymphoid tissues.. Similar to how deoxycytidine is transported into the cells and metabolized for downstream processes such as DNA replication and repair, ^{18}F-FAC is also transported into the cells through similar mechanisms and is phosphorylated by dCK. However, phosphorylated FAC is cannot be utilized and is accumulated in the cell (**Fig. 1.8**), allowing for the PET signals that see in the PET images.

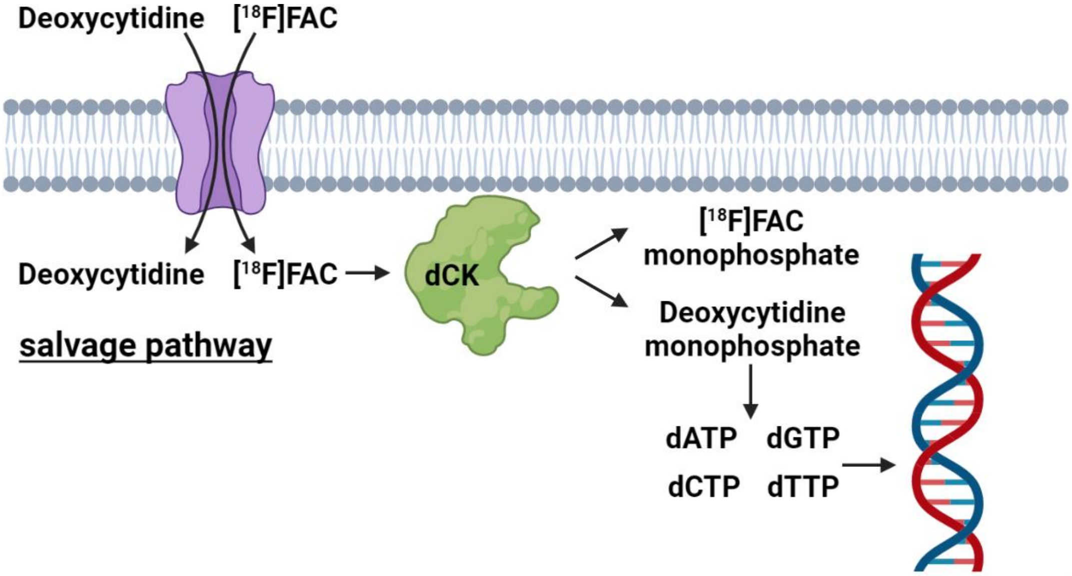

Figure 1.8. Deoxyribonucleoside salvage with deoxycytidine and ^{18}F-FAC schematic.

^{18}F-FAC enables PET imaging of deoxyribonucleoside salvage in mice but is rapidly deaminated due to high levels of cytidine deaminase (CDA) in humans (*96*). CDA converts ^{18}F-FAC into ^{18}F-FAU, a metabolite that cannot be phosphorylated by dCK. To solve this issue, ^{18}F-CFAwas developed to image deoxyribonucleoside salvage in humans (*97*).

1.4 Conclusion

MS is a chronic autoimmune disease that can severely affect a patient’s quality of life. Current method used to monitor MS and therapeutic effectiveness is through magnetic resonance imaging (MRI).While this imaging modality can provide important anatomical information regarding MS, it does not provide functional information in terms of the biology of MS, such as the cells that are activated and contributing to disease onset and progression. Furthermore, therapies that are currently used to treat MS patients only help a subset of patients. There is a need for a method to image key pathogenic immune cells in MS and new therapeutic options that can meet the needs of a larger subset of MS patients.

In this dissertation, I evaluate the use of image-guided therapeutic intervention for autoimmune diseases. In chapter 2, I evaluate the use of [^{18}F]FAC to image brain-infiltrating leukocytes in a mouse model of MS and determined the use of [^{18}F]FAC in monitoring therapeutic intervention. In chapter 3, I targeted the deoxyribonucleoside salvage pathway through the use of a novel dCK inhibitor, TRE-515, in multiple models of MS and evaluated the specific immune cell types affected by the pharmacological inhibition. In chapter 4, I draw my conclusions regarding image-guided therapeutic intervention for autoimmune diseases. Finally, in chapter 5, I discuss some of the other works that I have contributed to throughout my PhD process.

Chapter 2: [^{18}F]FAC PET visualizes brain-infiltrating leukocytes in a mouse model of multiple sclerosis

2.1 Introduction

Brain-infiltrating leukocytes drive pathology in multiple sclerosis (MS) and autoimmune encephalomyelitis (*31*,*98–100*). During MS brain-infiltrating T cells, B cells, and macrophages promote neurodegeneration (*31*,*98*,*99*). In addition, disease-modifying therapies modulate the immune system (*100*). Leukocytes are also found in the brains of murine models of traumatic brain injury, stroke, and seizure and of postmortem Parkinson's disease and P301L tau frontotemporal dementia patients (*101–108*). Inhibiting leukocyte migration into the brain or depleting lymphocytes in these animal models can slow disease progression (*102–108*), suggesting a functional role for the immune system in these diseases. Although PET assays have been developed to image and quantify different aspects of neuroinflammation (*59*,*109–112*), there is no PET assay to visualize brain-infiltrating leukocytes. A non-invasive method to selectively image and quantify brain-infiltrating leukocytes would complement current approaches and provide information on tleukocyte ocation during the development and treatment of neurological diseases.

The radiotracer 1-(2′-deoxy-2′-18F-fluoroarabinofuranosyl) cytosine ([^{18}F]FAC) is a deoxynucleoside analogue that measures deoxynucleoside salvage, a biochemical pathway enriched in leukocytes. ([^{18}F]FAC)accumulates at high levels in lymphoid tissues; and is increased in these same tissues in mouse models of immune activation (*91*,*93*,*94*). Additionally, [^{18}F]FAC accumulates at higher levels in activated T lymphocytes than in effector-memory T cells, CD11b+ innate immune cells, or B220+ B cells and at low levels in the healthy brain (*91*,*93*,*94*).

We hypothesized that [^{18}F]FAC PET could non-invasively visualize brain-infiltrating leukocytes. In this chapter, [^{18}F]FAC PET imaging results in an experimental autoimmune encephalomyelitis (EAE) mouse model of MS are presented. Our results suggest that [^{18}F]FAC PET can visualize brain-infiltrating leukocytes during disease and treatment.

2.2 Methods

2.2.1 **EAE mouse model and induction**

10-week-old, female C57BL/6 and NOD scid gamma (NSG) mice were used for all experiments. All mouse experiments were approved by the UCLA Animal Resource Committee. Mice were injected with an emulsion of myelin oligodendrocyte glycoprotein (MOG_{35-55}) in Freund's complete adjuvant (100 μL) and with pertussis toxin (80 ng) 2 hours and again 24 hours later (Hooke Laboratories). EAE treatments were conducted and scored similarly to reported (*111*,*113*). All experiments were conducted 13 to 15 days post-immunization. Fingolimod (0.5 mg/kg; Selleckchem S5002) or vehicle were injected intraperitoneal daily starting immediately post-immunization. Immunocompetent EAE mice were used at an average clinical score of 3.0.

2.2.2 **Immunohistochemistry**

Sagittal brain sections (4 μm) were immunostained as described (20) except for the additional inclusion of anti-CD45 (Clone 30-F11; 1:00; Novus Biologicals), imaged at 1X and 40X magnification, and quantified using the Ilastik software (Version 1.3.2). Boxes in the 1x magnification images outline from where the 40x magnification images were taken. To evaluate correlations, two independent 40X magnification images were scored using an H-score (*114*).

2.2.3 **[^{18}F]FAC PET/CT**

Mice injected with either [^{18}F]FAC (1.85 MBq) or with [^{18}F]FAC (1.85 MBq) plus 10 mg of non-radiolabeled FAC were imaged for an hour or imaged one-hour post-injection for 10 min on a G8 PET/CT. The one-hour post-injection time point was chosen as this is the earliest time point at which [^{18}F]FAC accumulation in the brain and blood no longer rapidly changes. Images were 6 analyzed using AMIDE (Version 1.0.4), and the MRM neurological atlas was fitted to the mouse skull (*115*,*116*). Regions of interest (ROI) were drawn at the interface of the hippocampus, thalamus, and midbrain as demarcated by the neurological atlas. [^{18}F]FAC blood levels were determined from a ROI drawn within the left ventricle of the heart.

2.2.4 ***Ex vivo*** **biodistribution studies**

Mice were injected with FAC (1.85 MBq). One-hour post-injection, blood (100 µL) was collected, the mice were perfused, and organs were extracted and rinsed in 1x PBS. Activity and weight of the blood and organs were measured.

2.2.5 **Autoradiography**

Autoradiography was performed as previously described (*117*). Briefly, pre- and postimmunization EAE mice were injected with [^{18}F]FAC (18.5 MBq) and sagittal brain sections (10 µm) from perfused mice were cut.

2.2.6 ***Ex vivo*** **accumulation assay**

Brain leukocyte isolation was conducted similar to previously described (*118*), and CD4+ and CD11b+ cells were isolated by flow cytometry cell sorting (*118*). Ex vivo deoxycytidine accumulation was performed as previously described (*93*) by incubating ~20,000 of each cell type in a 96-well filter plate with [^{3}H]deoxycytidine (0.037 MBq per well) for 30 min.

2.2.7 **Statistical analysis**

Data was analyzed using GraphPad Prism (Version 7.03). Statistical comparisons were performed using two-sided t-tests and one-way ANOVA analyses with multiple comparison testing. Data is reported as mean ± standard error.

2.3 Results

2.3.1 **[^{18}F]FAC crosses the blood brain barrier in healthy mice**

To develop a PET assay to quantify brain-infiltrating leukocytes in neurological diseases, we needed a PET radiotracer that accumulates in leukocytes and crosses the BBB. [^{18}F]FAC is a pyrimidine deoxynucleoside analogue radiotracer that accumulates in leukocytes (*91*,*94*). Generally, pyrimidine ribonucleosides except for uridine, do not cross the BBB, but studies suggest that [^{18}F]FAC accumulates at ~2 %ID/g in the brain of healthy mice (*94*,*119*).

[^{18}F]FAC accumulated at nearly uniform levels throughout the healthy mouse brain as evaluated by PET and autoradiography one-hour post-injection (Fig. 2.1A, 2.1B). [^{18}F]FAC levels in the healthy mouse brain, corrected for blood volume in the brain (*120*), were slightly lower than [^{18}F]FAC levels in the blood (brain-to-blood ratio quantified from the PET images: 0.84±0.05 – brain: 2.54±0.2 %ID/g, blood: 3.04±0.3 %ID/g; brain-to-blood ratio quantified from isolated tissue and blood: 0.76±0.05; Figs. 2.1C, 2.1D; [^{18}F]FAC time-activity curves: Fig. 2.2, correlation between brain-to-blood ratios quantified from the PET images and from isolated tissue and blood: R^2=0.89, Fig. 2.3). [^{18}F]FAC has a logP value of -1.33, well below the 2 – 3.5 logP value of most radiotracers that diffuse into the brain, suggesting that [^{18}F]FAC is transported across the BBB (*121*). Collectively, these data suggest that [^{18}F]FAC crosses the healthy BBB.

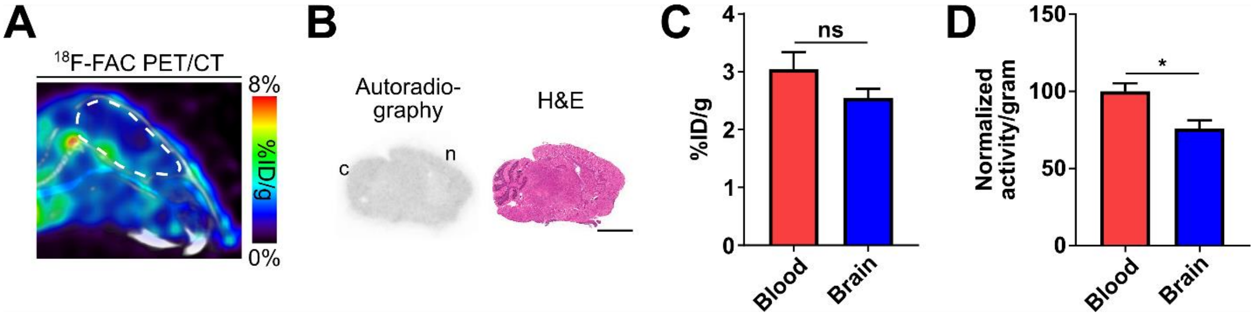

Figure 2.1. [^{18}F]FAC crosses the blood brain barrier in healthy mice.

(A) Sagittal [^{18}F]FAC PET/CT image of a healthy C57BL/6 mouse. Representative image of n=5. **Brain outlined in white**. (B) [^{18}F]FAC autoradiography and H&E staining of a sagittal brain section from a healthy C57BL/6 mouse. Scale bar: 3 mm. c: cerebellum, n: neocortex. Representative image of n=5. (C) Blood and brain [^{18}F]FAC levels, quantified from PET images of healthy C57BL/6 mice. n=5. (D) Normalized blood and brain [^{18}F]FAC levels, quantified from extracted blood and brain. n=6. *: $P<0.05$, ns: not significant.

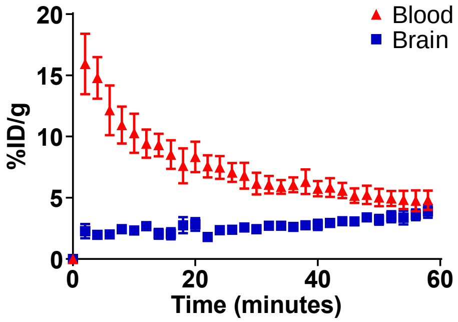

Figure 2.2. Time activity curves of [^{18}F]FAC accumulation.

Time activity curves of [^{18}F]FAC accumulation in blood and brains of healthy mice. n=5.

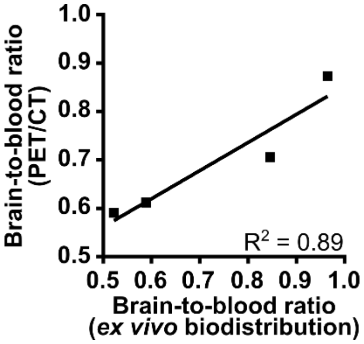

Figure 2.3. Brain-to-blood ratios of [^{18}F]FAC in healthy mice.

Brain-to-blood ratios of [^{18}F]FAC in healthy mice, as measured from the PET/CT images and ex vivo biodistribution studies. n=4.

2.3.2 **Brain-infiltrating leukocytes are present in EAE mice.**

EAE is a well-established MS model with leukocyte infiltration into the spinal cord and brain (*122*,*123*). EAE was induced in immunocompetent C57BL/6 and immunocompromised NSG mice by co-injecting $\text{MOG}_{35\text{-}55}$ in Freund's complete adjuvant with pertussis toxin (*111*,*113*). NSG mice are immunodeficient due to *scid* and $\mathit{IL2rg}^{null}$ mutations that result in B and T cell deficiency and lack of cytokine signaling for functional NK cells. Consistent with literature (*111*,*113*), immunocompetent mice began to display EAE symptoms ~9 days post-immunization that peaked ~13 days post-immunization and which included a limp tail, hind leg paralysis, and severe head tilting (Fig. 2.4A). Immunocompromised mice treated to induce EAE never displayed symptoms (Fig. 2.4A). Immunohistochemistry of immunocompetent mouse brain sections demonstrated significant perivascular and periventricular leukocyte infiltrates characterized by an abundance of CD11b-positive innate immune cells and CD4 T cells with few B220-positive B cells and CD8 T cells (Fig. 2.4B). 37±2% of infiltrating leukocytes in these sections were dividing as suggested by Ki67 immunostaining. No infiltrating leukocytes were observed in the immunocompromised EAE mouse brains (Fig. 2.4B). Isolated leukocytes from immunocompetent EAE mouse brains were similarly enriched for CD11b-positive innate immune cells and CD4 T cells (Fig. 2.4C).

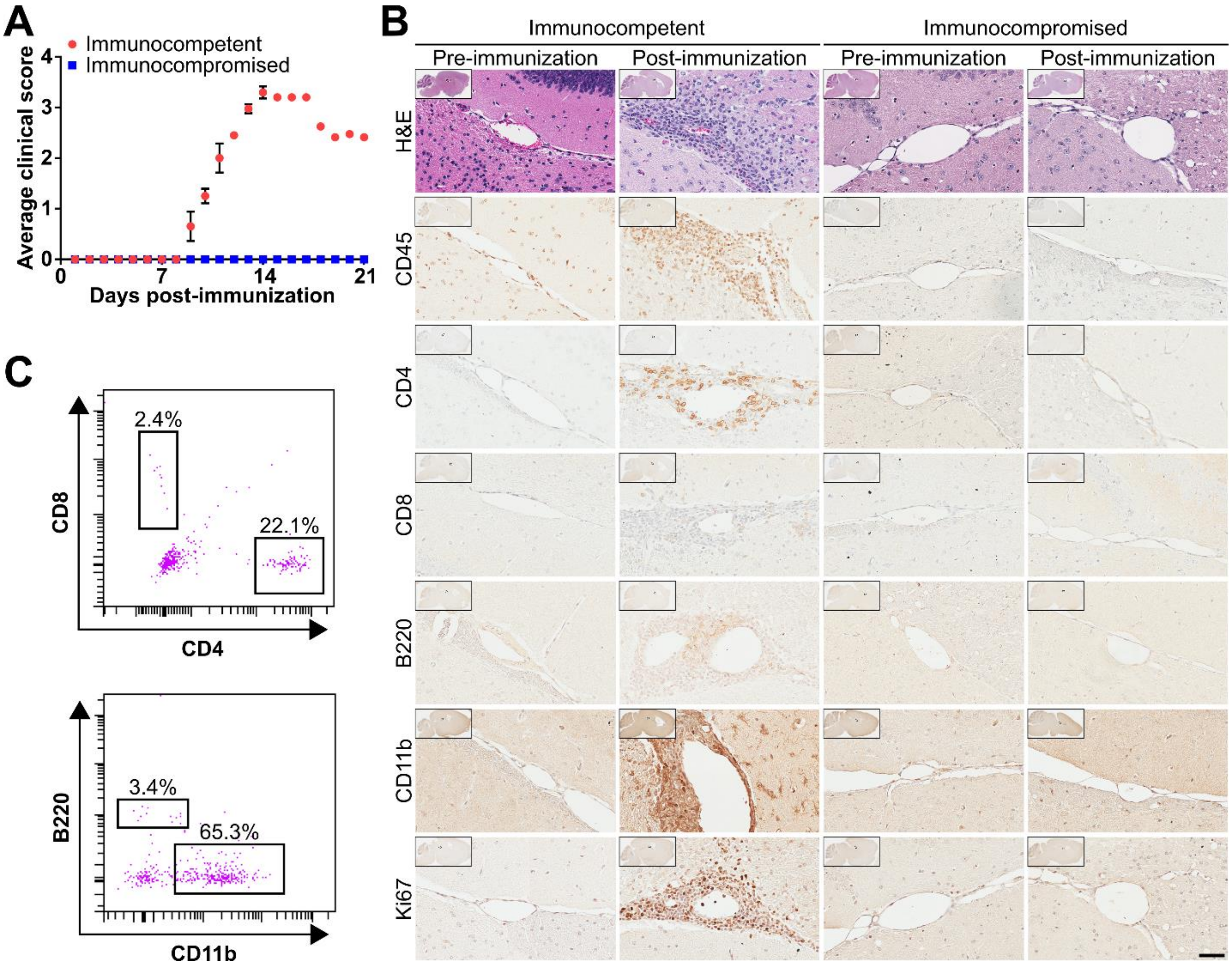

Figure 2.4. Brain-infiltrating leukocytes are present in EAE mouse model.

(A) Time course of EAE symptoms in immunocompetent and immunocompromised mice. n=4. (B) H&E and immunohistochemical stains of brain sections of mice pre- and post-immunization. 1X and 40X magnification images. Scale bar: 50 microns. n=2. (C) Immune cell populations isolated by fluorescence-activated cell sorting from immunocompetent EAE mouse brains. n=3.

2.3.3 **[^{18}F]FAC accumulates at higher levels in EAE mice**

Immunocompetent and immunocompromised pre-immunization and EAE mice were injected with [^{18}F]FAC and imaged by PET/CT one hour later. [^{18}F]FAC accumulation in the brains of immunocompetent EAE mice was 180% of the levels of [^{18}F]FAC accumulation in pre-immunization immunocompetent mice, based on a ROI drawn at the interface of the hippocampus, midbrain, and thalamus, where a high concentration of infiltrating leukocytes resides (pre-immunization immunocompetent mice: 2.4±0.15 %ID/g; immunocompetent EAE mice: 4.4±0.66 %ID/g; Fig. 2.5A; Fig. 2.6). [^{18}F]FAC accumulation in this same brain region of immunocompromised EAE mice was not significantly different from pre-immunization immunocompromised mice (pre-immunization immunocompromised mice: 3.2±0.31 %ID/g; immunocompromised EAE mice: 2.4±0.15 %ID/g; Fig. 2.5B; Fig. 2.6). [^{18}F]FAC brain accumulation was lower in immunocompetent mice than in immunocompromised mice pre-immunization, and lower in post-immunization than in preimmunization immunocompromised mice. We cannot readily explain either of these results, although neither result reached statistical significance. [^{18}F]FAC accumulation was also significantly increased in the spleen and lymph nodes but not the femur, bone marrow, or spinal cord of the immunocompetent EAE compared to pre-immunization mice (quantified from the PET images: spleen – pre-immunization mice: 11.8±2.1 %ID/g, EAE mice: 21.3±3.2 %ID/g; lymph nodes – pre-immunization mice: 2.3±0.06 %ID/g, EAE mice: 9.1±0.84 %ID/g; bone marrow – preimmunization mice: 14.7±1.1 %ID/g, EAE mice: 11.9±1.5 %ID/g; spinal cord – pre-immunization mice: 4.9±0.24 %ID/g, EAE mice: 5.7±0.70 %ID/g; Fig. 2.7; ex vivo biodistribution data: Fig. 2.8). EAE mice suffer BBB breakdown, leading to the slow exchange or pooling of blood fluids in areas with significant leukocyte infiltration and a compromised BBB (*124*). Our results in the EAE model could be due to [^{18}F]FAC in these blood pools and not to specific cellular [^{18}F]FAC accumulation. Immunocompetent EAE mice were injected with [^{18}F]FAC supplemented with 10 mg non-radiolabeled FAC. Cellular FAC accumulation can be saturated but FAC accumulation in blood pools cannot. Co-injection of [^{18}F]FAC and non-radiolabeled FAC decreased brain [^{18}F]FAC accumulation in immunocompetent EAE mice by 57% compared to immunocompetent EAE mice injected with only [^{18}F]FAC and to 78% of the levels of pre-immunization immunocompetent mice (pre-immunization immunocompetent mice: 2.4±0.15 %ID/g; immunocompetent EAE mice: 4.4±0.66 %ID/g; immunocompetent EAE mice injected with [^{18}F]FAC and non-radiolabeled FAC: 1.9±0.15 %ID/g; Fig. 2.5A; Fig. 2.6). This suggests that the increased [^{18}F]FAC accumulation in the immunocompetent EAE mouse brains is due to specific cellular [^{18}F]FAC accumulation.

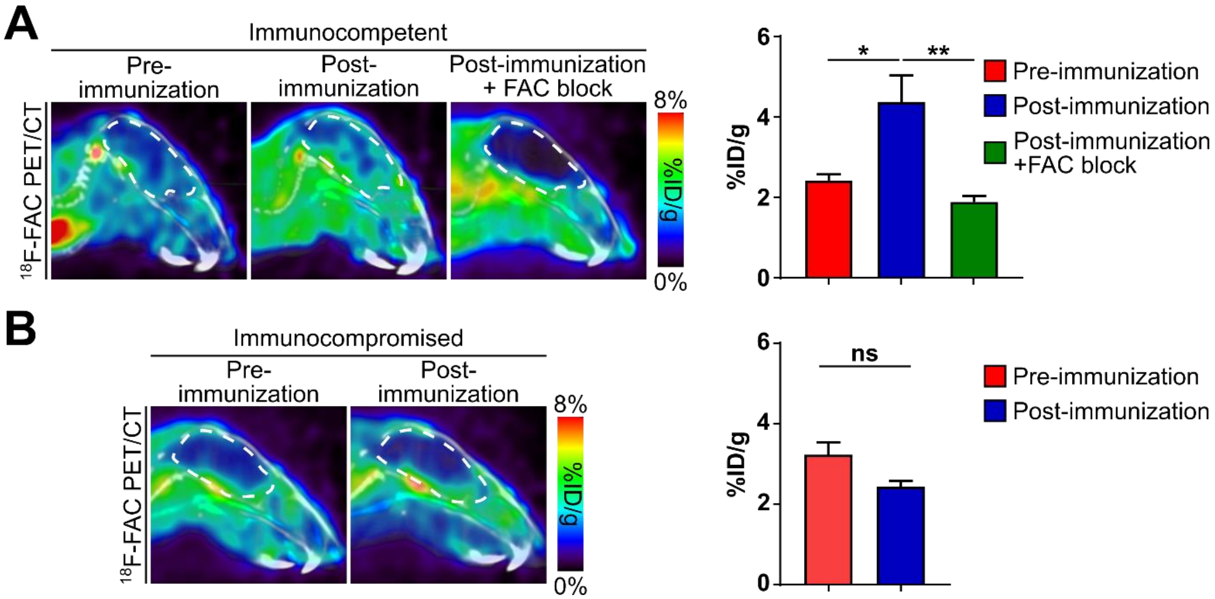

Figure 2.5. [^{18}F]FAC accumulates more in the brains of EAE mice than control mice.

Sagittal [^{18}F]FAC PET/CT images (left) and quantification (right) of (A) immunocompetent and (B) immunocompromised pre- and post-immunization mice. FAC block: co-injection of mice with [^{18}F]FAC and non-radiolabeled FAC. All experiments: n=4. *: P<0.05, **: P<0.01, ns: not significant. Brains outlined in white.

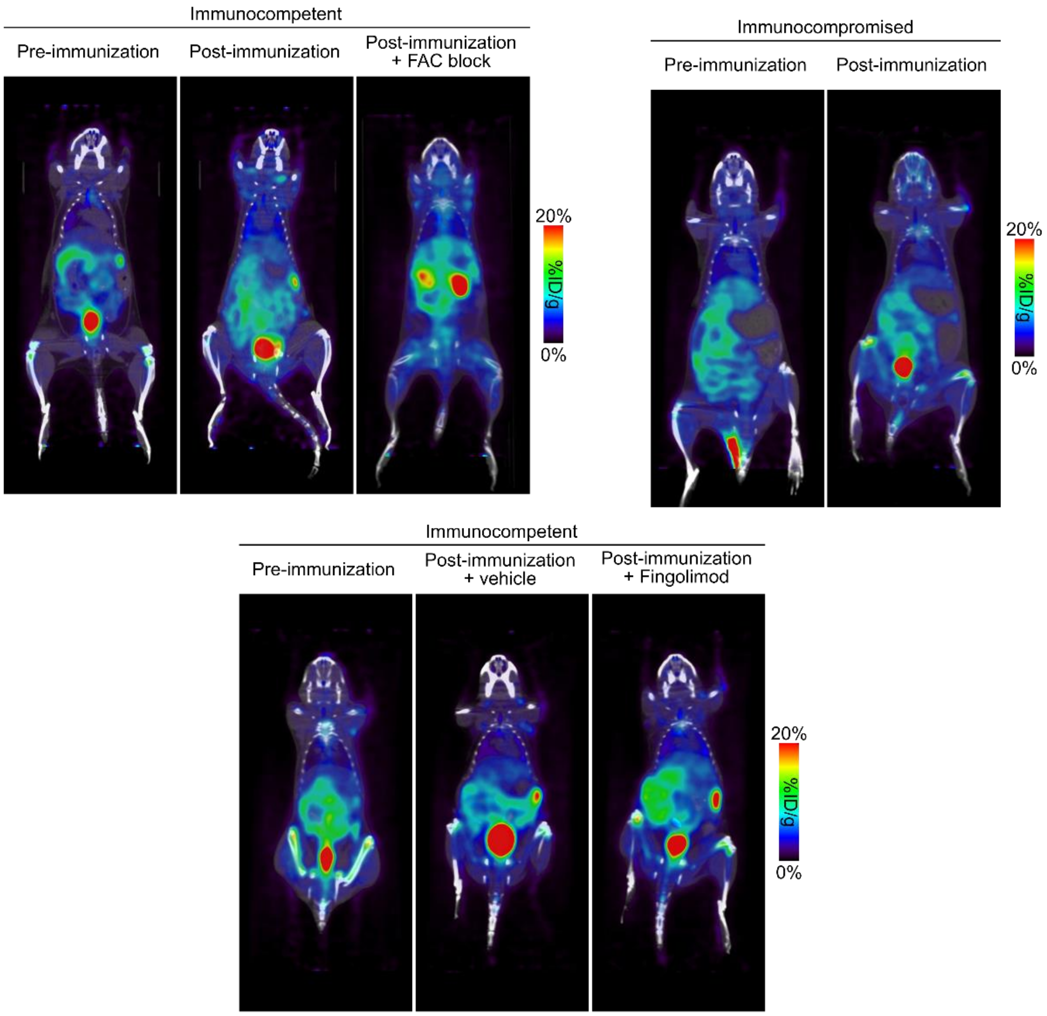

Figure 2.6. Whole body PET/CT of mice pre and post-immunization.

[^{18}F]FAC accumulation in immunocompetent and immunocompromised mice pre- and post-immunization, and co-injected with non-radiolabeled FAC (FAC block) or treated with vehicle or fingolimod. H = heart, S = spleen, B = bladder.

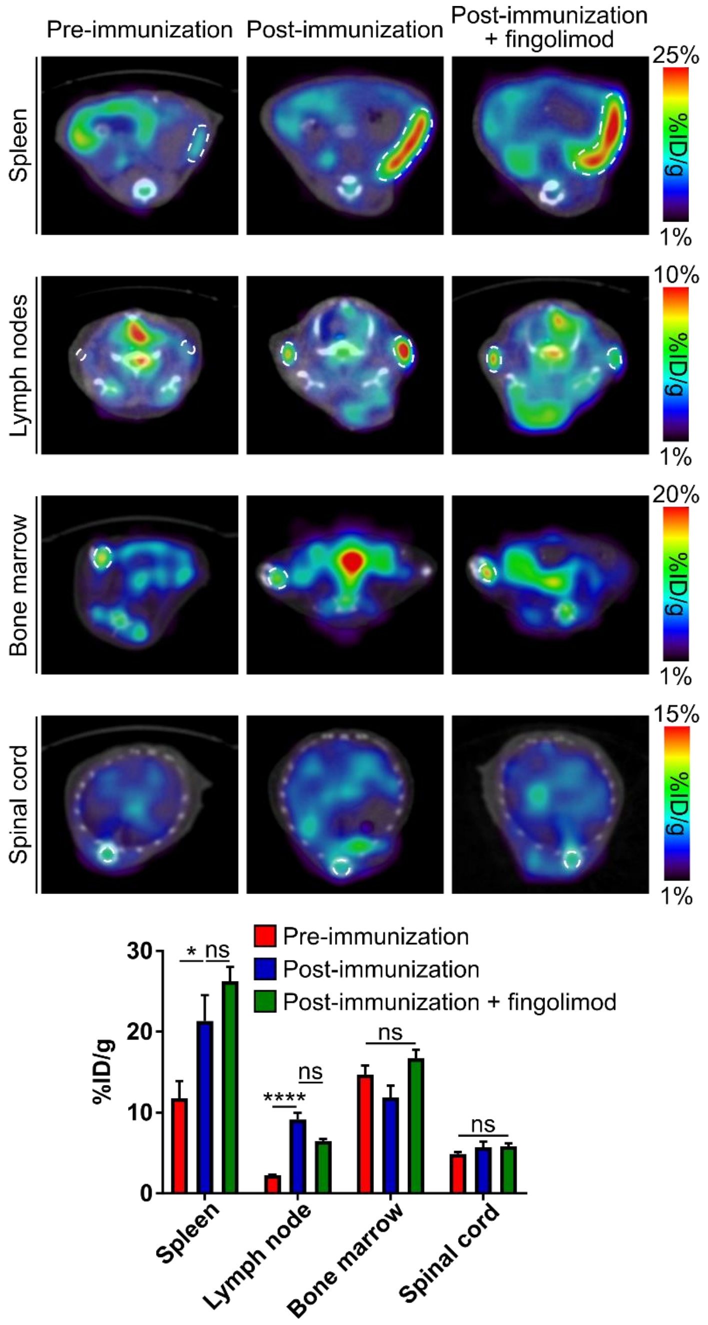

Figure 2.7. Monitoring peripheral immune activation in EAE at 14 days post-immunization.

[^{18}F]FAC PET can be used to monitor peripheral immune activation at specific locations throughout the body in EAE mice and following treatment with an immunomodulatory drug. Representative transverse [^{18}F]FAC PET/CT images of immunocompetent mice pre-immunization, post-immunization, and postimmunization and treated with fingolimod. Spleen, lymph nodes, bone marrow, and spinal cord encircled in a white dotted line (top). Quantification (bottom). Preimmunization and post-immunization: n=7; postimmunization and treated with fingolimod: n=3. *:P<0.05; ****: P<0.0001, ns: not significant.

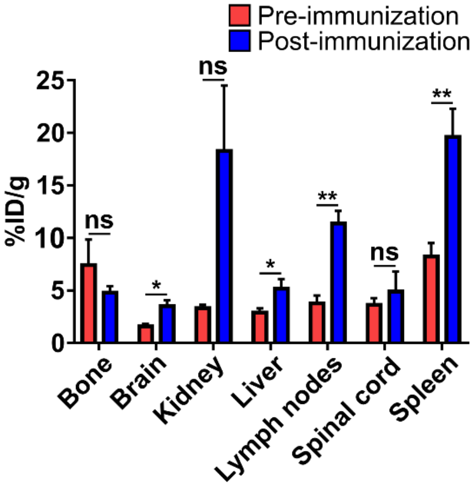

Figure 2.8. [^{18}F]FAC biodistribution immunocompetent mice pre- and post-immunization.

[^{18}F]FAC biodistribution, measured ex vivo in organs from immunocompetent mice pre- and post-immunization. n=4 except for spinal cord which is n=3. *: P<0.05, **: P<0.01, ns: not significant.

2.3.4 **[^{18}F]FAC accumulates in brain-infiltrating leukocytes in EAE mice.**

Deoxycytidine kinase (dCK) phosphorylates [^{18}F]FAC and is a rate-limiting enzyme in the cellular accumulation of this radiotracer ((*81*,*94*). Brain sections of pre-immunization or EAE mice were immunostained with an antibody targeting dCK. Strong dCK immunostaining was apparent in 68±5% of the infiltrating leukocytes in the brain sections of the immunocompetent EAE mice and the intensity and number of immunostained leukocytes correlated with brain [^{18}F]FAC accumulation (R^2=0.85; Fig. 2.9A; Fig. 2.10). In contrast, 37±12% of leukocytes in the spinal cord of immunocompetent EAE mice, a tissue in which [^{18}F]FAC accumulation did not increase compared to pre-injection mice, stained strongly for dCK (Fig. 2.11). Weak dCK immunostaining was present in the brain parenchyma across all conditions, and the degree of dCK immunostaining in the brain parenchyma was unaffected by the EAE treatment (Fig. 2.9A). This suggests increased brain [^{18}F]FAC accumulation in the immunocompetent EAE mice may be due to the tracer accumulating in the brain-infiltrating leukocytes. Consistent with this model, autoradiography of brain sections of immunocompetent EAE mice injected with [^{18}F]FAC shows the greatest enrichment in [^{18}F]FAC accumulation specifically in areas coincident with significant leukocyte infiltration in the EAE mouse brain (Fig. 2.9B). Brain-infiltrating leukocytes in this model consist mostly of CD11b-positive innate immune cells and CD4 T cells (Fig. 2.4B, C). Deoxynucleoside salvage activity was similar between CD11b positive innate immune cells and CD4 T cells isolated from the immunocompetent EAE mouse brains (Fig. 2.9C). Insufficient B220-positive B cells and CD8 T cells could be isolated for analysis. The number of leukocytes in the brain correlated with [^{18}F]FAC accumulation (R^2=0.82; Fig. 2.12). Whether activated microglia also consume [^{18}F]FAC remains a topic for future study. However, the overlap between the strong [^{18}F]FAC accumulation identified in the autoradiography and the areas identified by immunohistochemistry as having significant leukocyte infiltration (Figs. 2.4B, 2.9B) supports our interpretation that [^{18}F]FAC accumulates in and [^{18}F]FAC PET images brain-infiltrating leukocytes. Collectively this suggests a model in which elevated [^{18}F]FAC accumulation in brain regions of immunocompetent EAE mice with significant leukocyte infiltration is due to [^{18}F]FAC accumulation in all of the brain-infiltrating leukocyte populations.

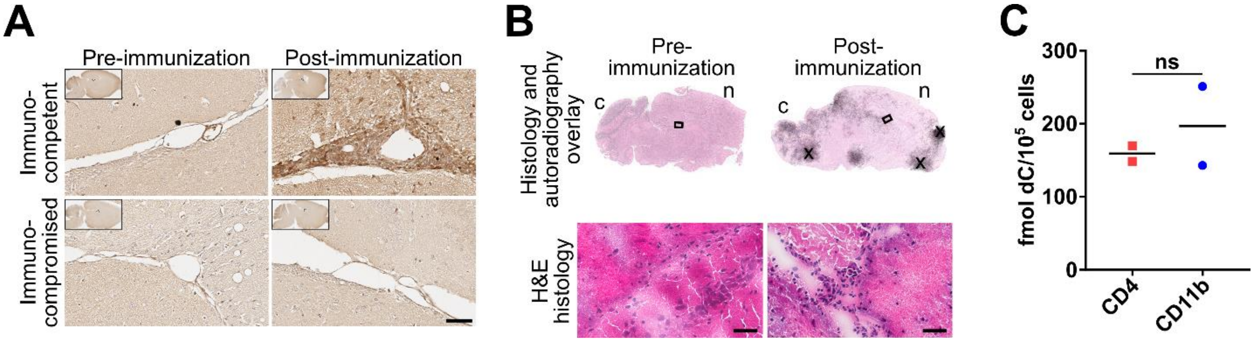

Figure 2.9. [^{18}F]FAC accumulates in brain-infiltrating leukocytes in an EAE mouse model.

(A) Mouse brain sections immunostained for deoxycytidine kinase pre- and post-immunization. 1X and 40X magnification images. Scale bar: 50 microns. n=2. (B) [^{18}F]FAC autoradiography images and H&E staining of sagittal brain sections of immunocompetent mice pre- and post-immunization. 1X and 40X magnification images. Scale bars: 50 microns. c: cerebellum, n: neocortex, x: regions where the tissue wrinkled. n=2. (C) Deoxycytidine (dC) accumulation in leukocyte populations isolated from immunocompetent EAE mouse brains. n=2. ns: not significant.

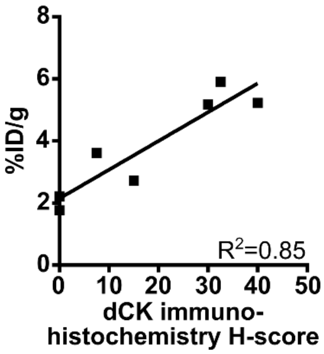

Figure 2.10. dCK immunostain and [^{18}F]FAC accumulation correlation.

dCK immunostaining (as measured by an immunohistochemistry H-score) and [^{18}F]FAC accumulation in the brains of immunocompetent mice. n=7.

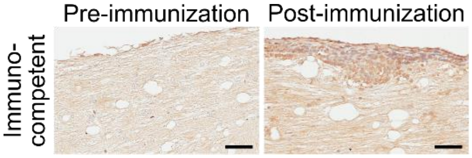

Figure 2.11. dCK immunostain of spinal cord tissue.

dCK immunostaining of spinal cord tissue sections from immunocompetent mice pre- and post-immunization. 40x magnification images. Scale bars: 50 microns. Representative images of n=2.

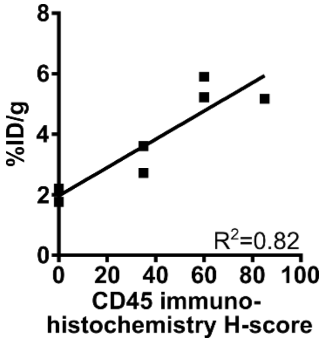

Figure 2.12. CD45 immunostain and [^{18}F]FAC accumulation correlation.

CD45 immunostaining (as measured by an immunohistochemistry H-score) and [^{18}F]FAC accumulation in the brains of immunocompetent mice. n=7.

2.3.5 **Monitoring immunomodulatory therapies using [^{18}F]FAC in EAE mice**

The small molecule fingolimod modulates the sphingosine-1-phosphate receptor, sequesters lymphocytes in lymph nodes and the spleen, and limits autoimmune diseases such as MS (*100*,*125*). Fingolimod decreased leukocytes in the brain of immunocompetent EAE mice compared to vehicle treatment (Fig. 2.13A). Fingolimod also significantly decreased brain [^{18}F]FAC accumulation compared to vehicle treatment in these same mice (pre-immunization mice: 2.0±0.13 %ID/g, EAE mice treated with vehicle: 4.2±0.25 %ID/g, EAE mice treated with fingolimod: 2.7±0.08 %ID/g; Fig. 2.13B, Fig. 2.6). Consistent with its mechanism of sequestering lymphocytes to lymph nodes and the spleen (4,35), fingolimod had no effect on [^{18}F]FAC accumulation in the lymph nodes and spleen of immunocompetent EAE mice (lymph nodes – EAE mice: 9.1±0.84 %ID/g, EAE mice treated with fingolimod: 6.5±0.26 %ID/g; Spleen – EAE mice: 21.3±3.2 %ID/g, EAE mice treated with fingolimod: 26.2±1.8 %ID/g; Fig. 2.6, Fig. 2.7).

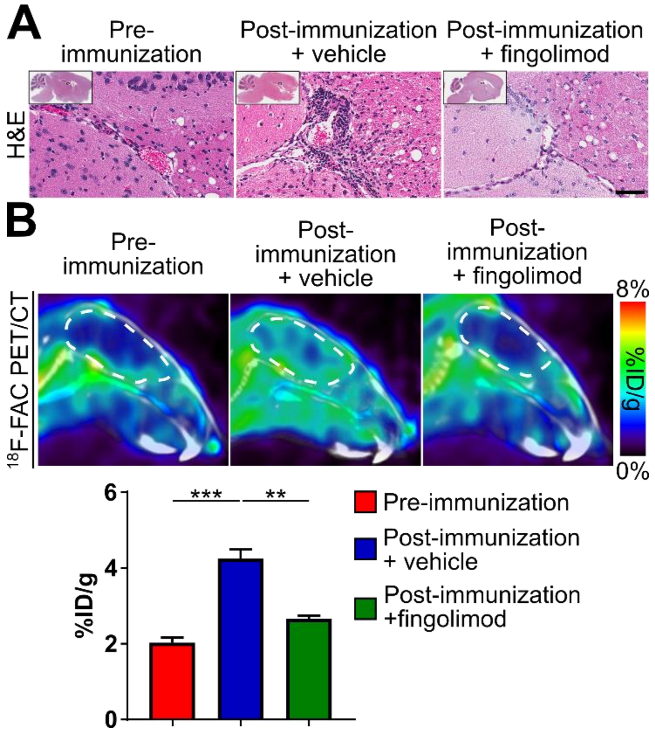

Figure 2.13. [^{18}F]FAC PET monitors immunomodulatory drug treatments in EAE.

(A) H&E stains of brain sections and (B) sagittal PET/CT images and quantification of [^{18}F]FAC accumulation in the brains of mice pre-immunization, and post-immunization and treated with vehicle or fingolimod. 1X and 40X magnification images. Scale bar: 50 microns. H&E: n=2, PET/CT: Pre-immunization: n=4, Post-immunization + vehicle: n=4; Post-immunization +fingolimod: n=3. **: P<0.01, ***: P<0.001. Brains outlined in white.

2.3.6 **[^{18}F]CFA does not cross the blood brain barrier in humans**

[^{18}F]FAC is deaminated in humans but 2-chloro-2'-deoxy-2'-18F-fluoro-9-β-Darabinofuranosyl-adenine ([^{18}F]-CFA), a radiotracer that also measures deoxynucleoside salvage (*97*,*126*,*127*). Accounting for blood volume in the brain(*128*), [^{18}F]CFA accumulates in the brain at 11.0±1.4% of the levels of 18F-CFA found in the blood (135 min post-injection: brain SUV: 0.08±0.01; blood SUV: 0.54±0.07; Fig. 2.14), suggesting that [^{18}F]CFA does not cross the BBB in healthy human patients.

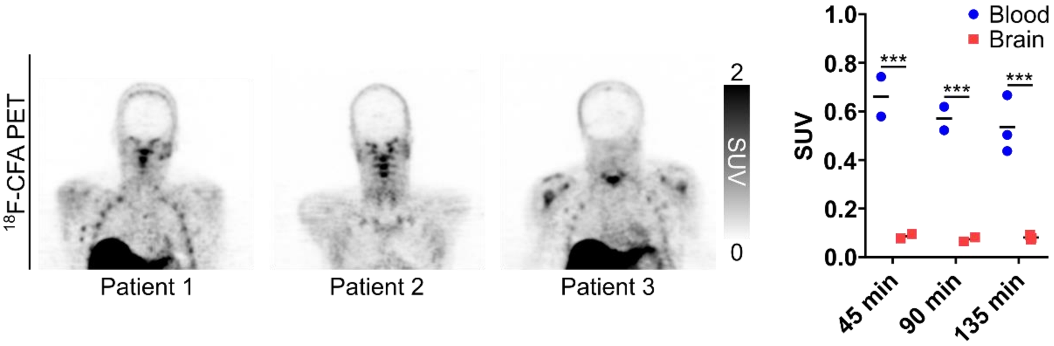

Figure 2.14. [^{18}F]CFA accumulation in healthy patients.

[^{18}F]CFA does not readily cross the blood-brain barrier in healthy human subjects. Representative coronal PET images of healthy volunteers injected with [^{18}F]CFA at 135 min post-tracer injection (left). Blood and brain [^{18}F]CFA accumulation, quantified from the PET images of healthy volunteers (right). The PET scans analyzed here are the same as those reported in (*129*). 45- and 90-min time point: n=2; 135 min time point: n=3. ***: P<0.001.

2.4 Discussion

Despite studies showing that [^{18}F]FAC selectively accumulates in activated lymphocytes in mouse models of autoimmune hepatitis and antitumor immunity (*91*,*93*,*94*), in the EAE mouse model we do not identify selective [^{18}F]FAC accumulation in brain-infiltrating lymphocytes. In the mouse model of antitumor immunity, the rate of 18F-FAC accumulation in T cells was proportional to the rate of cellular proliferation (*91*). One explanation for our results is that brain-infiltrating lymphocytes are not rapidly dividing and thus do not consume high [^{18}F]FAC levels. Only 37±2% of the brain-infiltrating leukocytes in our model are dividing, similar to the number of dividing liver-infiltrating leukocytes in a viral hepatitis model in which no enhanced hepatic [^{18}F]FAC accumulation was observed (*93*). [^{18}F]FAC is likely able to image infiltrating leukocytes in the EAE model but not the viral hepatitis model due to the ~50% lower basal accumulation of [^{18}F]FAC in the brain than the liver. [^{18}F]FAC may show selectivity for lymphocytes in other models with more actively dividing lymphocytes in the brain.

We show higher [^{18}F]FAC accumulation in brain-infiltrating leukocytes and in lymphoid organs such as the spleen and lymph nodes in the EAE model. [^{18}F]FAC measures deoxynucleoside salvage, for which dCK is a rate-limiting enzyme, and genetic knockout of dCK in healthy mice leads to decreased lymphocyte levels (*81*,*94*). Small molecule dCK inhibitors with in vivo efficacy have been developed (*130*). Our data may suggest that dCK inhibitors could limit disease in this model.

A previous study found that [^{18}F]FDG accumulation in the spinal cord increased by 200% compared to control mice in this exact EAE model at the exact time point we studied (*111*). We identify no significant increase in spinal cord [^{18}F]FAC accumulation in the EAE mice, suggesting that in this model, immune cells in the spinal cord increase glucose but not deoxynucleoside consumption. This result is supported by the lower percentage of leukocytes in the spinal cord relative to the brain of EAE mice that stain strongly for dCK. This data suggesting that immune cells at different anatomical locations have different metabolic needs is consistent with data showing a much larger increase in [^{18}F]FDG than [^{18}F]FAC consumption in the draining lymph nodes of a mouse rhabdomyosarcoma model (*91*).

Implications for Human Studies. Brain-infiltrating leukocytes contribute to neurological diseases, and can be treated with immunomodulatory drugs (*31*,*98*–*105*). Many immunomodulatory drugs cause significant side effects. In MS, the primary effects of these drugs on the immune system are assessed indirectly with MRI and clinical evaluations (*131*). PET assays with radiotracers that measure deoxynucleoside salvage could directly monitor the effect of these drugs on brain-infiltrating leukocytes. We demonstrate how this might work with the drug fingolimod. Both [^{18}F]FAC and [^{18}F]CFA measure deoxynucleoside salvage (*94*,*97*). [^{18}F]CFA works poorly in mice due to high plasma deoxycytidine levels but is resistant to deamination in humans (*97*,*127*). However, [^{18}F]CFA does not cross the BBB in humans, suggesting that a different radiotracer will need to be tested in humans. These could include the [^{18}F]FAC derivatives [^{18}F]-L-FAC and 2′-deoxy-2′-^{18}F-fluoro-5-methyl-β-L-arabinofuranosylcytosine, which are resistant to deamination (*126*). Additional studies would have to be conducted with these radiotracers to determine whether they cross the human BBB.

Chapter 3: Targeting deoxycytidine kinase, dCK, in deoxyribonucleoside salvage improves EAE clinical symptoms

3.1 Introduction

Multiple sclerosis (MS) is a chronic autoimmune disease in which cells of the immune system attack myelin in the central nervous system (CNS) leading, to neuroinflammation, demyelination, and neurodegeneration (*25*,*132–134*). MS pathology is likely driven primarily by T cells that recognize myelin autoantigens with additional involvement of B cells(*30*,*31*). Currently approved therapies for MS patients such as the anti-CD20 antibody ocrelizumab, the anti-CD52 antibody alemtuzumab, and the dihydroorotate dehydrogenase (DHODH) inhibitor teriflunomide are immunomodulatory and target various aspects of the immune system including B and T lymphocytes. These therapies can be effective, but they all cause significant side effects such as an increased risk of malignancy and infection, and they only cover a subset of patients (*132*). Additional therapeutic strategies to treat MS patients are needed.

The deoxyribonucleoside salvage pathway utilizes extracellular deoxyribonucleosides for intracellular metabolism, including the biosynthesis of deoxyribonucleoside triphosphates (dNTPs) for DNA synthesis. The salvage pathway complements dNTP production from the de novo pathway(*78*). In the salvage pathway, deoxyribonucleosides are transported across the cell membrane by concentrative and equilibrative nucleoside transporters and are subsequently phosphorylated by deoxycytidine kinase (dCK), the rate-limiting enzyme in this pathway(*78–81*). The PET radiotracers [^{18}F]FAC and [^{18}F]CFA can visualize the deoxyribonucleoside salvage pathway and quantify deoxyribonucleoside salvage activity in mice and humans, respectively (*94*,*97*).

In mice and in humans, the deoxyribonucleoside salvage pathway is enriched in lymphoid organs, including the bone marrow, spleen, and lymph nodes, and the development of T and B cells is blocked in dCK knockout mice (*81*,*94*,*97*). The deoxyribonucleoside salvage pathway is increased in T cells during activation in culture and in the spleen and lymph nodes in mouse models of systemic lupus erythematosus, autoimmune hepatitis, and inflammatory bowel disease and in a mouse model of anti-tumor immunity(*91*,*93*–*95*). In addition, we previously showed in the experimental autoimmune encephalomyelitis (EAE) model of MS that the deoxyribonucleoside salvage pathway is activated in the lymph nodes and spleen at one time point in the disease(*135*). These data suggest a potential functional role for deoxyribonucleoside salvage in autoimmune diseases including MS. Here we show that dCK is required for and can be targeted to block clinical symptoms in the EAE model of MS.

3.2 Methods

3.2.1 **Mice**

10-week-old, male and female C57Bl/6N mice were used for experiments at UCLA. 10-week-old female C57BL/6N mice were used for experiments at Crown Biosciences. 7-week-old female C57Bl/6J mice were used for experiments at Charles River Laboratories. All mice were purchased from Charles River Laboratories. All mouse studies at UCLA were approved of by the UCLA Animal Resource Committee. All mouse experiments at Crown Biosciences and Charles River Laboratories complied with local animal welfare guidelines.

3.2.2 **EAE induction**

$MOG_{35\text{-}55}$: Mice were acclimated to the animal facility for at least 7 days before starting the experiment. At mice were injected subcutaneously at two sites on the back with an emulsion of $MOG_{35\text{-}55}$ peptide and Complete Freund's Adjuvant (CFA; 100 µL/injection; 140 µg $MOG_{35\text{-}55}$/injection; Hooke Laboratories EK-2110). Two hours and again 24 hours later, the mice were injected intraperitoneally with pertussis toxin (80 ng; 100 µL).

At Crown Biosciences, mice were injected subcutaneously on each leg flank with an emulsion of $MOG_{35\text{-}55}$ peptide and CFA (100 µL/injection; 50 µg $MOG_{35\text{-}55}$/injection). Immediately after and again 48 hours later, the mice were injected intraperitoneal with pertussis toxin (200 ng; 100 µL).

At Charles Rivers Laboratory, mice were injected subcutaneously with an emulsion of $MOG_{35\text{-}55}$ peptide and CFA (100 µL/injection; 150 µg $MOG_{35\text{-}55}$/injection) at two sites on the lower back on Day 0 and two sites on the upper back on Day 7. Immediately after and again 48 hours after the first set of emulsion injections, mice were injected intraperitoneal with pertussis toxin (500 ng; 100 µL).

$MOG_{1\text{-}125}$: EAE was induced in mice with $MOG_{1\text{-}125}$ following the same protocol as was used at UCLA for inducing EAE with $MOG_{35\text{-}55}$ except that an emulsion of $MOG_{1\text{-}125}$ peptide and CFA was used (70 µg $MOG_{1\text{-}125}$/injection; Hooke Laboratories EK-2160).

All mice were scored following the standard clinical score that ranges from 0 to 5 where a score of 1 represents a limp tail; a score of 2 represents a limp tail and hind leg weakness; a score of 3 represents a limp tail and complete hind leg paralysis; a score of 4 represents a limp tail, complete hind leg paralysis, and partial front leg paralysis; and a score of 5 represents complete limb paralysis or death.

3.2.3 **[^{18}F]FAC PET/CT imaging**

[^{18}F]FAC PET/CT imaging was conducted as previously described (*135*). [^{18}F]FAC accumulation was quantified as percent injected dose per cubic centimeter except for the PET images of the vehicle- and TRE-515-treated mice. To account for the higher background levels of [^{18}F]FAC in the TRE-515-treated mice, in those experiments results are quantified as signal/background where background is muscle [^{18}F]FAC accumulation.

3.2.4 **Deoxyribonucleoside salvage ex vivo measurements**

Ex vivo measurements of deoxyribonucleoside salvage activity were conducted as previously described (*135*) except that cells were isolated from the lymph nodes and spleen.

3.2.5 **TRE-515 treatments**

TRE-515 (Trethera Corporation) was dissolved to a concentration of 12.5 mg/mL in 40% captisol (w/v) vehicle. Mice were treated daily with TRE-515 via oral gavage at a concentration and frequency of 75 mg/kg BID, 100 mg/kg QD, and 150 mg/kg QD. Treatments were initiated at Day 1 post-EAE induction (UCLA and Crown Biosciences), at Day 11 post-EAE induction when all the mice had reached a clinical score of 1 or greater (UCLA), or at Day 7 post-EAE induction when a third of the mice had reached a clinical score of 0.5 (Charles River).

3.2.6 **Immunohistochemistry**

Immunohistochemistry was conducted as previously described except that spinal cord sections were analyzed (*135*) . Spinal cord sections were stained with Luxol fast blue by incubating the tissue in Luxol fast blue solution overnight at 65 °C, differentiating the tissue with lithium carbonate solution, and counterstaining the tissue using cresyl violet solution per the manufacturer’s protocol (IHC World).

3.2.7 **Plasma deoxycytidine measurements**

EAE mice (14 days post-induction) were treated with vehicle or TRE-515 (75 mg/kg) and blood was collected at 4 hours post-treatment. Plasma deoxycytidine levels were analyzed as previously described(*97*).

3.2.8 **TRE-515 pharmacokinetic studies**

Naïve and EAE mice (14 days post-induction when all the mice had a clinical score>2.5) were treated with vehicle or TRE-515 (75 mg/kg) and brain, spinal cord, and blood were collected 1, 4, and 12 hours later. TRE-515 levels in the brain, spinal cord, and plasma were analyzed similar to previously described (*136*).

3.2.9 **Tetramer studies**

An APC-labeled MOG38-49 I-A(b) tetramer and control I-A(b) tetramer were obtained from the NIH Tetramer Core Facility at Emory University. EAE mice were treated with vehicle or TRE-515 (150 mg/kg, QD) starting on Day 1 post-EAE induction. On Day 10 post-EAE induction, cells from the inguinal, axial, and cervical lymph nodes were isolated by grinding the tissue between two glass slides in RPMI-1640 media containing 10% (v/v) FBS, glutamine (2 mM), and penicillin-streptomycin (100 U/mL). Cells were left unstained or were stained with either an APC-labeled MOG38-49 I-A(b) tetramer or control I-A(b) tetramer (NIH Tetramer Core Facility, Emory University; 18 μg/mL; 37 °C; 30 min) followed by a PE-labeled anti-mouse CD4 antibody (eBioscience 12-0042-81; 1.25 μg/mL; 4 °C; 30 min) and DAPI (1.2 μM). Cells were gated for single, live, CD4+ cells, and the percent tetramer positive cells for each sample was quantified.

3.2.10 **CyTOF experiments**

EAE mice were treated daily with vehicle or TRE-515 (150 mg/kg, QD) starting on Day 1 post-EAE induction. On Day 3 and Day 10 post-EAE induction, cells from the lymph nodes and spleens of the EAE mice were isolated as describe above. Red blood cells in the spleen were lysed using ACK lysis buffer. Cell were immunostained and analyzed by CyTOF with the antibodies in Table 1 as previously described(*137*) except that following the surface staining, cells were stained with the intracellular markers by fixing the cells with paraformaldehyde (2%, 10 min, room temperature), washing the cells twice with Perm-S buffer (2 mL; Fluidigm 201066), adding the intracellular markers in Perm-S buffer (1 hour, room temperature), and washing the cells twice with Maxpar Cell Staining Buffer (2 mL; Fluidigm 201068). Data was analyzed using the OMIQ software. Cells were gated for live, single, CD45+ cells and subsampled so that each sample had equal numbers of cells. Cells from each time point and organ system were analyzed separately using the FlowSOM algorithm, which creates self-organizing maps by clustering cells into nodes and further organizing the nodes by consensus metaclustering into 20 non-overlapping metaclusters. The Significance Analysis of Microarrays (SAM) software (number of permutations: 500; FDR cutoff: 0.1) was used to identify metaclusters whose levels differed significantly with TRE-515 treatments. The SAM software occasionally identified metaclusters with high variance and small differences between vehicle- and TRE-515-treated samples. To focus on the most significantly different clusters, we conducted T tests on each metacluster identified by SAM as significant, and only further analyzed those with a p-value<0.1. Median marker expression for a given marker represents the median expression of that marker across all samples.

Table 3. Markers and antibodies used for CyTOF

Label	Target	Clone	Source
89Y	CD45	30-F11	Fluidigm
115In	Ki67	SolA15	eBioscience
141Pr	TNFa	MP6-XT22	Fluidigm
142Nd	CD39	24DMS1	Fluidigm
143Nd	CD69	H1.2F3	Fluidigm
144Nd	IL2	JES6-5H4	Fluidigm
145Nd	CD4	RM4-5	Biolegend
146Nd	CD150	W19132B	Biolegend
147Sm	CD163	S15049I	Biolegend
149Sm	CD19	6D5	Fluidigm
150Nd	Ly6C	HK1.4	Biolegend
151Eu	Ly6G	1A8	Biolegend
152Sm	CD3e	145-2C11	Fluidigm
153Eu	CD335	29A1.4	Fluidigm
155Gd	CD25	3C7	Biolegend
156Gd	CD14	Sa14-2	Fluidigm
159Tb	TCRgd	GL3	Fluidigm
160Gd	CD62L	MEL-14	Biolegend
161Dy	iNOS	CXNFT	Fluidigm
162Dy	CD366	RMT3-23	Fluidigm
163Dy	CD138	281-2	Biolegend
164Dy	CD197	4B12	Fluidigm
165Ho	IFNg	XMG1.2	Biolegend
167Er	GATA3	TWAJ1	Fluidigm
168Er	CD8a	53-6.7	Biolegend
169Tm	TBET	4B10	Biolegend
170Er	CD192	475301R	R&D
171Yb	Granzyme B	QA16A02	Biolegend
172Yb	CD11B	M1/70	Biolegend
173Yb	CD44	IM7	Biolegend
174Yb	MHCII (IA/IE)	M5/114.15.2	Biolegend
175Lu	CD127	A7R34	Biolegend
176Yb	CD45R	RA3-6B2	Biolegend
209Bi	CD11C	N418	Fluidigm

3.2.11 **Red blood cell counts**

Blood (100 μL) was collected into K2-EDTA tubes from EAE mice Day 28 post-EAE induction following daily treatment with vehicle or TRE-515 (100 mg/kg, QD) starting on Day 1 post-EAE induction and was analyzed by a Vetscan hematology analyzer to quantify white blood cells, lymphocytes, neutrophils, monocytes, red blood cells, and platelet cells.

3.3 Results

3.3.1 **Deoxyribonucleoside salvage is elevated in lymph node T cells of EAE mice.**

EAE is the standard mouse model for studying the biology of and testing new therapies for MS. This model can be induced by injecting into C57Bl/6 mice an emulsion containing amino acids 35 – 55 of the mouse myelin oligodendrocyte glycoprotein (MOG_{35-55} peptide) and Complete Freund's Adjuvant (CFA) followed by two injections with pertussis toxin(*138*). This model can be induced in mice lacking B cells but requires T cells and is considered a B-cell independent model(*139*). Following injection of the MOG_{35-55}/CFA emulsion, mice remain asymptomatic for approximately 10 days, after which they manifest clinical phenotypes starting with a limp tail and leading to hind limb and forelimb paralysis. The severity of clinical phenotypes is quantified on a scale of 0 to 5, and the disease manifests as largely monotonic with limited remission.

We have previously shown that the deoxyribonucleoside salvage pathway is activated in the lymph nodes and spleen of MOG_{35-55} EAE mice at Day 14 post-EAE induction during which the mice were at peak disease(*140*), but whether deoxyribonucleoside salvage was activated in these tissues at other stages of the disease remained unknown. To determine in which EAE disease stages immune cells activate deoxyribonucleoside salvage, we induced EAE in female and male mice with the MOG_{35-55} peptide/CFA emulsion and imaged the mice with [^{18}F]FAC PET/CT pre-induction and at 7, 14, 21, and 28 days post-induction, time points that corresponded to no disease, presymptomatic disease, peak disease, disease maintenance, and mild remission, respectively. [^{18}F]FAC accumulation was quantified in the lymph nodes, spleen, spinal cord, and brain. [^{18}F]FAC accumulation was elevated in the spleen and lymph nodes of both the female and male mice starting as early as 7 days post-EAE induction and remained elevated through Day 28 post-EAE induction relative to pre-induction mice (**Fig. 3.1A, B; Fig. 3.2**), suggesting activation of the deoxyribonucleoside salvage pathway in immune cells of the secondary lymphoid organ throughout the EAE disease. [^{18}F]FAC accumulation was also elevated in the brains of female and male EAE mice at Days 7 and 14 post-induction and throughout disease, respectively, relative to pre-induction mice, likely due to brain-infiltrating leukocytes in these mice(*140*) and in the spinal cords of male but not female EAE mice (**Fig. 3.2, 3.3**).

EAE can also be induced in mice using an emulsion containing amino acids 1 – 125 of the mouse myelin oligodendrocyte glycoprotein (MOG$_{1\text{-}125}$ peptide) and CFA followed by two injections with pertussis toxin. This EAE disease fails to manifest in mice lacking B cells and thus is considered a B cell-dependent disease(*139*). MOG$_{1\text{-}125}$ EAE mice present with disease following a similar time course as the MOG$_{35\text{-}55}$ mouse model. We imaged MOG$_{1\text{-}125}$ EAE mice with [^{18}F]FAC PET/CT pre-induction and at Day 14 post-induction when the mice had reached peak disease. Similar to the MOG$_{35\text{-}55}$ EAE mice, MOG1-125 EAE mice had significantly higher [^{18}F]FAC accumulation in the lymph nodes and brain compared to pre-induction mice (**Fig. 3.4**). These data suggests that deoxyribonucleoside salvage is activated in the spleen and lymph nodes at multiple stages of disease in multiple EAE models.

Higher [^{18}F]FAC accumulation in the spleen and lymph nodes of EAE mice likely represent both a change in the cellular composition of these organs during disease and an increase in deoxyribonucleoside salvage activity in specific cell types residing in those organs. To quantify changes in deoxyribonucleoside salvage activity in specific cell types at different disease stages, we isolated CD11b innate immune cells, CD4 T cells, CD8 T cells, and CD45R (B220) B cells from the lymph nodes and spleens of MOG$_{35\text{-}55}$ EAE mice early (Days 7 – 14 post-EAE induction) or late (Days 21 – 28 post-EAE induction) in the disease course and measured deoxyribonucleoside salvage activity with [^{3}H]deoxycytidine. In cells from the lymph nodes, deoxyribonucleoside salvage activity was elevated in CD4 and CD8 T cells but not innate immune or B cells early in the disease course but returned to pre-induction levels at the later time point (**Fig. 3.1C**). In the spleen, deoxyribonucleoside salvage activity was significantly elevated in CD11b cells during late disease (**Fig. 3.5**). Deoxyribonucleoside salvage activity remained unaffected in the CD4 and CD8 T cells and B cells in the spleen at any point in the disease. Collectively, these results suggest that T lymphocytes in the lymph nodes activate deoxyribonucleoside salvage activity during immune activation in the MOG$_{35\text{-}55}$ EAE mouse model.

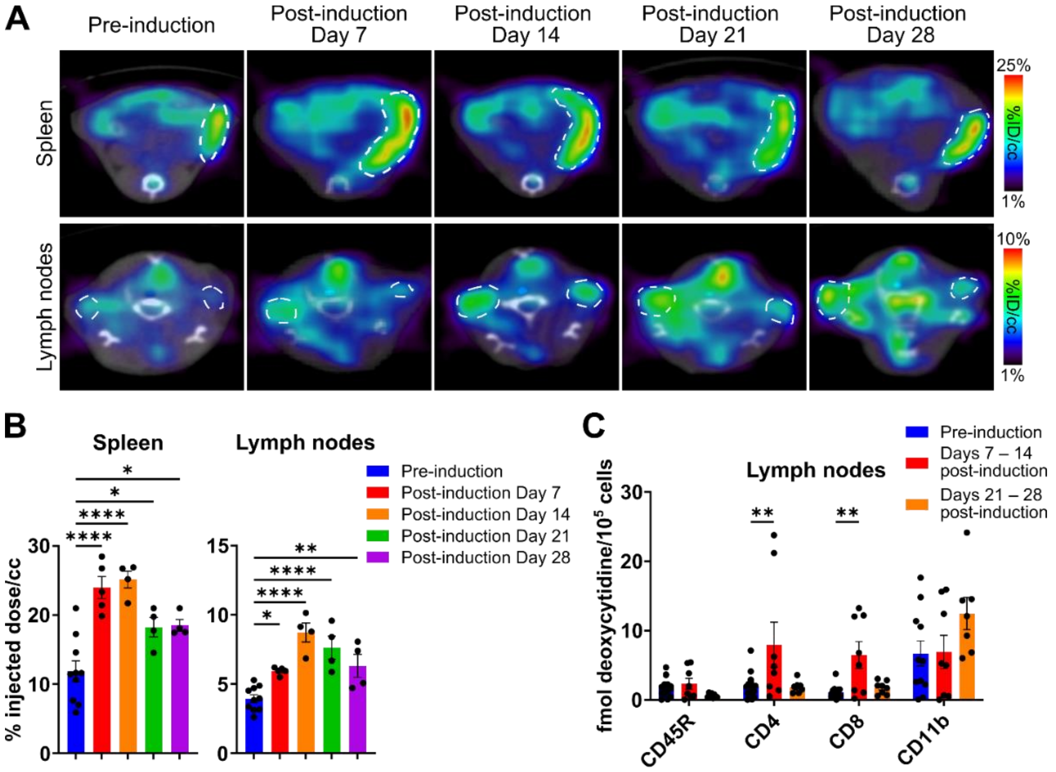

Figure 3.1. Deoxyribonucleoside salvage is upregulated in the spleen and lymph nodes throughout disease in MOG_{35-55} EAE mice.

(A) Representative transverse PET/CT images and (B) quantification of [^{18}F]FAC accumulation in the spleen and lymph nodes of EAE mice pre- and post-induction. Spleens and lymph nodes encircled in a white dotted line. (C) Ex vivo accumulation of deoxycytidine in immune cells isolated from the lymph nodes of EAE mice pre- and post-induction. Data in this and subsequent figures represent mean ± SEM. *: P<0.05; **: P<0.01; ****: P<0.0001.

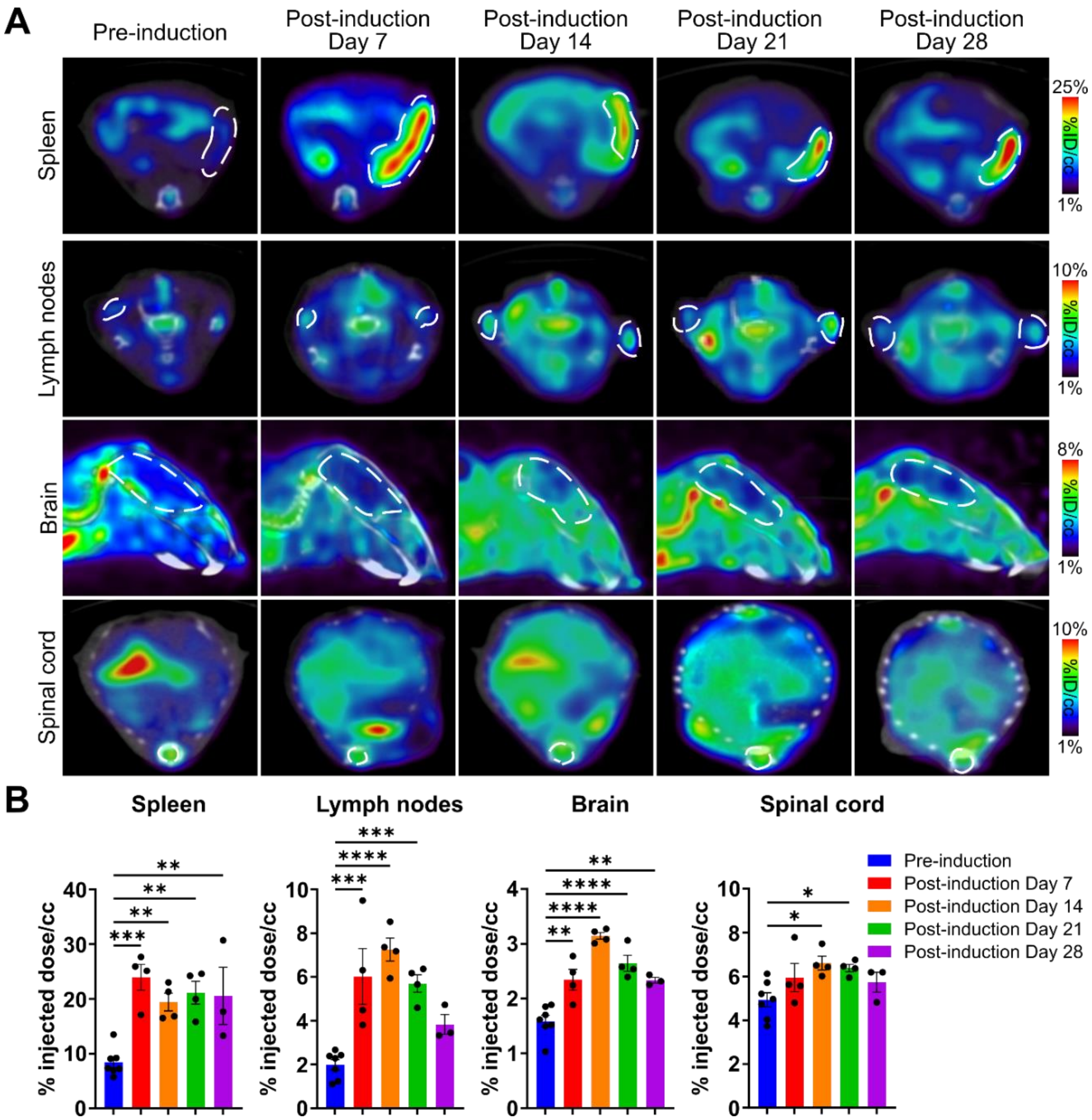

Figure 3.2. Deoxyribonucleoside salvage is upregulated in the spleen, lymph nodes, brain, and spinal cord at multiple time points throughout disease in male MOG_{35-55} EAE mice.

(A) Representative transverse PET/CT images and (B) quantification of [^{18}F]FAC accumulation in the spleen, lymph nodes, brain, and spinal cord of male EAE mice pre- and post-induction. Spleens, lymph nodes, brains, and spinal cords encircled in a white dotted line. *: P<0.05; **: P<0.01; ***P<0.001; ****P<0.0001.

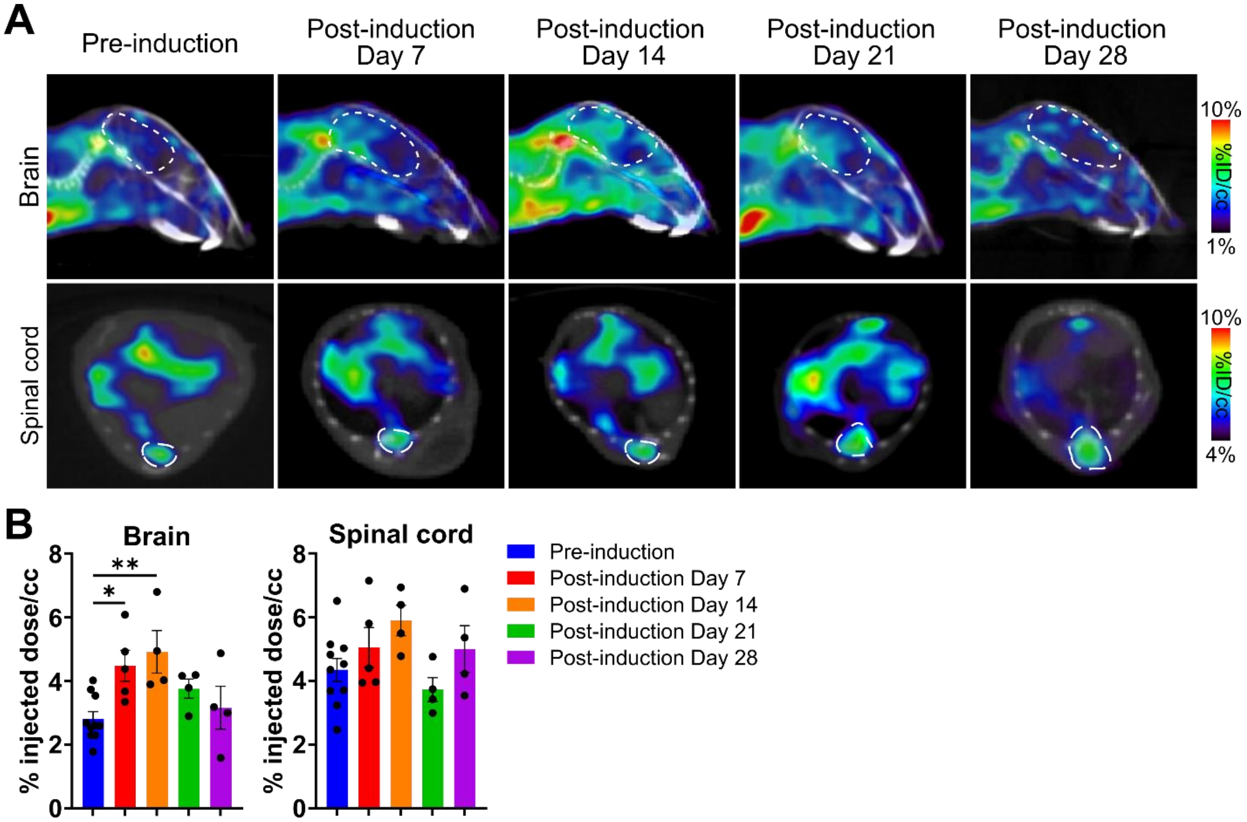

Figure 3.3. Deoxyribonucleoside salvage is upregulated in the brain but not the spinal cord at multiple time points throughout disease in female MOG_{35-55} EAE mice.

(A) Representative transverse PET/CT images and (B) quantification of [^{18}F]FAC accumulation in the brain and spinal cord of female EAE mice pre-induction and 7, 14, 21, and 28 days post-induction. Brains and spinal cords encircled in a white dotted line. *: P <0.05; **: P<0.01.

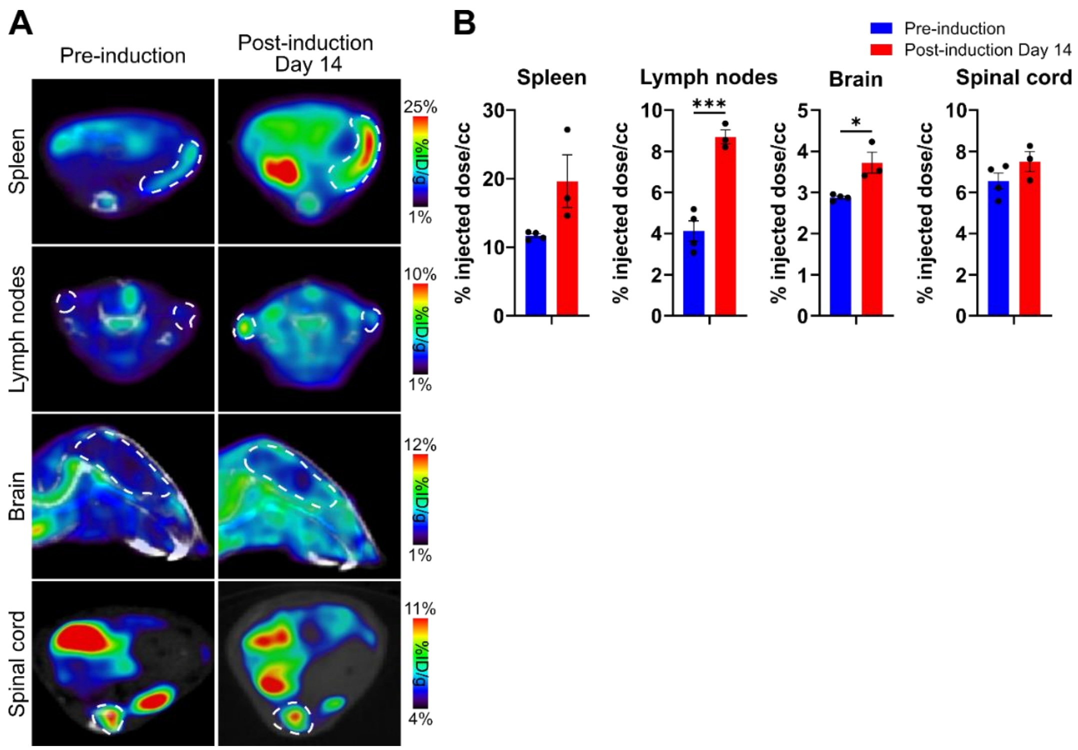

Figure 3.4. Deoxyribonucleoside salvage is upregulated in the lymph nodes and brain in MOG_{1-125} EAE mice at Day 14 post-induction.

(A) Representative transverse PET/CT images and (B) quantification of [^{18}F]FAC accumulation in the spleen, lymph nodes, brain, and spinal cord of MOG_{1-125} EAE mice pre-induction and 14 days post-induction. Spleens, lymph nodes, brains, and spinal cords encircled in a white dotted line. *: P<0.05; ***: P<0.001.

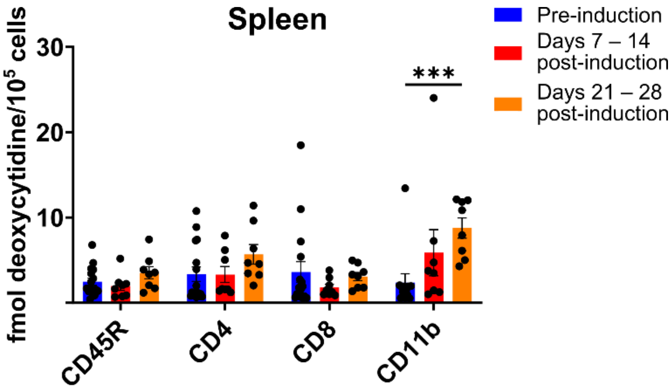

Figure 3.5. Deoxyribonucleoside salvage is upregulated in innate immune cells in the spleen in MOG_{35-55} EAE mice.

Ex vivo accumulation of deoxycytidine in splenocytes of EAE mice pre- and post-induction.

3.3.2 **TRE-515 blocks deoxyribonucleoside salvage activity in spleen and lymph nodes**

Our data demonstrating that CD4 and CD8 T cells increase deoxyribonucleoside salvage activity during periods of immune activation in EAE mice suggests a potential functional role for this pathway in the development of clinical symptoms in EAE. TRE-515 is a recently developed small molecule inhibitor of dCK, the rate-limiting enzyme in the deoxyribonucleoside salvage pathway. Analogues of TRE-515 blocks deoxyribonucleoside salvage in xenograft tumors(*130*,*141*). To evaluate whether TRE-515 blocks deoxyribonucleoside salvage activity in lymphoid organs, we treated mice with vehicle or TRE-515 (150 mg/kg) once and imaged the mice with [^{18}F]FAC PET/CT. TRE-515 blocked [^{18}F]FAC accumulation in the bone marrow and spleen (**Fig. 3.6A, B**) while having no effect following this acute dosing on the levels of major immune cell classes in these organs (**Fig. 3.6C**). The lymph nodes of these mice proved too small to accurately quantify a decrease in [^{18}F]FAC accumulation following TRE-515 treatment. TRE-515 at a dose of 75 mg/kg also blocked deoxyribonucleoside salvage activity as indicted by our PET results and increased plasma deoxycytidine levels (**Fig. 3.7A – C**), an expected result given that dCK is required for the cellular consumption of deoxycytidine from the plasma.

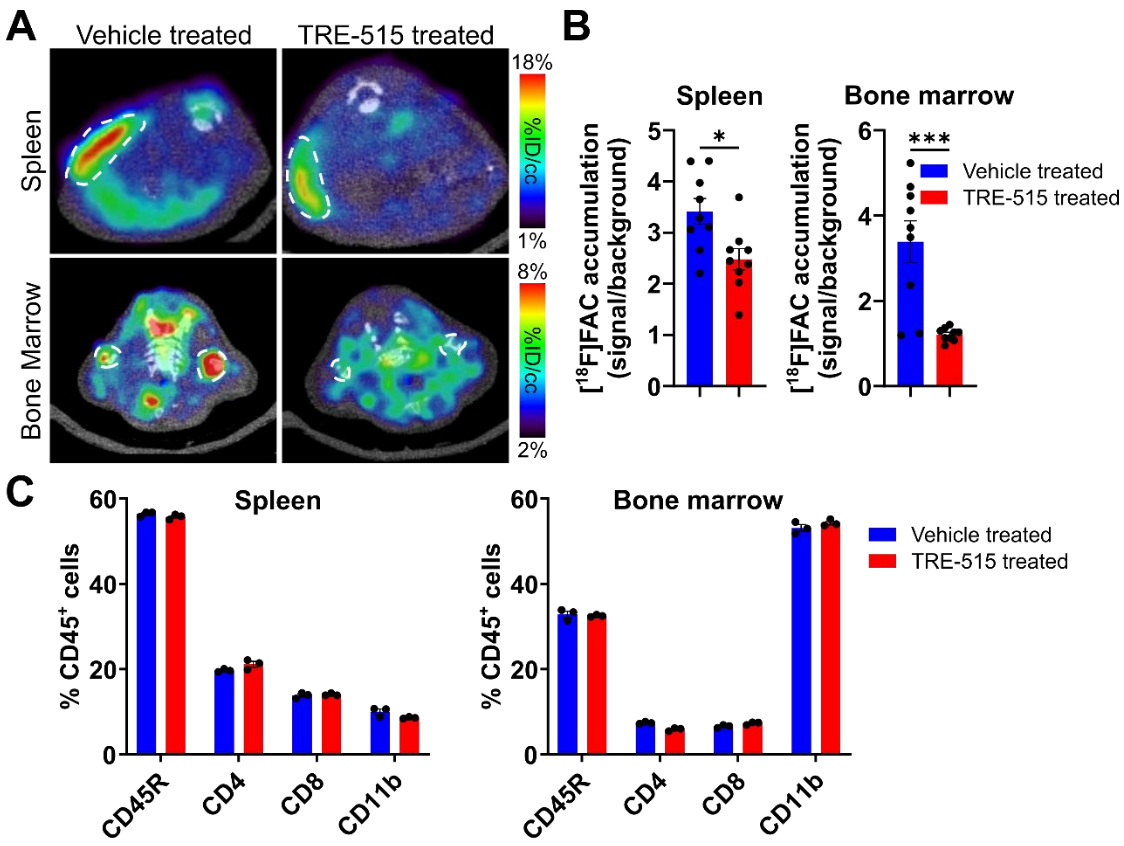

Figure 3.6. TRE-515 blocks deoxyribonucleoside salvage activity in the spleen and bone marrow.

(A) Representative transverse PET/CT images and (B) quantification of [^{18}F]FAC accumulation in the spleen and bone marrow of mice treated with vehicle or TRE-515 (150 mg/kg QD). Spleens and bone marrow encircled in a white dotted line. (C) Percent of CD45+ cells for each major immune cell class in the spleen and bone marrow of mice treated with vehicle or TRE-515 (150 mg/kg QD). *: $P<0.05$; ***$P<0.001$.

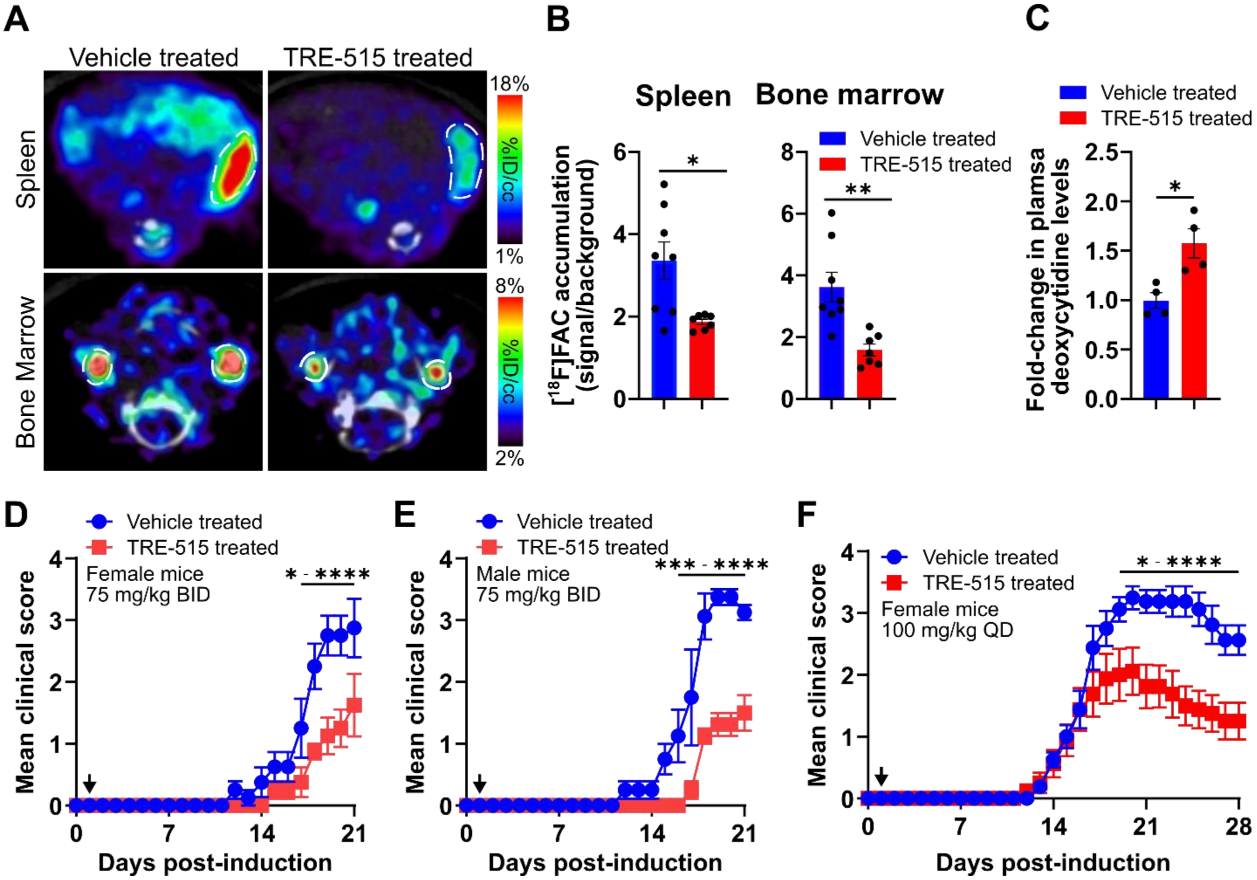

Figure 3.7. TRE-515 blocks clinical symptoms under multiple dosing regimens and in male and female mice.

(A) Representative transverse PET/CT images and (B) quantification of [^{18}F]FAC accumulation in the spleen and bone marrow of mice treated with vehicle or TRE-515 (75 mg/kg BID). Spleens and bone marrow encircled in a white dotted line. (C) Fold-change in plasma deoxycytidine levels in mice treated with vehicle or TRE-515 (75 mg/kg BID). Mean clinical scores of (D) female and (E) male EAE mice treated daily with vehicle or TRE-515 (75 mg/kg BID) starting on Day 1 post-induction. Arrows denote time point when treatments were started. (F) Mean clinical scores of female EAE mice treated daily with vehicle or TRE-515 (100 mg/kg QD) starting on Day 1 post-induction. Vehicle-treated mice in this experiment are the same as in Fig. 3A. Arrow denotes time point when treatments were started. *: P<0.05; **: P<0.01; ***: P<0.001; ****: P<0.0001.

3.3.3 **TRE-515 alleviates clinical symptoms of EAE mice.**

The ability of TRE-515 to target dCK and block deoxyribonucleoside salvage activity in the lymphoid organs of mice allowed us to test whether dCK and the deoxyribonucleoside salvage pathway contributes to and can be targeted to limit clinical phenotypes in EAE mice at different stages of disease. To evaluate whether targeting dCK prophylactically could limit disease phenotypes, we induced EAE in mice and treated the mice with vehicle or TRE-515 (150 mg/kg QD) starting the next day and through Day 21 post-EAE induction. The EAE mice treated with TRE-515 reached a lower clinical score at peak disease, had fewer symptoms overall, and developed symptoms later compared to EAE mice treated with vehicle (**Fig. 3.8A – C**). TRE-515 also limited clinical symptoms in the $MOG_{35\text{-}55}$ EAE model at once daily dosing of 100 mg/kg, at twice daily dosing of 75 mg/kg, and whether the EAE was induced in male or female mice (**Fig. 3.7D – F**). Additionally, TRE-515 limited clinical symptoms in the $MOG_{1\text{-}125}$ EAE model at once daily dosing of 150 mg/kg and 300 mg/kg but not twice daily dosing of 75 mg/kg (**Fig. 3.9**). We identified no side effects of the drug treatments under any of the treatment regimens. EAE clinical symptoms in the $MOG_{35\text{-}55}$ EAE model occur secondary to demyelination caused by infiltrating leukocytes in the CNS(*142*). TRE-515-treated EAE mice have fewer infiltrating leukocytes in the CNS and less demyelination compared with vehicle-treated EAE mice (**Fig. 3.8D**).

To evaluate whether targeting dCK therapeutically could limit disease progression, EAE mice were treated with vehicle or TRE-515 (150 mg/kg QD) starting when the mean clinical score for the mice reached 1, which in this experiment occurred on Day 11. Within five days of starting treatments, EAE mice treated with TRE-515 began to have significantly fewer clinical symptoms than vehicle-treated EAE mice; reduced clinical symptoms were maintained for the remainder of the treatment period, yielding fewer EAE symptoms overall (**Fig. 3.8 E, F**). Similar to the mice treated starting on Day 1 post-EAE induction, the mice treated starting on Day 11 post-EAE induction had fewer infiltrating leukocytes in the CNS and less CNS demyelination (**Fig. 3.8G**).

To evaluate the rigor and reproducibility of these experiments and to further validate and expand on these results, we had two contract research organizations – Crown Biosciences and Charles River Laboratories – evaluate the efficacy of TRE-515 in limiting clinical phenotypes using their established EAE protocols. Crown Biosciences treated MOG_{35-55} EAE induced using a similar protocol to our own with vehicle or TRE-515 (100 mg/kg QD) starting Day 1 post-EAE induction. Consistent with the results obtained from our own laboratory (**Fig. 3.7F**), in the experiment conducted at Crown Biosciences, the TRE-515-treated EAE mice had fewer symptoms at peak disease, had fewer symptoms overall, and developed symptoms later compared with vehicle-treated EAE mice (**Fig. 3.10A – C**). Charles River Laboratories induced their MOG_{35-55} EAE model by injecting a MOG_{35-55} peptide/CFA emulsion at Day 0 and Day 7 in contrast to our approach of just injecting the MOG_{35-55} peptide/CFA emulsion at Day 0. This double injection protocol yields an EAE disease that left untreated produces monotonically increasing symptoms without remission. In this experiment, mice were treated with vehicle or TRE-515 (75 mg/kg BID) starting on Day 8 post-EAE induction when at least a third of the mice showed symptoms. Consistent with the results obtained from our own laboratory (**Fig. 3.8E, F**), in the experiment conducted at Charles River Laboratories, TRE-515-treated EAE mice had fewer symptoms than vehicle-treated EAE mice (**Fig. 3.10D, E**). Additionally, half of the EAE mice treated with TRE-515 at Charles River Laboratories began to recover from their symptoms starting at Day 20 post-EAE induction and a third of those mice recovered from all symptoms and returned to a clinical score of 0. The TRE-515-treated EAE mice that showed recovery in this model had fewer infiltrating leukocytes in the CNS and less demyelination than the vehicle-treated EAE mice (**Fig. 3.10F**).

Collectively, our data – reproduced and expanded upon by independent laboratories – demonstrate that targeting dCK with the small molecule inhibitor TRE-515 can limit clinical symptoms in the EAE mouse model when treatments are started either at disease induction or when symptoms arise.

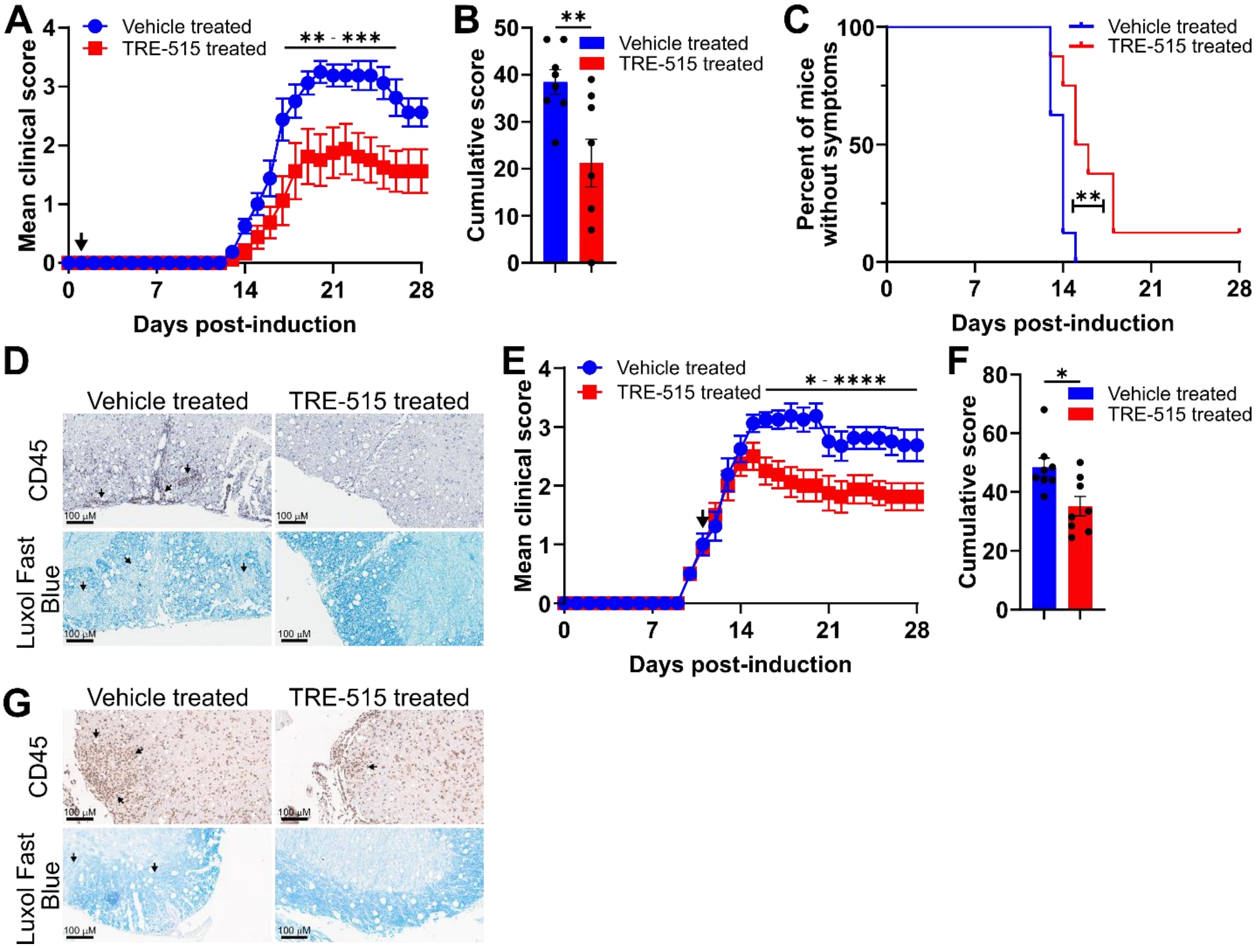

Figure 3.8. TRE-515 limits clinical symptoms in EAE mice.

(A) Mean clinical score, (B) cumulative score, and (C) percent of mice without symptoms of EAE mice treated with vehicle or TRE-515 (150 mg/kg QD) starting on Day 1 post-EAE induction. Arrow denotes time point when treatments were initiated. (D) Spinal cord sections from Day 21 post-induction EAE mice treated with vehicle or TRE-515 (150 mg/kg QD) starting on Day 1 post-EAE induction stained with a CD45 antibody (top) or with Luxol fast blue (bottom) to detect myelin. Arrows denote areas of significant leukocyte infiltration or demyelination. (E) Mean clinical score and (F) cumulative score of EAE mice treated with vehicle or TRE-515 (150 mg/kg QD) starting on Day 11 post-EAE induction when all the mice had reached a clinical score of 1 or greater. Arrow denotes time point when treatments were initiated. (G) Spinal cord sections from Day 28 post-induction EAE mice treated with vehicle or TRE-515 (150 mg/kg QD) starting at Day 11 post-EAE induction and stained with a CD45 antibody (top) or with Luxol fast blue (bottom) to detect myelin. Arrows denote areas of significant leukocyte infiltration or demyelination. *: $P<0.05$; **: $P<0.01$; ***: $P<0.001$; ****: $P<0.0001$.

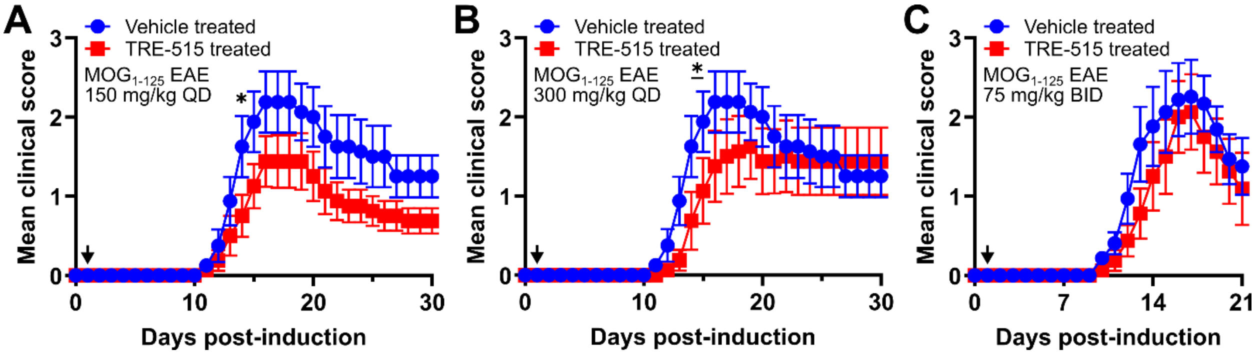

Figure 3.9. TRE-515 blocks clinical symptoms under multiple dosing regimens in MOG_{1-125} EAE mice.

MOG_{1-125} EAE mice were treated daily with vehicle or (A) TRE-515 (150 mg/kg QD), (B) TRE-515 (300 mg/kg QD), or (C) TRE-515 (75 mg/kg BID) starting on Day 1. Vehicle-treated mice in (A) and (B) are the same. Arrows denote time point when treatments were started. *: $P<0.05$.

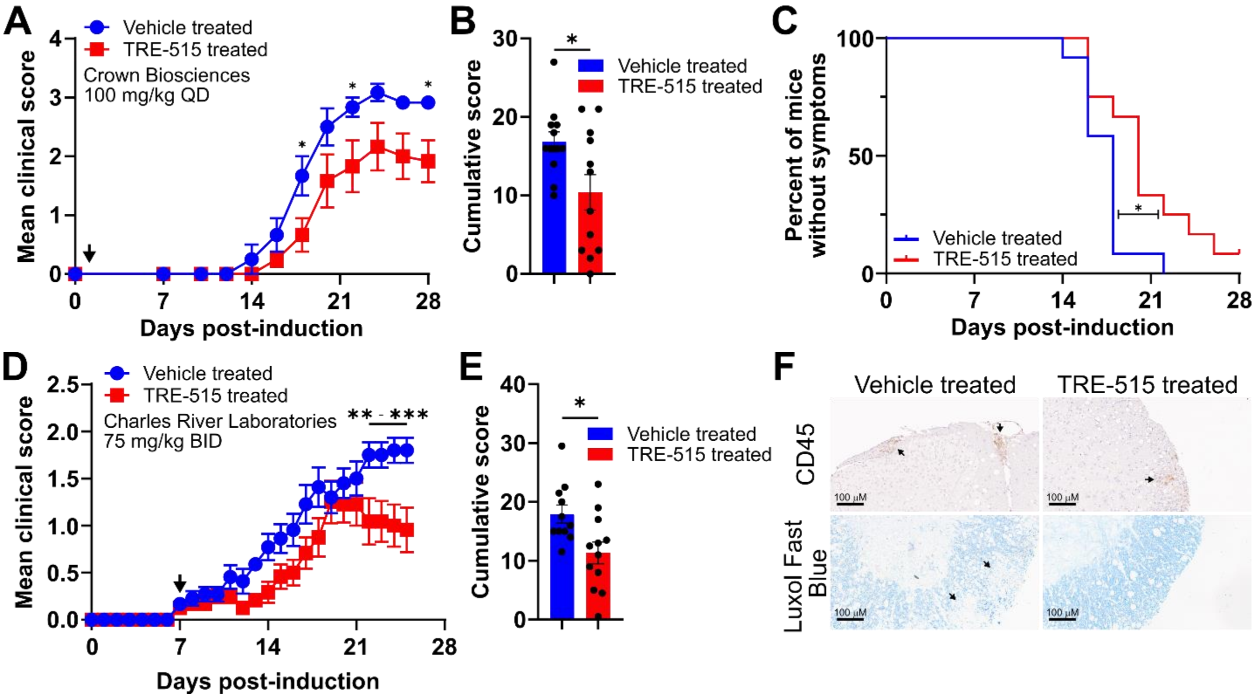

Figure 3.10. TRE-515 limits clinical symptoms in EAE mice.

(A) Mean clinical score, (B) cumulative score, and (C) percent of mice without symptoms of EAE mice treated at Crown Biosciences with vehicle or TRE-515 (100 mg/kg QD), starting on Day 1 post-EAE induction. Arrow denotes time point when treatments were started. (D) Mean clinical score and (E) cumulative score of EAE mice treated at Charles River Laboratories with vehicle or TRE-515 (75 mg/kg BID), starting on Day 7 post-EAE induction when at least a third of the mice had reached a clinical score of 0.5. Arrow denotes time point when treatments were started. (F) Spinal cord sections from EAE mice Day 25 post-induction treated as described in (D) at Charles River Laboratories and stained with a CD45 antibody (top) or with Luxol fast blue (bottom) to detect myelin. Arrows denote areas of significant leukocyte infiltration or demyelination. *: $P<0.05$; **: $P<0.01$; ***: $P<0.001$.

3.3.4 **TRE-515 blocks CD4 T and B cell activation-induced proliferation in EAE.**

Our data demonstrate that TRE-515 can block symptoms in EAE mice. TRE-515 could be having this effect by directly affecting cells either in the CNS or in the periphery. To test whether TRE-515 crosses the blood-brain and blood-spinal cord barrier, we treated naïve and EAE mice with TRE-515 and measured TRE-515 levels in the plasma, brain, and spinal cord of these mice 1, 4, and 12 hours later. Less than 4% and 7% of plasma TRE-515 levels reached the brain and spinal cord, respectively, independent of whether the mouse was induced with EAE (**Fig. 3.12**). These results combined with our earlier data showing that mice treated with TRE-515 have fewer infiltrating leukocyte in the CNS (**Fig. 3.8 D, G**) argue against the possibility that TRE-515 affects cells in the CNS to modulate EAE phenotypes and instead focused our attention on how TRE-515 affects immune cells in the periphery.

In EAE mice, CD4 T cells that express a T cell receptor that recognizes the $MOG_{35\text{-}55}$ peptide (MOG-specific CD4 T cells) are primary drivers of disease(*143*,*144*). Blocking these myelin-specific CD4 T cells could be one way in which TRE-515 limits clinical symptoms in this model. We quantified these cells using a fluorescently labeled tetramer that presents a peptide consisting of amino acids 38 – 49 of the mouse myelin oligodendrocyte glycoprotein ($MOG_{38\text{-}49}$ peptide) on a Class II MHC protein. As a control, we used a fluorescently labeled tetramer that presents a peptide not targeted by a mouse CD4 T cell. EAE induction caused a significant expansion of the MOG-specific CD4 T cells compared to naïve mice; this increase was blocked by TRE-515 treatment (**Fig. 3.11A**). The percent of CD4 T cells that bound to the control tetramer was not significantly affected by the EAE induction or the TRE-515 treatment (**Fig. 3.11B**) indicating that our results with the $MOG_{38\text{-}49}$ peptide-expressing tetramer were specific. These data suggest that TRE-515 blocks the expansion of MOG-specific CD4 T cells.

In addition to blocking the expansion of MOG-specific CD4 T cells, TRE-515 could affect other cells of the immune system to limit clinical symptoms in this model. For example, we show (**Fig. 3.11C**) that both CD4 and CD8 T cells in the lymph nodes increase deoxyribonucleoside salvage activity during early stages of EAE associated with immune activation. To more fully analyze the immune system in these experiments, we treated EAE mice with vehicle or TRE-515 (150 mg/kg QD) starting on Day 1 post-EAE induction, and profiled the immune system in the spleen and lymph nodes at Day 3 and Day 10 post-EAE induction using mass cytometry (CyTOF). We chose antibodies for our CyTOF experiment (**Table 1**) that labeled many of the major immune cell classes as well as their activation states. The results from each time point and organ system were analyzed by FlowSOM, an algorithm that performs unsupervised clustering of the cells to create self-organized maps containing nodes that represent different cell types and states and that then further groups these nodes into metaclusters, and SAM, a statistical method that identifies metaclusters whose abundances are significantly related to the TRE-515 treatment relative to the vehicle treatment(*145*,*146*).

In each organ and at each time point, the cells clustered on the maps into major immune cell classes (**Fig. 3.13**). These include cell clusters with high expression of CD3 and CD4 and low expression of CD8 representing CD4 T cells, cell clusters with high expression of CD3 and CD8 and low expression of CD4 representing CD8 T cells, cell clusters with high expression of CD19 and CD45R or CD138 representing B cells, and cell clusters with high expression of CD11b and low expression of CD3 representing innate immune cells.

In the lymph nodes samples from Day 3 post-EAE induction, the cluster of CD4 T cells organized into four metaclusters with greater than 0.5% abundance in the vehicle-treated mice: Metaclusters 11, 12, 15, and 16 (**Fig. 3.11C**). These metaclusters express markers representative of different stages of T cell activation (**Fig. 3.11D**). Metacluster 16 has high levels of the cell surface marker CD62L found on naïve T cells, low levels of the cell surface markers CD69, CD39, and CD44 found on activated T cells, and low levels of the proliferation marker Ki67 indicating that this metacluster likely represents naïve CD4 T cells. Compared to Metacluster 16, Metacluster 15 has elevated levels of CD69 and CD39 but similarly low levels of CD44 and Ki67 and similarly high levels of CD62L indicating that this metacluster likely represents very early activated T cells that have yet to induce proliferation. Compared to Metaclusters 16, Metaclusters 11 and 12 have lower levels of CD62L and higher levels of CD69, CD39, CD44, and Ki67 indicating that these metacluster likely represent activated, proliferating CD4 T cells. TRE-515 treatment had no effect on the percent of cells in the naïve CD4 T cell Metacluster 16 or the early activated but not proliferating CD4 T cell Metacluster 15 (**Fig. 3.11E**). However, TRE-515 significantly decreased the percent of cells in the activated and proliferating CD4 T cell Metacluster 11 and 12 (**Fig. 3.11E**). TRE-515 had no significant effect on the levels of any of the CD8 T cell metaclusters, although none of these metaclusters expressed high levels of CD69, CD39, CD44, or Ki67 suggesting that at this time point the CD8 T cells were not being activated or proliferating. These data suggest that TRE-515 blocks activation-induced proliferation in CD4 T cells in our model without affecting the levels of naïve CD4 T cells.

Additionally, in the lymph nodes samples from Day 3 post-EAE induction, the cluster of B cells organized into five metaclusters: Metaclusters 1, 8, 14, 17, and 18 (**Fig. 3.11F**). These metaclusters express markers representative of different stages of B cell activation and differentiation (**Fig. 3.11G**). Metacluster 1 expresses low levels of the cell surface marker CD69 that is expressed on activated B cells, the cell surface marker CD138 that is expressed at high levels on plasma cells, and low levels of Ki67 indicating that this metacluster likely represents naïve, non-activated B cells. Metaclusters 8 and 14 express higher but still intermediate levels of CD69 and CD138 and low levels of Ki67 indicating that these metaclusters likely represent different types of activating but not yet rapidly proliferating B cells. Finally, compared to Metacluster 1, Metaclusters 17 and 18 express elevated levels of CD69, CD138, and Ki67 and likely represent proliferating cells at or near the plasmablast stage of differentiation. TRE-515 had no effect on the percent of cells in the naïve B cell Metacluster 1 or the activating but not proliferating B cell Metacluster 8 and 14 (**Fig. 3.11H**). However, TRE-515 significantly decreased the percent of cells in the proliferating plasmablast Metaclusters 17 and 18. These data suggest that TRE-515 blocks B cell proliferation during B cell activation and differentiation in addition to blocking CD4 T cell activation-induced proliferation.

In the spleen samples from Day 3 post-EAE induction, TRE-515 had no effect on any of the metaclusters, including any of the CD11b innate immune metaclusters, except to significantly decrease the number of cells in Metacluster 14, a B cell metacluster that expresses high levels of CD69, CD138, and Ki67 similar to the proliferating plasmablast metaclusters identified to be affected by TRE-515 in the lymph nodes (**Fig. 3.14**).

In the lymph nodes samples from Day 10 post-EAE induction, the cluster of CD4 T cells organized into three metaclusters: Metacluster 8, 14, and 18 (**Fig. 3.15A**). Metacluster 18 expresses high levels of CD62L and low levels of CD69, CD39, CD44, and Ki67 likely representing naïve CD4 T cells (**Fig. 3.15B**). Compared to Metacluster 18, Metacluster 8 expresses lower levels of CD62L and elevated levels of CD69, CD39, CD44, and Ki67 likely representing activated and proliferating CD4 T cells. Compared to Metaclusters 8 and 18, Metacluster 14 expresses intermediate levels of CD62L, CD69, CD39, CD44, and Ki67 but high levels of the cell surface marker CD25. CD25 is a marker of regulatory CD4 T cells(*147*), and Metacluster 14 may represent regulatory CD4 T cells although to assign this with more confidence additional markers such as FoxP3 would be required. TRE-515 significantly increased the percent of cells in the naïve T cell Metacluster 18 while decreasing the percent of cells in the activated T cell Metacluster 8 (**Fig. 3.15C**). At this time point, TRE-515 had no effect on the percent of cells in CD4 T cell Metacluster 14 or the metaclusters representing B cells and CD8 T cells.

Similar to the Day 3 spleen samples, in the spleen samples from Day 10 post-EAE induction, TRE-515 had no effect on any CD11b innate immune cell cluster. TRE-515 did decrease the percent of cells in Metacluster 10, which consists of a CD4 T cell metacluster with low levels of CD62L, CD69, CD39, and Ki67 and high levels of CD44 likely representing memory T cells (**Fig. 3.16**).

In total, our tetramer and CyTOF data suggest that TRE-515 blocks B and CD4 T cell activation-induced proliferation early in the EAE disease course, leading to more naïve T cells and fewer memory T cells than in vehicle-treated EAE mice without decreasing the levels of other major immune cell types including naïve CD4 or CD8 T cells, naïve B cells, or CD11b innate immune cells. Notably, the lack of an effect of TRE-515 on major immune cell classes as demonstrated through our CyTOF data is consistent with additional results from the Crown Biosciences EAE mouse treatment experiment (**Fig. 3.17**). In that experiment, at the end of the 28-day treatment, total white blood cells, lymphocytes, neutrophils, monocytes, platelets, and red blood cells were counted from the blood of the vehicle and TRE-515-treated EAE mice. TRE-515 had minimal to no effect on the levels of any of these cell types.

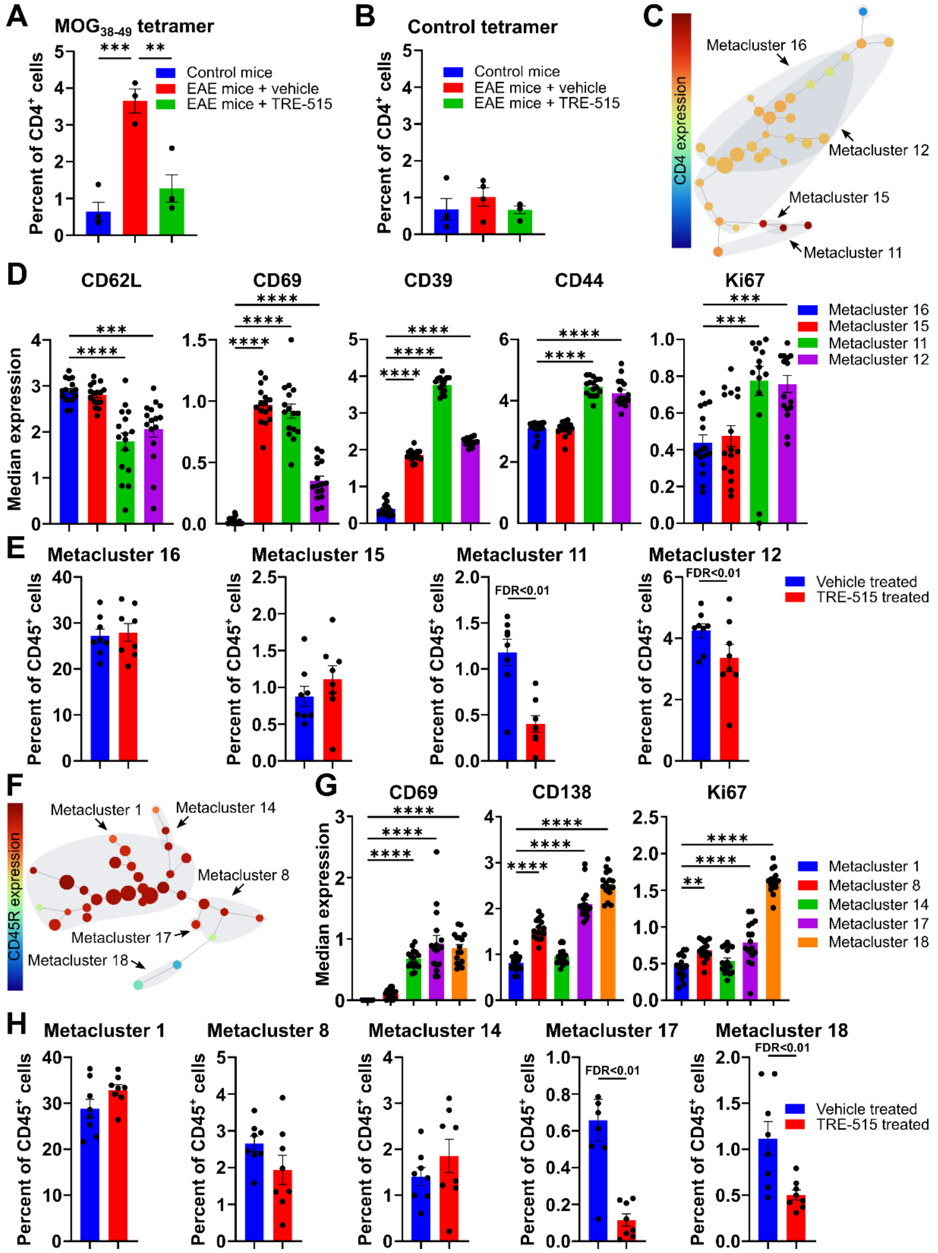

Figure 3.11. TRE-515 blocks B and CD4 T cell activation-induced proliferation in EAE mice.

(A) Percent of MOG38-49 tetramer and (B) control tetramer stained CD4 T cells in naïve mice, EAE mice treated with vehicle, and EAE mice treated with TRE-515 (150 mg/kg QD). In EAE mice treated with vehicle or TRE-515 (150 mg/kg QD): (C) CD4 T cell metaclusters in a map of lymph node cells analyzed by CyTOF. (D) Median expression levels of CD62L, CD69, CD39, CD44, and Ki67 among the T cell metaclusters. (E) Percent of cells in the T cell metaclusters. (F) B cell metaclusters in a map of lymph node cells analyzed by CyTOF. (G) Median expression levels of CD69, CD138, and Ki67 among the B cell metaclusters. (H) Percent of cells in the B cell metaclusters. **: P<0.01; ***: P<0.001; ****: P<0.0001.

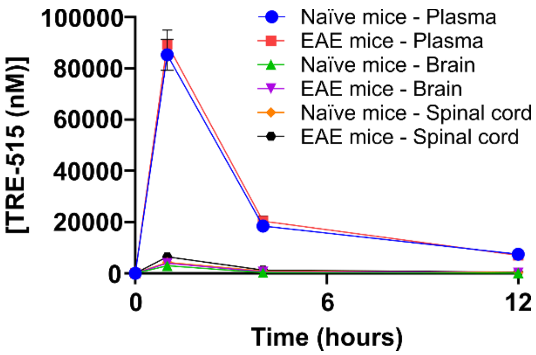

Figure 3.12. TRE-515 does not readily cross the blood-brain or blood-spinal cord barrier.

Naïve mice and EAE mice (all with a clinical score>2) were injected with TRE-515. Plasma, brain tissue, and spinal cord tissue were harvested 1, 4, and 12 hours later, and TRE-515 levels analyzed.

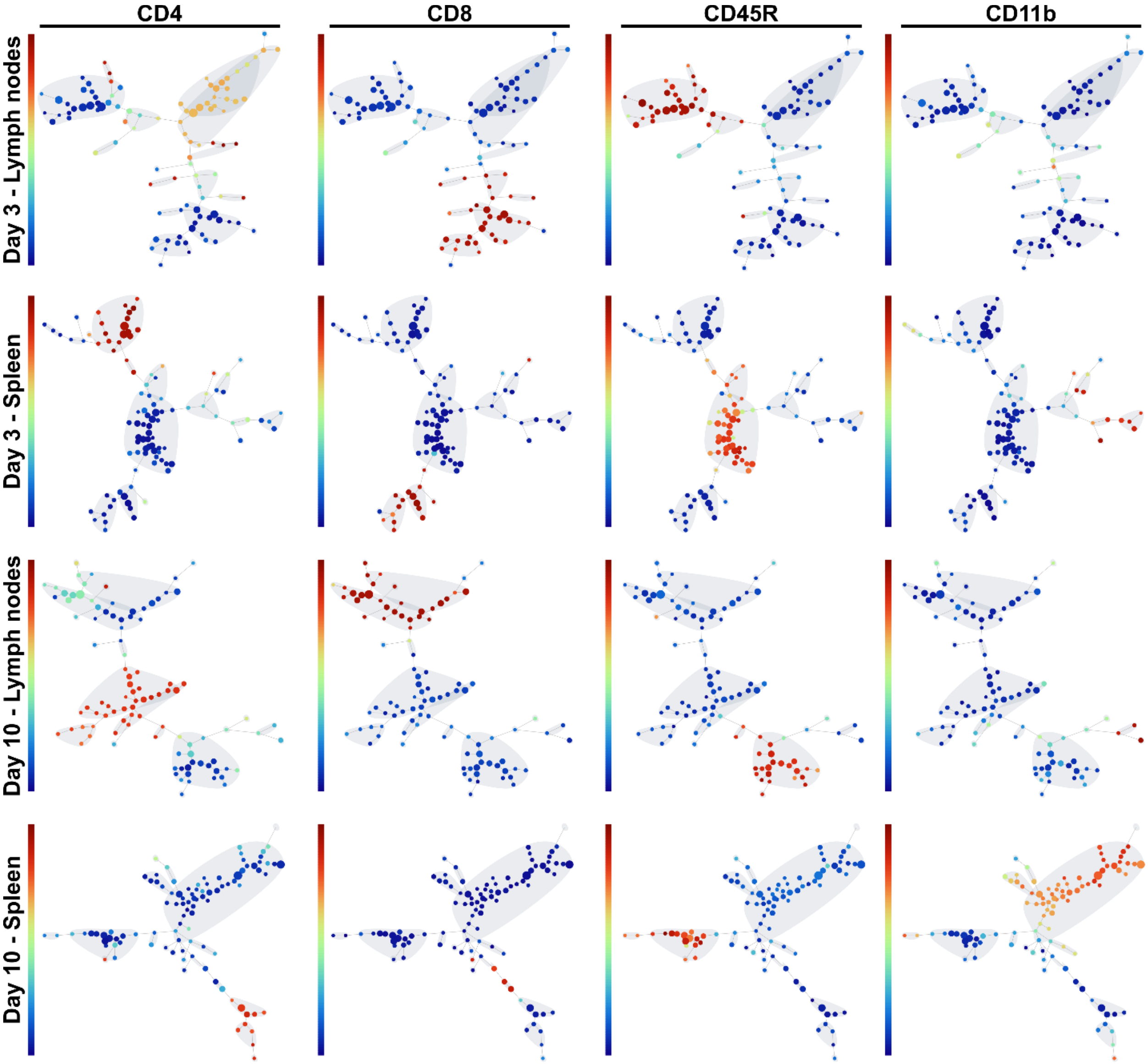

Figure 3.13. CyTOF results: self-organized maps spleen and lymph node cells of mice treated with vehicle or TRE-515 through day 3 and day 10 post-EAE induction.

Self-organized maps of cells from the spleen and lymph nodes of mice treated with vehicle or TRE-515 (150 mg/kg QD) through Day 3 and Day 10 post-EAE induction and analyzed by CyTOF. Maps colored by the intensity of CD4, CD8, CD45R, and CD11b staining of each node.

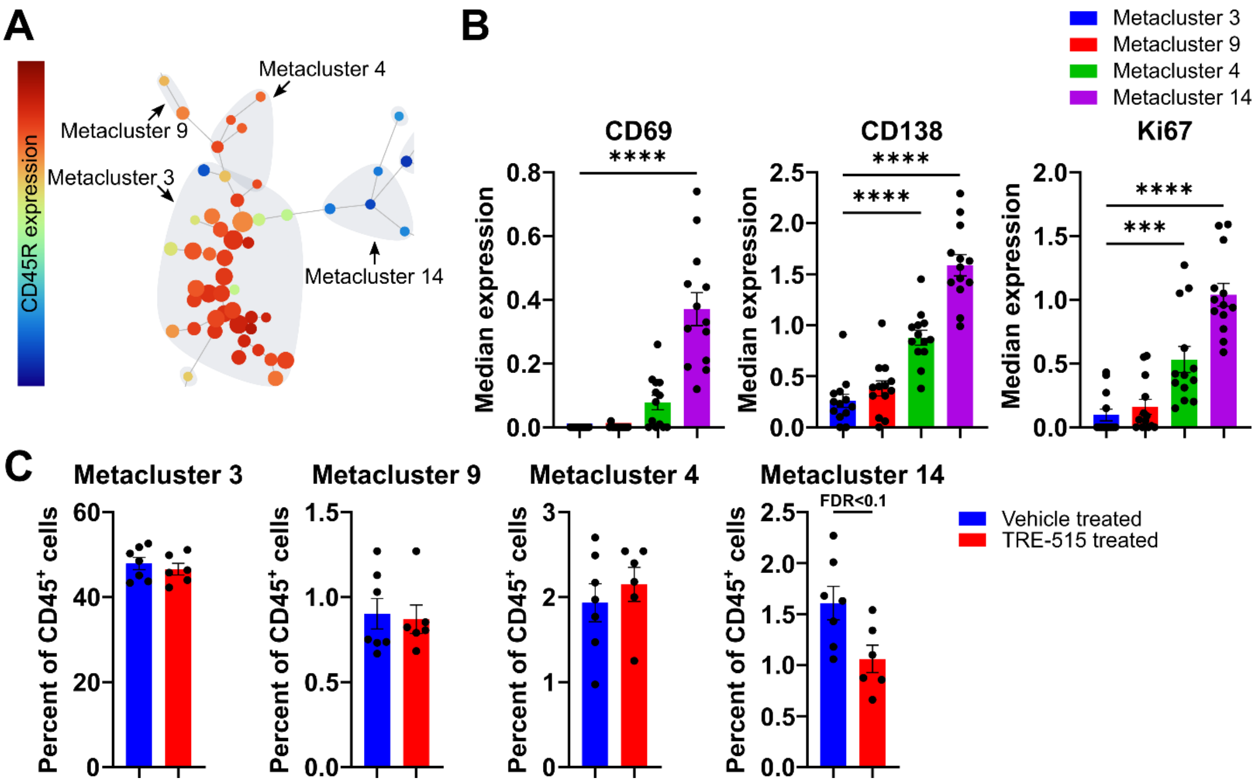

Figure 3.14. TRE-515 significantly decreases the percent of cells in a proliferating plasmablast metacluster in the spleen, three days post-EAE induction.

(A) B cell metaclusters from a self-organized map of splenocytes analyzed by CyTOF. (B) Median expression levels of CD69, CD138, and Ki67 in the four B cell metaclusters. (C) Percent of CD45+ cells in the B cell metaclusters. ***: $P<0.001$; ****: $P<0.0001$.

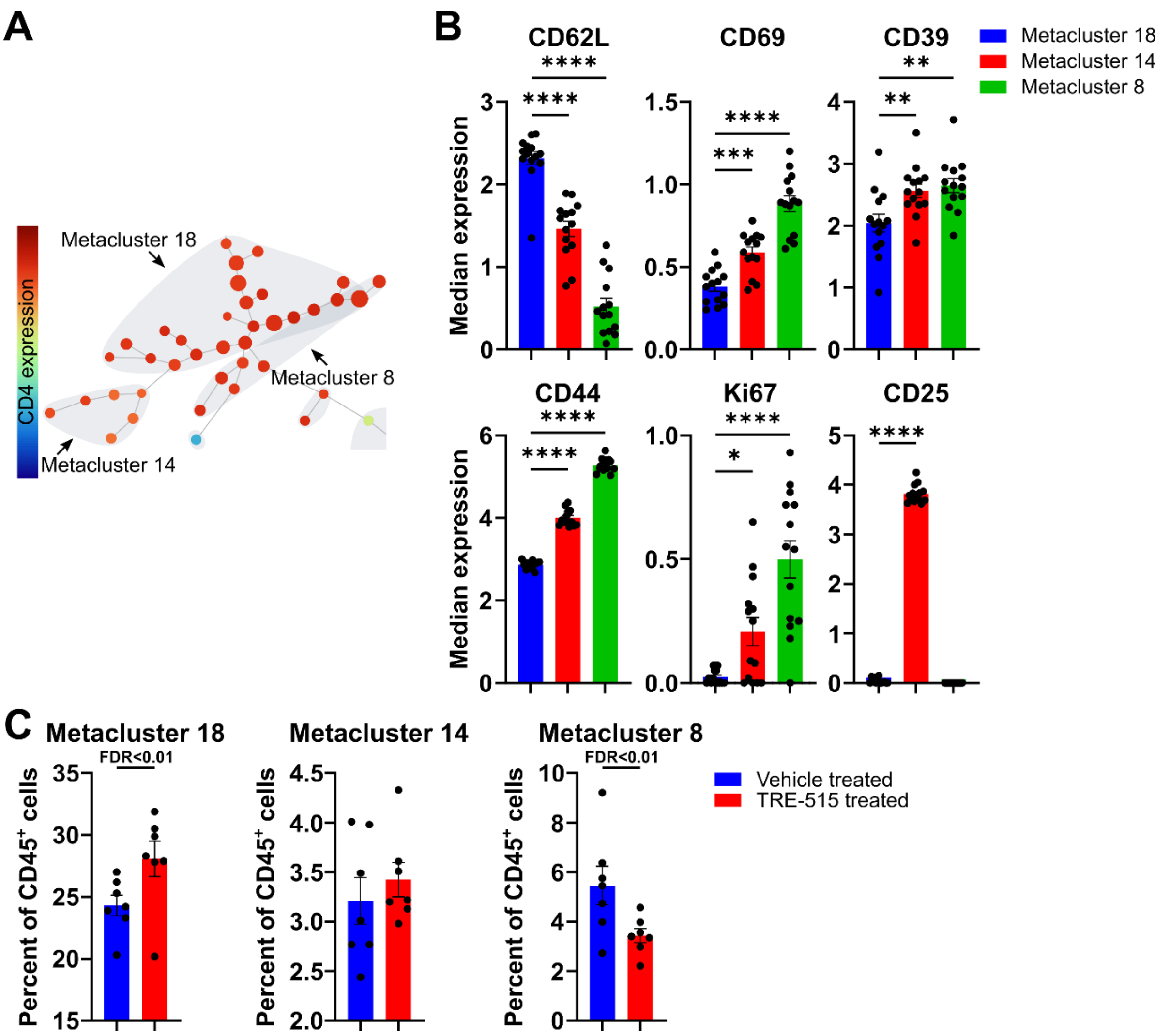

Figure 3.15. TRE-515 treatment significantly decreases the percent of cells in an activated CD4 T cells metacluster in the lymph nodes, 10 days post-EAE induction.

(A) T cell metaclusters from a self-organized map of cells from the lymph nodes analyzed by CyTOF. (B) Median expression levels of CD62L, CD69, CD39, CD44, Ki67, and CD25 in the three CD4 T cell metaclusters. (C) Percent of CD45+ cells in the CD4 T cell metaclusters. *: P<0.05; **: P<0.01; ***: P<0.001; ****: P<0.0001.

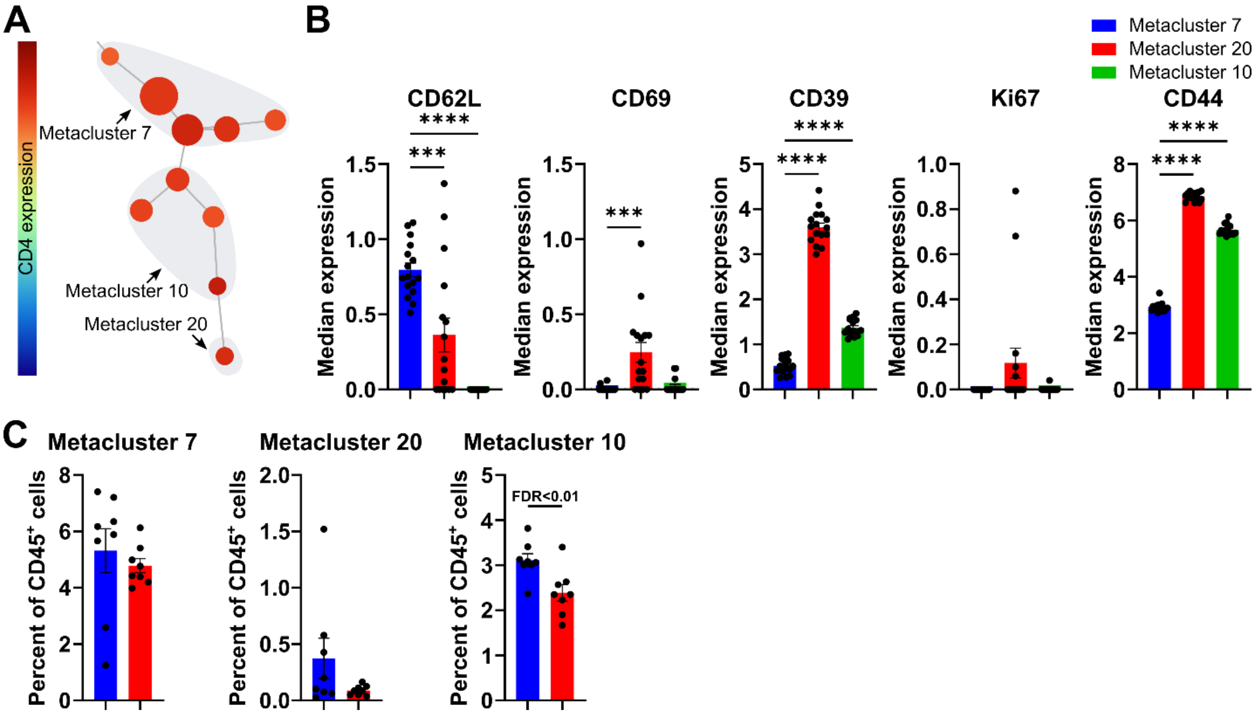

Figure 3.16. TRE-515 treatment significantly decreases the percent of cells in a memory CD4 T cell metacluster in the spleen, 10 days post-EAE induction.

(A) CD4 T cell metaclusters from a self-organized map of splenocytes analyzed by CyTOF. (B) Median expression levels of CD62L, CD69, CD39, Ki67, and CD44 in the three T cell metaclusters. ***: P<0.001; ****: P<0.0001.

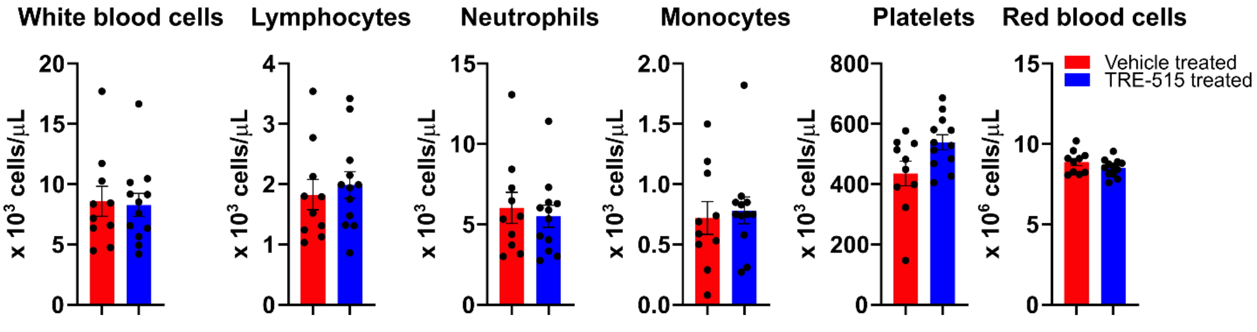

Figure 3.17. TRE-515 has minimal to no effect on the level of major cell types in the blood of mice.

Cell concentrations of white blood cells, lymphocytes, neutrophils, monocytes, platelets, and red blood cells in the blood of EAE mice treated for 28 days with vehicle or TRE-515 (100 mg/kg QD).

3.4 Discussion

Here we show that the dCK inhibitor TRE-515 limits the development of clinical symptoms and blocks CD4 T and B cell activation-induced proliferation in the MOG_{35-55} EAE mouse model. Activated CD4 T cells are key drivers of pathology in the MOG_{35-55} EAE model(*143*,*144*), and TRE-515 blocks the proliferation of activated CD4 T cells in this model at both Day 3 and Day 10 post-EAE induction. These data strongly suggest that blocking CD4 T cell activation-induced proliferation with TRE-515 blocks clinical symptoms in this model. Additionally, by Day 10 post-EAE induction, mice treated with TRE-515 have fewer memory CD4 T cells, an expected result of blocking CD4 T cell activation-induced proliferation. B cells likely do not contribute to clinical phenotypes in the MOG_{35-55} EAE model(*139*), so the fact that TRE-515 blocks B cell activation-induced proliferation, though notable and possibly important for other models, does not likely affect clinical phenotypes here.

Cells use two major pathways to synthesize dNTPs for DNA synthesis: the *de novo* nucleotide synthesis pathway and the deoxyribonucleoside salvage pathway(*78*). In the *de novo* nucleotide synthesis pathway, dNTPs are synthesized from consumed glucose and amino acids through a stepwise process. In the deoxyribonucleoside salvage pathway, complete deoxyribonucleosides are consumed from extracellular space and phosphorylated to dNTPs. Here we show that the proliferation of B and CD4 T cells in the lymph nodes and B cells in the spleen at Day 3 post-EAE induction can be blocked by inhibiting dCK, suggesting that these cells require deoxyribonucleoside salvage for their proliferation under these conditions. At the same time, we did not identify any innate immune cell types that are affected by dCK inhibition, even though a number of innate immune cell metaclusters have similar Ki67 levels as the proliferating B and CD4 T cell metaclusters. Similarly, dCK knockout mice develop normally except for a failure in lymphocyte development(*81*). These data suggest that innate immune cells and cells other than lymphocytes that divide during development do not require deoxyribonucleoside salvage. Why certain cell types require both deoxyribonucleoside salvage and the *de novo* nucleotide synthesis pathway while other cell types require only the *de novo* nucleotide synthesis pathway for deoxyribonucleoside synthesis remains unclear. However, studies show that thymidine can block the synthesis of deoxycytidine triphosphate in the *de novo* pathway via inhibition of the rate-limiting enzyme ribonucleotide reductase(*92*). High thymidine levels in the bone marrow and thymus of adolescent mice relative to other tissues likely shifts developing T and B cells to using the salvage pathway to maintain adequate deoxycytidine triphosphate levels(*92*). Whether the same is true for T and B cells activated in the lymph nodes of adult mice remains to be determined. Notably, at least in adolescent mice, thymidine levels in the lymph nodes are similar to thymidine levels in the thymus and bone marrow(*92*).

It remains to be determined how blocking dCK limits B and CD4 T cell activation-induced proliferation in the $MOG_{35\text{-}55}$ EAE mouse model. However, lack of dCK in rapidly proliferating Hardy fraction B-C B cell progenitors, DN3b T cell precursors, and nucleated erythroblast erythrocyte precursors yields lower levels of deoxycytidine triphosphates and promotes replication stress, cell cycle arrest at early S phase, and blocked proliferation(*92*). One hypothesis is that these same mechanisms are present in mature, naïve B and T cells and are activated in response to dCK inhibition during activation-induced proliferation of B and T cells. We do not identify a change in the total number of red blood cells in mice treated for up to 28 days with TRE-515, suggesting that deoxyribonucleoside salvage does not contribute significantly to maintaining erythrocyte levels after development. Testing this and other hypotheses will be the subject of future studies.

Enzymes in nucleotide synthesis pathways are effective targets for limiting clinical symptoms both in the MOG_{35-55} EAE mouse model as well as in patients with MS although to date all nucleotide synthesis inhibitors have targeted the *de novo* nucleotide synthesis pathway. The clinical inhibitor teriflunomide inhibits DHODH an enzyme in the *de novo* pyrimidine biosynthesis pathway that converts dihydroorotate to orotate(*148*). The clinical inhibitor cladribine is a prodrug that accumulates in cells and is phosphorylated to cladribine diphosphate and cladribine triphosphate. Cladribine likely has multiple mechanisms-of-action; one proposed mechanism is reversible inhibition of ribonucleotide reductase by cladribine diphosphate and triphosphate(*149*). Ribonucleotide reductase catalyzes the reduction of ribonucleotide diphosphates to deoxyribonucleotide diphosphates(*78*). How targeting enzymes in the *de novo* nucleotide synthesis pathway will compare to targeting dCK in the salvage pathway with respect to both efficacy and side effect profiles in MS patients will only be determined in clinical trials. However, TRE-515 blocks clinical EAE symptoms in the MOG_{35-55} model to a similar level as leflunomide, a metabolic precursor of teriflunomide(*148*), potentially suggesting similar efficacy. Additionally, $[^{18}F]$CFA PET imaging of human subjects demonstrates that deoxyribonucleoside salvage activity is largely concentrated in the lymphoid organs in humans(*97*), suggesting that on-target side effects in patients – if any exist – may be limited to effects on the immune system.

Conclusions:

Here we show that pharmacological inhibition of the deoxyribonucleoside salvage pathway can block B and CD4 T cell activation-induced proliferation and limit symptoms in a mouse model of the autoimmune disease MS, without decreasing the levels of other immune cell populations that include both naïve T and B cells and innate immune cells. B and T cells are important contributors to many different autoimmune diseases including systemic lupus erythematosus and inflammatory bowel disease(*150*,*151*). Although it remains to be formally tested, based on its mechanism-of-action in the EAE model, we hypothesize that TRE-515 may have efficacy across a wide range of autoimmune diseases and could represent a new type of immunomodulatory drug.

Chapter 4: Conclusions

In this dissertation, I studied the use of image-guided therapeutic intervention in autoimmune diseases. First, I determined that [^{18}F]FAC can be used to image brain-infiltrating leukocytes in EAE mice, a mouse model of MS and that [^{18}F]FAC can be used to monitor therapeutic intervention in this mouse model. Knowing [^{18}F]FAC accumulation is increased during disease in the MS mouse model, we tested whether targeting deoxyribonucleoside salvage, the metabolic pathway imaged by [^{18}F]FAC, might be be of functional relevance to MS. I determined, in multiple mouse MS models, that deoxyribonucleoside salvage is functionally important for MS and that targeting this pathway using a novel dCK inhibitor, TRE-515, led to significant clinical benefit for MS symptoms in mice.

Our immune system is a powerful biological ally to tackle foreign invaders in our body. However, sometimes our own immune system can turn against us and attack, believing that what is a foreign invader is actually our own body's tissues and organs. Autoimmunity is a complex system of immune cells orchestrating an immune response against our own body. Autoimmunity is thought to play a pathological role in more than 100 different diseases. The need to be able to image and quantify these pathological immune cells in the body is of importance and finding druggable biological targets that are well-studied to minimize side-effects from drugs for autoimmune diseases continues to be studied. We believe that the deoxyribonucleoside salvage pathway is a strong candidate for therapeutic success in autoimmune diseases. Not only is there an imaging strategy in place to monitor therapeutic intervention of TRE-515 in MS but this pathway has now been targeted in multiple models of MS, all of which have shown successful therapeutic benefit. MS is usually the first autoimmune disease that is studied and tested with new therapies and these therapies are often then translated to other autoimmune diseases such as lupus. We envision that our work in targeting deoxyribonucleoside salvage will also have therapeutic benefit other autoimmune diseases and that our imaging strategy that was demonstrated in this thesis work will help to provide personalized treatment options for patients with autoimmune diseases.

Chapter 5: Appendix

In this chapter, I will present some of the work that I have also done in which I coauthored throughout my time in my PhD. I have worked on imaging hepatic health and infiltrating leukocytes in a mouse model of autoimmune hepatitis and acetaminophen-driven liver failure, determining glucose uptake in neonatal heart regeneration, provided *in vivo* validation for radiotracers synthesized using a microfluidics platform, and validated the mechanism of decreased GLUT1 mRNA levels in lung cancer cells treated with a cyclin-dependent kinase inhibitor.

5.1 Imaging T cells and liver health in autoimmune hepatitis

Immune cell infiltration into the liver is a defining feature of autoimmune hepatitis and liver transplant rejection (*152*,*153*). T cells are known to play an important pathogenic role in liver damage. Various clinical methods can be used to detect for infiltrating T cells, however none of these methods provide the degree to which T cells are infiltrating into the liver and does not provide functional information about the cells of interest. For example, when a liver is damaged, the ability of the liver to convert proteins into energy or metabolize amino acids decreases. To test for this, clinicians detect for AST/ALT levels in the blood. If blood levels of both of these enzymes are high, then that suggests the liver is damaged. However, these tests do not inform us the extent of T cell infiltration into the liver and are cannot predict whether a disease is reversible. Furthermore, imaging techniques such as magnetic resonance imaging, computed tomography, and ultrasound provide anatomical results but do not tell us functional information regarding the pathogenic T cells. Currently, the gold standard method to detect for these infiltrating T cells is an invasive biopsy into the liver. However, biopsies can result in sampling error, high risks of complications, and can have heterogenous results. As such, a method to visualize and quantify liver-infiltrating T cells in autoimmune hepatitis and allograft rejection could improve our understanding of these diseases.

My role in this study was to assess the degree of immune infiltration in the concanavalin A model of autoimmune hepatitis. Concanavalin A is a mannose/glucose-binding lectin that is a known to activate T mitogen that activates the immune system (*154*). ConA will produce a CD4 T cell-dependent but CD8 Independent hepatitis (*154*,*155*). In this study, mice were induced with hepatitis when injected with conA. Hepatic-infiltrating leukocytes displayed a high proportion of CD4 T cells (64%) with additional infiltration from CD11b innate immune cells (9%), B220 B cells (18%), and CD8 T cells (13%) (**Fig. 4.1**). About 67% of the infiltrating leukocytes were positive for Ki-67, a marker of proliferation (**Fig. 4.1**).

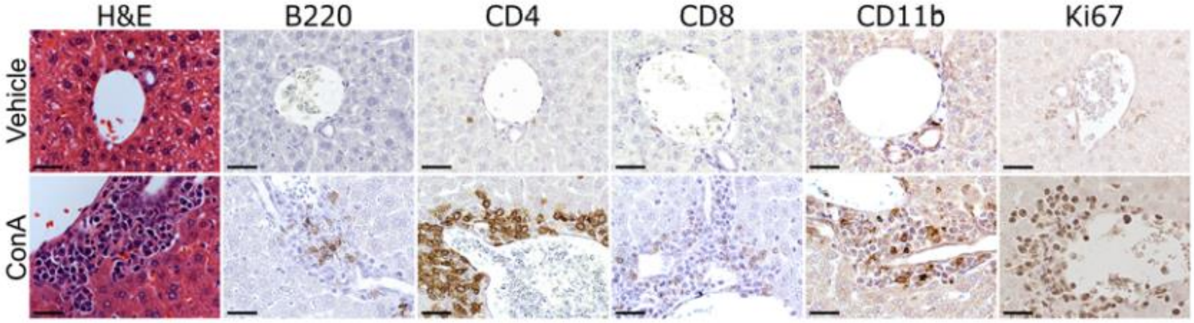

Figure 5.1 Immunostaining and histochemical staining of liver sections from vehicle-treated and conA-treated mice. Scale bars represent 50 microns

The goal of this study is to not only image hepatic-infiltrating leukocytes but to also determine liver health in response to autoimmune hepatitis. ^{18}F-FDG is a radiolabeled glucose analogue that is accumulated within a cell when the cell utilizes glucose metabolism ((*111*)). ^{18}F-FAC is accumulated when the deoxyribonucleoside salvage is utilized (*126*). Both glucose metabolism and deoxyribonucleoside salvage are upregulated during immune cell activation ((*91*,*94*,*95*,*111*)). ^{18}F-DFA measures ribose salvage activity, a pathway that is upregulated in liver hepatocytes ((*156*,*157*)). In results not shown here, hepatic ^{18}F-FDG, ^{18}F-FAC, and ^{18}F-DFA accumulation were affected in ConA-induced autoimmune hepatitis. ^{18}F-FDG, ^{18}F-FAC levels were increased in mice induced with autoimmune hepatitis. ^{18}F-DFA accumulation were decreased in mice induced with autoimmune hepatitis. These metabolic pathways are regulated by specific proteins ((*47*,*81*,*156*)) and changes in the levels of these protein in the liver can affect radiotracer accumulation in the liver. GLUT1 is a glucose transporter that is a major determinant of glucose consumption in activated lymphocytes (*158*). dCK is the rate-limiting enzyme in the deoxyribonucleoside salvage pathway (*81*)and RBKs is the key enzyme in the ribose salvage pathway (*156*). In addition to assessing the amount of immune cell infiltration in the livers of mice induced with autoimmune hepatitis, I also determined levels of GLUT1, dCK, and RBK in ConA-treated mice. ConA-treated mice immunostained for GLUT1 showed higher levels of membrane-localized GLUT1 in hepatic infiltrating leukocytes and in leukocyte proximal liver sinusoidal endothelial cells (Fig 4.2). RBKs protein levels were not present in the hepatic infiltrating leukocytes but was present in the liver hepatocytes. Hepatic infiltrating leukocytes expressed similar levels of dCK protein levels compared to vehicle-treated group.

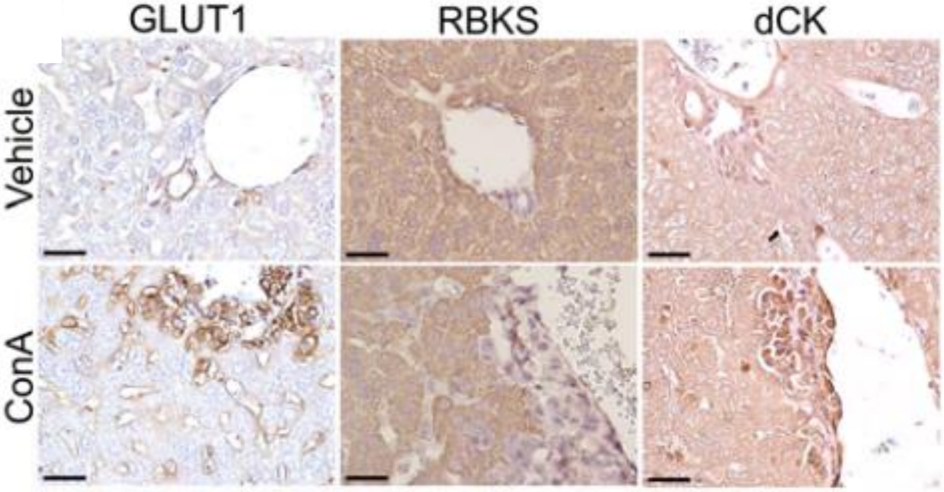

Figure 5.2 GLUT1, RBKS, and dCK immunostained vehicle and ConA-treated mouse liver sections. Scale bars represent 50 microns.

Additionally, I evaluated whether hepatic infiltrating leukocytes in patients with autoimmune hepatitis express dCK. To determine the deoxyribonucleoside salvage activity in hepatic infiltrating leukocytes in human patients with autoimmune hepatitis, I immunostained dCK in liver tissue sections from biopsies of patients with autoimmune hepatitis. The hepatic infiltrating leukocytes in the liver sections stained strongly for dCK (**Fig. 4.3**), suggesting that Pet radiotracers that measure deoxyribonucleoside salvage can potentially be used to quantify hepatic infiltrating immune cells in autoimmune hepatitis.

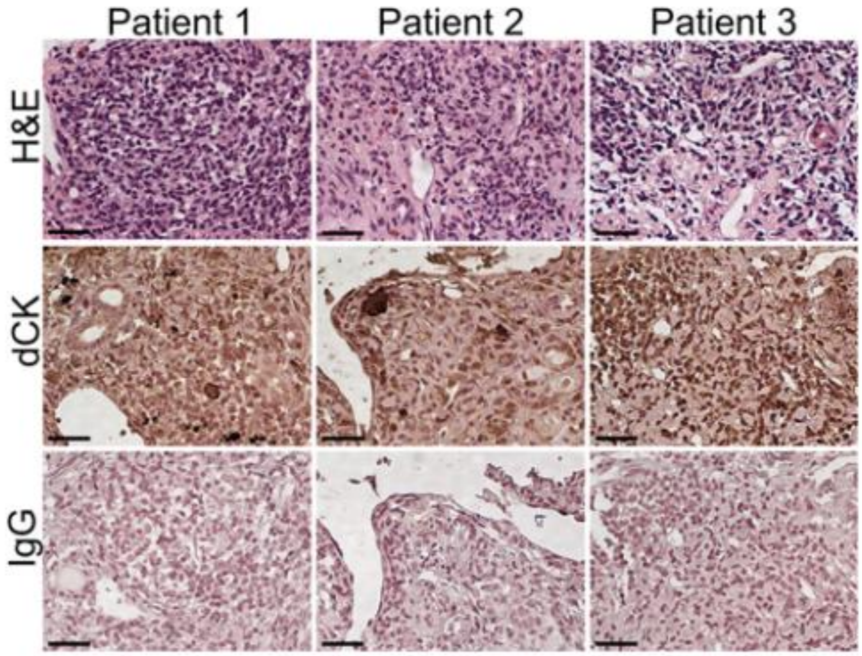

Figure 5.3 Hepatic infiltrating leukocytes in patients with autoimmune hepatitis express dCK. Histochemical and immunohistochemical analyses of liver biopsies from patients with autoimmune hepatitis. Scale bar represents 50 microns.

5.2 Monitoring drug-induced liver injury using ^{18}F-DFA

Drug-induced liver damage can be triggered by agents such as analgesics, tyrosine kinase inhibitors, and antibody-drug conjugates. A variety of techniques are utilized to assess liver health including liver-selective enzymes and metabolites (such as AST/ALT and bilirubin), liver biopsies, and CT/MRI/ultrasound imaging. While these all have clinical value, these methods do not provide a complete picture about the health of the liver, particularly, of the cells specifically damaged from the drugs. Furthermore, there's currently no clinically-relevant way to identify patients who will progress from acute liver failure to terminal liver failure. A technique to image functional aspects of the liver will provide helpful information for diagnosis and treatment of liver failure.

Recently, ^{18}F-DFA (^{18}F-deoxy-2-fluoroarabinose) was developed to measure ribose salvage activity in the liver. Because the ribose salvage pathway is most active in the liver, this leads to significant and specific accumulation of ^{18}F-DFA. Previously, it was shown that accumulation of ^{18}F-DFA was lower in mouse models of fatty liver disease and in mice treated with acetaminophen at one time point. Whether or not PET imaging can be used to image liver injury and failure remains to be determined.

^{18}F-DFA is not approved for human use yet but human hepatocytes can be studied in culture and engrafted into mice. My role in this study was evaluate the levels of ribose salvage activity in human hepatocytes to determine whether ^{18}F-DFA can be use for human studies of liver health. Isolated mouse and human hepatocytes were cultured and tested for ribose salvage activity using a tritium uptake assay. Mouse and human hepatocytes in culture consumed similar levels of ribose at a similar rate (**Fig. 4.4 A**). Human hepatocytes engrafted into mice can repopulate a mouse liver. Immunohistochemical staining for FAH enzyme, an enzyme that is only present in human hepatocytes, suggests that over 71% of the mouse liver are of human origin (**Fig. 4.4 B**). Accumulation of ^{18}F-DFA in livers of control mice or mice engrafted with human hepatocytes were indistinguishable (**Fig. 4.4 C**). How ^{18}F-DFA accumulates in humans will depend on the ribose salvage activity in the liver and other organs in the body. Together, these results suggest that PET imaging with ^{18}F-DFA could provide important liver function in humans.

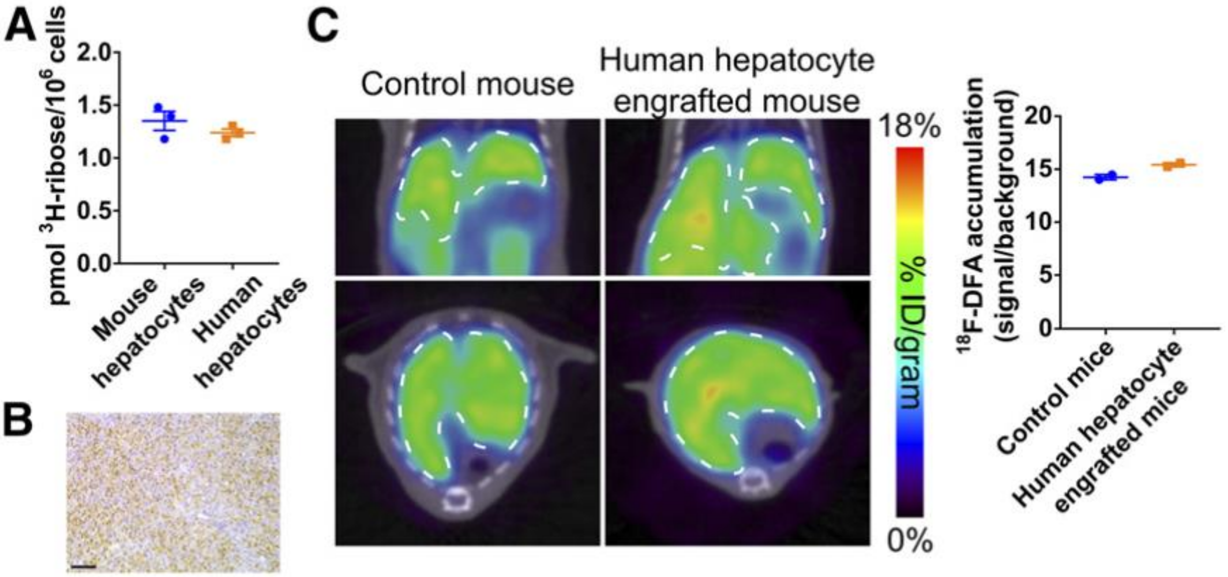

Figure 5.4. Ribose salvage activity in mouse and human hepatocytes.

5.3 Glucose metabolism in neonatal heart regeneration

Heart disease is one of the leading causes of death in the world, in part due to the fact that the heart is one of the least regenerative organs. Damage of cardiomyocytes in the heart leads to workload increase of the remaining cardiomyocytes. Studies have shown that postnatal cardiomyocytes are able to renew at a detectable rate. During the first few days of life, a neonatal heart can regenerate up to 15% of its heart muscles. However, the mitotic activity of the cardiomyocytes during the fetal stages is lost shortly after birth. This loss in regenerative capacity is affiliated with a metabolic switch of energy source from glucose to fatty acids. Not much is known about whether or not and how glucose can impact regeneration of the heart *in vivo*.

My role in this study was to validate and quantify the uptake of glucose in GLUT1 transgenic hearts in mice pups at different stages of development. One of ways in which we can study glucose metabolism is through the use of a glucose analogue, ^{18}F-FDG. Since the mice that we used were too small to image on a PET/CT scanner, we utilized autoradiography to study the distribution and uptake of glucose in neonatal hearts. 1 hour prior to tissue processing, mice were injected with injected with 3.33 MBq of ^{18}F-FDG. At time point, hearts of mouse pups were removed and sliced at 7micron thickness for analysis. ^{18}F-FDG accumulation was quantified and signal was normalized to the amount of probe injected for each mouse pup. Results indicate that Glut1 transgenic hearts accumulate 2.6-fold more ^{18}F-FDG at P2 and that accumulation decreases after P4 stage of the mouse pup (**Fig. 4.5**).

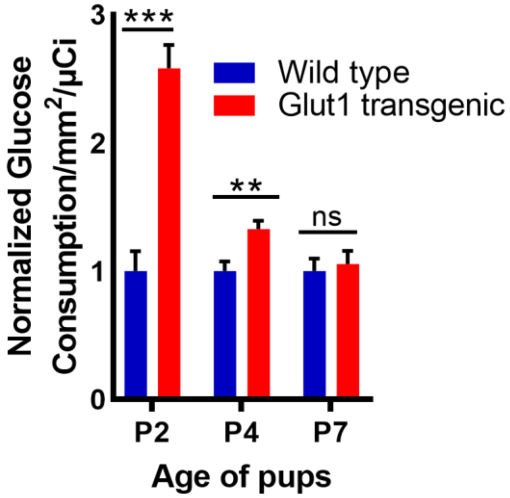

Figure 5.5. ^{18}F-FDG heart glucose consumption of mouse pups at different stages of development in wild type and Glut1 transgenic mice.

5.4 *In vitro* and *in vivo* validation of [^{18}F]FET synthesis using microdroplet radiosynthesis

Preparation of radiotracers for PET imaging is a complicated and expensive process that requires trained personnel, operation of expensive automated radiosynthesis equipment, and use of expensive precursors. Conventional setup for the synthesis includes carrying out chemical reactions in milliliter volume scales and using large amounts of reagent amounts are needed to achieve yield within a short amount of time. Furthermore, in [^{18}F]fluoride chemistry, large amounts of radioactivity is needed to achieve a high molar activity (*159*). Together, these components contribute to the inefficient use of resources for studies that require a small of radiotracers, such as preclinical imaging or even for single clinical PET scan.

Emerging microfluidic radiosynthesis techniques require less reagent amounts and radionuclide and can be performed using bench top sized instruments. Microscale reactions are cheaper and tend to be synthesized much faster than standard methods. Due to use of low precursor mass, crude products can be purified with more simple methods such as analytical-scale high-performance liquid chromatography. In this study, a simple and rapid method for [^{18}F]FET synthesis using a microvolume droplet technique. For this study, I helped to determine cancer cell lines that upregulated tyrosine metabolism and to set up mice tumor models to test different molar activities of microdroplet synthesized [^{18}F]FET.

In order to visualize xenograft tumors when imaging with[^{18}F]FET, the signal of the tumor should be above the background of the surrounding organs. To do that, we first determined which types of cancer cell lines utilized tyrosine metabolism. Different types of cancer cell lines were screened to for tyrosine metabolism using *in vitro* an [^{18}F]FET uptake assay. Results indicated that HCC827, a lung cancer cell line, accumulated [^{18}F]FET at higher levels compared to other cancer cells lines. Results of the uptake was also confirmed when [^{18}F]FET accumulation was blocked when cold FET was added, suggesting that the accumulation of [^{18}F]FET in HCC827 cells are specific (**Fig. 4.6**). To test whether different molar activities of microdroplet synthesized [^{18}F]FET will have an impact on imaging contrast, male NOD *scid* gamma (NSG) mice were engrafted with the lung cancer cell line (HCC827), injected with different molar concentrations of microdroplet synthesized [^{18}F]FET and dynamically imaged on the HiPET imaging system (**Fig. 4.7)**. Results suggests no differences were observed in tumors imaged with lower [^{18}F]FET molar activities compared to higher molar activities (**Fig. 4.8**), indicating that lower molar activities of [^{18}F]FET can be synthesized using the microdroplet synthesized approach and still be easily visualized for PET imaging.

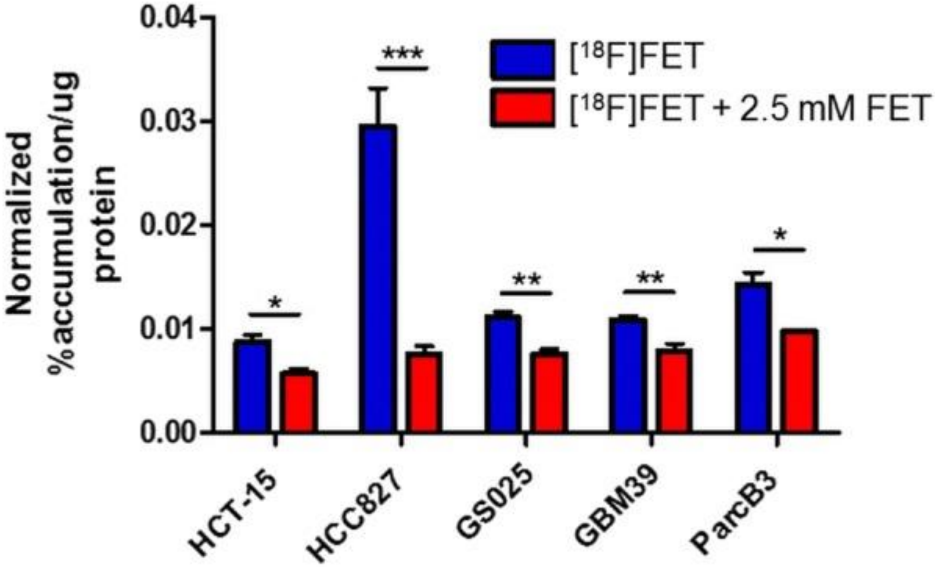

Figure 5.6. [^{18}F]FET accumulation in different cancer cell lines.

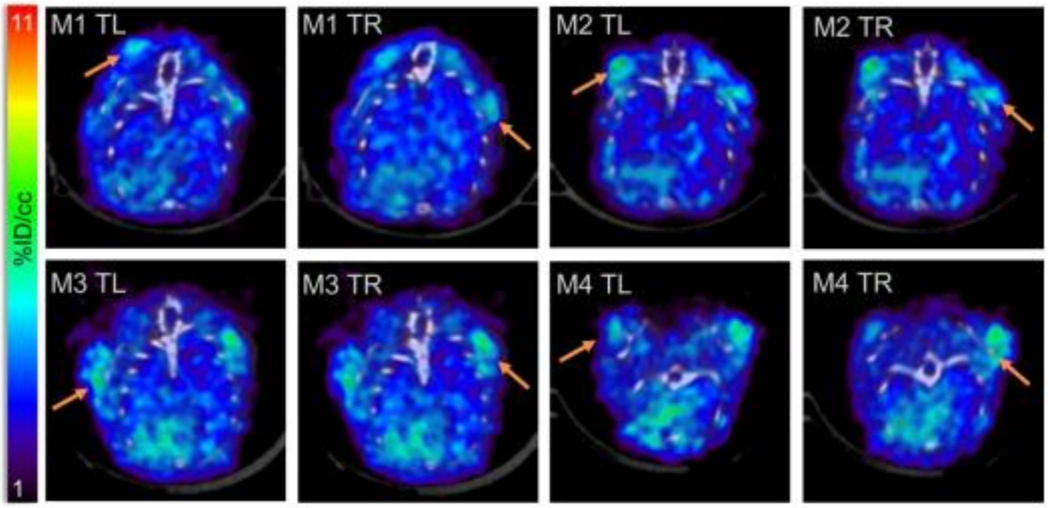

Figure 5.7. Transverse PET/CT of NSG mice bearing HCC827 xenografts. Arrow indicates tumor. M 1-4 represents the mouse number. TL: left shoulder tumor. TR: right shoulder tumor.

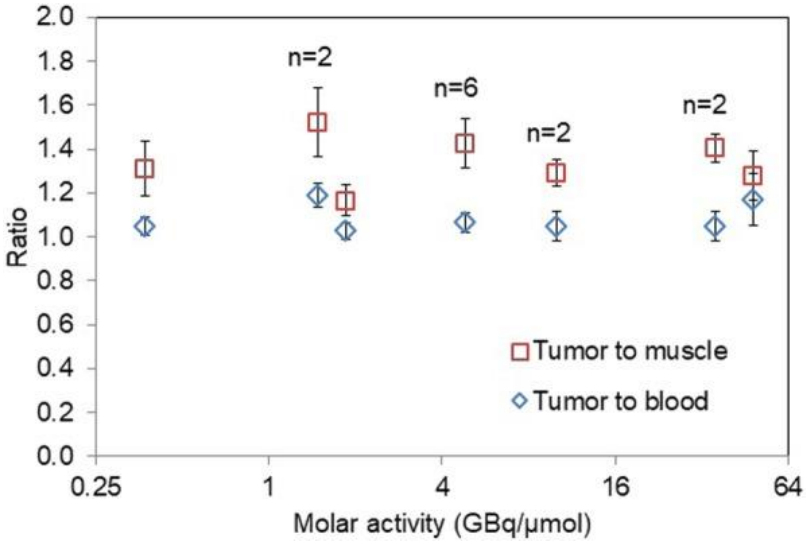

Figure 5.8. Tumor to muscle and tumor to blood ratios averaged for all tumors injected with [^{18}F]FET from the same molar activity group.

5.5 Highthroughput screening identifies CDK7 as an activator of glucose consumption

Increase in glucose consumption is a fundamental hallmark of most cancer. This phenomenon is either induced by oncogenes or from loss of tumor supressors and is exploited in the clinic to visualize with ^{18}F-FDG PET. Studies have shown that targeting glucose consumption can limit cancer growth and induce cell death. Currently, glucose consumption is targeted through the use of 2-DG (2-deoxyglucose), which is a glucose analogue that can act as a prodrug and be targeted by hexokinase, important enzymes in the glucose consumption pathway. However, 2-DG lack specificity and can lead to toxicity in patients and this limited the use of 2-DG clinically. Inhibitors that target GLUT transporters have shown promise but are not yet tested in patients. Different signaling pathways are use to regulate enzymes in cancer cells compared to non-transformed cells and targeting these specific enzymes can be a strategy to block cancer cell glucose consumption while sparing healthy cells. Currently, there are no high-throughput methods to study glucose consumption. Standard assays with isotopically labeled glucose or glucose analogues to quantify glucose consumption are low-throughout. In this study, Ghezzi et al. adapted and optimized a highthroughput luminescence-based glucose consumption assay that can be used to screen thousands of small molecule or genetic libraries. In the general overview of the assay, cells expressing blue fluorescent protein (BFP) are plated into the 384-well plates that contain either DMSO or small molecule in media. After a 24 hours incubation time, cells are washed with 1XPBS that contain 0.25% BSA and 2-DG is added. During a 20 minutes incubation period, cells are imaged with an automated fluorescent microscope imager and counted for BFP+ cells in each well. After

20 minutes, a stop buffer is added followed by a neutralization buffer and detection reagent. Luminescence is then measured on a plate reader (**Fig. 4.9**).

In the study, thousands of compounds were screened against non-small cell lung cancer cells using the high-throughput assay and they discovered that blocking CDK7 with Milciclib (one of the drug candidates in the high-throughput screening), blocked glucose consumption. The exact mechanisms of how blocking CDK7 with Milciclib which lead to decrease in glucose consumption was elucidated in this study. For my role in this study, I validated the inhibition of RNA polymerase II phosphorylation and activation when CDK7 is blocked using chromatin immunoprecipitation (ChIP). I confirmed that when CDK7 is inhibited by Milciclib, levels of phosphorylated subunit of RNA polymerase II that sits on the SLC2A1 promoter is decreased (**Fig. 4.10**). This explained the decrease in GLUT1 mRNA levels that Ghezzi et al. observed previously.

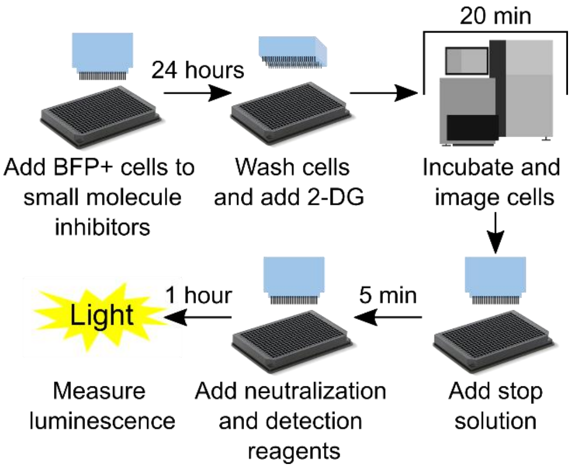

Figure 5.9. Scheme of luminescence-based high-throughput assay for measuring glucose consumption.

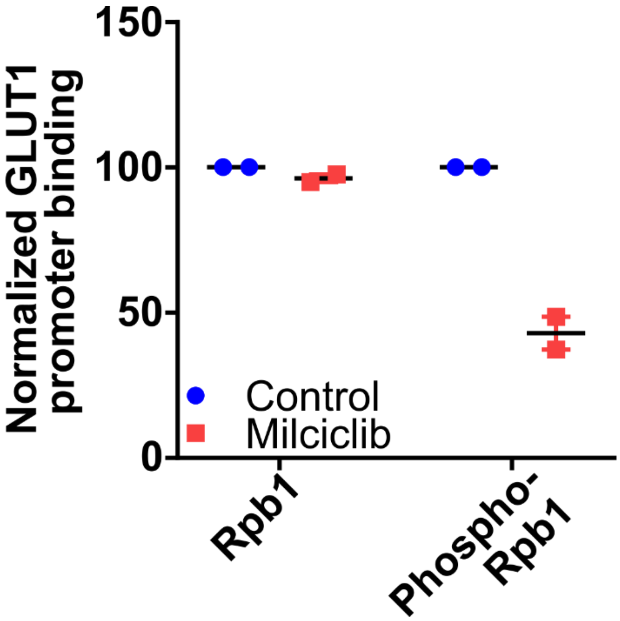

Figure 5.10. Rpb1 and phospho-Rpb1 levels on GLUT1 promoter in H460 cells treated with vehicle or Milciclib.

References

1. Wallin MT, Culpepper WJ, Campbell JD, et al. The prevalence of MS in the United States: A population-based estimate using health claims data. *Neurology*. 2019;92:e1029-e1040.

2. Greer JM, McCombe PA. Role of gender in multiple sclerosis: clinical effects and potential molecular mechanisms. *J Neuroimmunol*. 2011;234:7-18.

3. Yeshokumar AK, Narula S, Banwell B. Pediatric multiple sclerosis. *Curr Opin Neurol*. 2017;30:216-221.

4. Browne P, Chandraratna D, Angood C, et al. Atlas of Multiple Sclerosis 2013: A growing global problem with widespread inequity. *Neurology*. 2014;83:1022-1024.

5. Rosati G. The prevalence of multiple sclerosis in the world: an update. *Neurol Sci*. 2001;22:117-139.

6. Patsopoulos NA, Barcellos LF, Hintzen RQ, et al. Fine-mapping the genetic association of the major histocompatibility complex in multiple sclerosis: HLA and non-HLA effects. *PLoS Genet*. 2013;9:e1003926.

7. Munger KL, Bentzen J, Laursen B, et al. Childhood body mass index and multiple sclerosis risk: a long-term cohort study. *Mult Scler*. 2013;19:1323-1329.

8. Handel AE, Williamson AJ, Disanto G, Dobson R, Giovannoni G, Ramagopalan SV. Smoking and multiple sclerosis: an updated meta-analysis. *PLoS One*. 2011;6:e16149.

9. Handel AE, Williamson AJ, Disanto G, Handunnetthi L, Giovannoni G, Ramagopalan SV. An updated meta-analysis of risk of multiple sclerosis following infectious mononucleosis. *PLoS One*. 2010;5:e12496.

10. Runmarker B, Andersen O. Prognostic factors in a multiple sclerosis incidence cohort with twenty-five years of follow-up. *Brain*. 1993;116 (Pt 1):117-134.

11. Weinshenker BG, Rice GP, Noseworthy JH, Carriere W, Baskerville J, Ebers GC. The natural history of multiple sclerosis: a geographically based study. 3. Multivariate analysis of predictive factors and models of outcome. *Brain*. 1991;114 (Pt 2):1045-1056.

12. Brownlee WJ, Hardy TA, Fazekas F, Miller DH. Diagnosis of multiple sclerosis: progress and challenges. *Lancet*. 2017;389:1336-1346.

13. Lublin FD, Reingold SC, Cohen JA, et al. Defining the clinical course of multiple sclerosis: the 2013 revisions. *Neurology*. 2014;83:278-286.

14. Toosy AT, Mason DF, Miller DH. Optic neuritis. *Lancet Neurol*. 2014;13:83-99.

15. Petzold A, Wattjes MP, Costello F, et al. The investigation of acute optic neuritis: a review and proposed protocol. *Nat Rev Neurol*. 2014;10:447-458.

16. Galetta SL, Villoslada P, Levin N, et al. Acute optic neuritis: Unmet clinical needs and model for new therapies. *Neurol Neuroimmunol Neuroinflamm*. 2015;2:e135.

17. Gilmore CP, Donaldson I, Bö L, Owens T, Lowe J, Evangelou N. Regional variations in the extent and pattern of grey matter demyelination in multiple sclerosis: a comparison between the cerebral cortex, cerebellar cortex, deep grey matter nuclei and the spinal cord. *J Neurol Neurosurg Psychiatry*. 2009;80:182-187.

18. Green AJ, McQuaid S, Hauser SL, Allen IV, Lyness R. Ocular pathology in multiple sclerosis: retinal atrophy and inflammation irrespective of disease duration. *Brain*. 2010;133:1591-1601.

19. Petrova N, Carassiti D, Altmann DR, Baker D, Schmierer K. Axonal loss in the multiple sclerosis spinal cord revisited. *Brain Pathol*. 2018;28:334-348.

20. Frischer JM, Weigand SD, Guo Y, et al. Clinical and pathological insights into the dynamic nature of the white matter multiple sclerosis plaque. *Ann Neurol*. 2015;78:710-721.

21. Machado-Santos J, Saji E, Tröscher AR, et al. The compartmentalized inflammatory response in the multiple sclerosis brain is composed of tissue-resident CD8+ T lymphocytes and B cells. *Brain*. 2018;141:2066-2082.

22. Lassmann H, van Horssen J, Mahad D. Progressive multiple sclerosis: pathology and pathogenesis. *Nat Rev Neurol*. 2012;8:647-656.

23. Mahad DH, Trapp BD, Lassmann H. Pathological mechanisms in progressive multiple sclerosis. *Lancet Neurol*. 2015;14:183-193.

24. Prineas JW, Kwon EE, Cho ES, et al. Immunopathology of secondary-progressive multiple sclerosis. *Ann Neurol*. 2001;50:646-657.

25. Filippi M, Bar-Or A, Piehl F, et al. Multiple sclerosis. *Nat Rev Dis Primers*. 2018;4:43.

26. Ortiz GG, Pacheco-Moisés FP, Macías-Islas MÁ, et al. Role of the blood-brain barrier in multiple sclerosis. *Arch Med Res*. 2014;45:687-697.

27. Minagar A, Alexander JS. Blood-brain barrier disruption in multiple sclerosis. *Mult Scler*. 2003;9:540-549.

28. Frohman EM, Racke MK, Raine CS. Multiple sclerosis--the plaque and its pathogenesis. *N Engl J Med*. 2006;354:942-955.

29. Lucchinetti C, Brück W, Parisi J, Scheithauer B, Rodriguez M, Lassmann H. Heterogeneity of multiple sclerosis lesions: implications for the pathogenesis of demyelination. *Ann Neurol*. 2000;47:707-717.

30. Li R, Patterson KR, Bar-Or A. Reassessing B cell contributions in multiple sclerosis. *Nat Immunol*. 2018;19:696-707.

31. Dendrou CA, Fugger L, Friese MA. Immunopathology of multiple sclerosis. *Nat Rev Immunol*. 2015;15:545-558.

32. Kitz A, Singer E, Hafler D. Regulatory T Cells: From Discovery to Autoimmunity. *Cold Spring Harb Perspect Med*. 2018;8:a029041.

33. Hauser SL, Bar-Or A, Comi G, et al. Ocrelizumab versus Interferon Beta-1a in Relapsing Multiple Sclerosis. *N Engl J Med*. 2017;376:221-234.

34. Cross AH, Stark JL, Lauber J, Ramsbottom MJ, Lyons J-A. Rituximab reduces B cells and T cells in cerebrospinal fluid of multiple sclerosis patients. *J Neuroimmunol*. 2006;180:63-70.

35. Monson NL, Cravens PD, Frohman EM, Hawker K, Racke MK. Effect of rituximab on the peripheral blood and cerebrospinal fluid B cells in patients with primary progressive multiple sclerosis. *Arch Neurol*. 2005;62:258-264.

36. Bar-Or A, Fawaz L, Fan B, et al. Abnormal B-cell cytokine responses a trigger of T-cell-mediated disease in MS? *Ann Neurol*. 2010;67:452-461.

37. Li R, Rezk A, Miyazaki Y, et al. Proinflammatory GM-CSF-producing B cells in multiple sclerosis and B cell depletion therapy. *Sci Transl Med*. 2015;7:310ra166.

38. Barr TA, Shen P, Brown S, et al. B cell depletion therapy ameliorates autoimmune disease through ablation of IL-6-producing B cells. *J Exp Med*. 2012;209:1001-1010.

39. Bjornevik K, Cortese M, Healy BC, et al. Longitudinal analysis reveals high prevalence of Epstein-Barr virus associated with multiple sclerosis. *Science*. 2022;375:296-301.

40. Lanz TV, Brewer RC, Ho PP, et al. Clonally Expanded B Cells in Multiple Sclerosis Bind EBV EBNA1 and GlialCAM. *Nature*. January 2022.

41. van Waesberghe JH, Kamphorst W, De Groot CJ, et al. Axonal loss in multiple sclerosis lesions: magnetic resonance imaging insights into substrates of disability. *Ann Neurol*. 1999;46:747-754.

42. Jakimovski D, Kolb C, Ramanathan M, Zivadinov R, Weinstock-Guttman B. Interferon β for Multiple Sclerosis. *Cold Spring Harb Perspect Med*. 2018;8:a032003.

43. Aharoni R. The mechanism of action of glatiramer acetate in multiple sclerosis and beyond. *Autoimmun Rev*. 2013;12:543-553.

44. Rae-Grant A, Day GS, Marrie RA, et al. Practice guideline recommendations summary: Disease-modifying therapies for adults with multiple sclerosis: Report of the Guideline Development, Dissemination, and Implementation Subcommittee of the American Academy of Neurology. *Neurology*. 2018;90:777-788.

45. Muraro PA, Pasquini M, Atkins HL, et al. Long-term Outcomes After Autologous Hematopoietic Stem Cell Transplantation for Multiple Sclerosis. *JAMA Neurol*. 2017;74:459-469.

46. Comi G, Radaelli M, Soelberg Sørensen P. Evolving concepts in the treatment of relapsing multiple sclerosis. *Lancet*. 2017;389:1347-1356.

47. Phelps ME. Positron emission tomography provides molecular imaging of biological processes. *Proc Natl Acad Sci U S A*. 2000;97:9226-9233.

48. Trapp BD, Stys PK. Virtual hypoxia and chronic necrosis of demyelinated axons in multiple sclerosis. *Lancet Neurol*. 2009;8:280-291.

49. Banati RB, Newcombe J, Gunn RN, et al. The peripheral benzodiazepine binding site in the brain in multiple sclerosis: quantitative in vivo imaging of microglia as a measure of disease activity. *Brain*. 2000;123 (Pt 11):2321-2337.

50. Nutma E, Stephenson JA, Gorter RP, et al. A quantitative neuropathological assessment of translocator protein expression in multiple sclerosis. *Brain*. 2019;142:3440-3455.

51. Singhal T, O’Connor K, Dubey S, et al. 18F-PBR06 Versus 11C-PBR28 PET for Assessing White Matter Translocator Protein Binding in Multiple Sclerosis. *Clin Nucl Med*. 2018;43:e289-e295.

52. Singhal T, O’Connor K, Dubey S, et al. Gray matter microglial activation in relapsing vs progressive MS: A [F-18]PBR06-PET study. *Neurol Neuroimmunol Neuroinflamm*. 2019;6:e587.

53. Politis M, Giannetti P, Su P, et al. Increased PK11195 PET binding in the cortex of patients with MS correlates with disability. *Neurology*. 2012;79:523-530.

54. Giannetti P, Politis M, Su P, et al. Increased PK11195-PET binding in normal-appearing white matter in clinically isolated syndrome. *Brain*. 2015;138:110-119.

55. Rissanen E, Tuisku J, Rokka J, et al. In Vivo Detection of Diffuse Inflammation in Secondary Progressive Multiple Sclerosis Using PET Imaging and the Radioligand ^{11}C-PK11195. *J Nucl Med*. 2014;55:939-944.

56. Hagens MHJ, Golla SV, Wijburg MT, et al. In vivo assessment of neuroinflammation in progressive multiple sclerosis: a proof of concept study with [18F]DPA714 PET. *J Neuroinflammation*. 2018;15:314.

57. Datta G, Colasanti A, Rabiner EA, et al. Neuroinflammation and its relationship to changes in brain volume and white matter lesions in multiple sclerosis. *Brain*. 2017;140:2927-2938.

58. Sucksdorff M, Matilainen M, Tuisku J, et al. Brain TSPO-PET predicts later disease progression independent of relapses in multiple sclerosis. *Brain*. 2020;143:3318-3330.

59. James ML, Hoehne A, Mayer AT, et al. Imaging B Cells in a Mouse Model of Multiple Sclerosis Using 64Cu-Rituximab PET. *J Nucl Med*. 2017;58:1845-1851.

60. Linnerbauer M, Wheeler MA, Quintana FJ. Astrocyte Crosstalk in CNS Inflammation. *Neuron*. 2020;108:608-622.

61. Takata K, Kato H, Shimosegawa E, et al. 11C-acetate PET imaging in patients with multiple sclerosis. *PLoS One*. 2014;9:e111598.

62. Kato H, Okuno T, Isohashi K, et al. Astrocyte metabolism in multiple sclerosis investigated by 1-C-11 acetate PET. *J Cereb Blood Flow Metab*. 2021;41:369-379.

63. Ishibashi K, Miura Y, Hirata K, Toyohara J, Ishii K. 18F-THK5351 PET Can Identify Astrogliosis in Multiple Sclerosis Plaques. *Clin Nucl Med*. 2020;45:e98-e100.

64. Ishibashi K, Kameyama M, Miura Y, Toyohara J, Ishii K. Head-to-Head Comparison of the Two MAO-B Radioligands, 18F-THK5351 and 11C-L-Deprenyl, to Visualize Astrogliosis in Patients With Neurological Disorders. *Clin Nucl Med*. 2021;46:e31-e33.

65. Rissanen E, Virta JR, Paavilainen T, et al. Adenosine A2A receptors in secondary progressive multiple sclerosis: a [(11)C]TMSX brain PET study. *J Cereb Blood Flow Metab*. 2013;33:1394-1401.

66. Tyacke RJ, Myers JFM, Venkataraman A, et al. Evaluation of 11C-BU99008, a PET Ligand for the Imidazoline2 Binding Site in Human Brain. *J Nucl Med*. 2018;59:1597-1602.

67. Stankoff B, Wang Y, Bottlaender M, et al. Imaging of CNS myelin by positron-emission tomography. *Proc Natl Acad Sci U S A*. 2006;103:9304-9309.

68. Wu C, Wang C, Popescu DC, et al. A novel PET marker for in vivo quantification of myelination. *Bioorg Med Chem*. 2010;18:8592-8599.

69. Wu C, Zhu J, Baeslack J, et al. Longitudinal positron emission tomography imaging for monitoring myelin repair in the spinal cord. *Ann Neurol*. 2013;74:688-698.

70. Bajaj A, LaPlante NE, Cotero VE, et al. Identification of the protein target of myelin-binding ligands by immunohistochemistry and biochemical analyses. *J Histochem Cytochem*. 2013;61:19-30.

71. Faria D de P, Copray S, Sijbesma JWA, et al. PET imaging of focal demyelination and remyelination in a rat model of multiple sclerosis: comparison of [11C]MeDAS, [11C]CIC and [11C]PIB. *Eur J Nucl Med Mol Imaging*. 2014;41:995-1003.

72. Auvity S, Tonietto M, Caillé F, et al. Repurposing radiotracers for myelin imaging: a study comparing 18F-florbetaben, 18F-florbetapir, 18F-flutemetamol,11C-MeDAS, and 11C-PiB. *Eur J Nucl Med Mol Imaging*. 2020;47:490-501.

73. Roelcke U, Kappos L, Lechner-Scott J, et al. Reduced glucose metabolism in the frontal cortex and basal ganglia of multiple sclerosis patients with fatigue: a 18F-fluorodeoxyglucose positron emission tomography study. *Neurology*. 1997;48:1566-1571.

74. Blinkenberg M, Rune K, Jensen CV, et al. Cortical cerebral metabolism correlates with MRI lesion load and cognitive dysfunction in MS. *Neurology*. 2000;54:558-564.

75. Freeman L, Garcia-Lorenzo D, Bottin L, et al. The neuronal component of gray matter damage in multiple sclerosis: A [(11) C]flumazenil positron emission tomography study. *Ann Neurol*. 2015;78:554-567.

76. Finnema SJ, Nabulsi NB, Eid T, et al. Imaging synaptic density in the living human brain. *Sci Transl Med*. 2016;8:348ra96.

77. Mansur A, Rabiner EA, Tsukada H, et al. Test-retest variability and reference region-based quantification of 18F-BCPP-EF for imaging mitochondrial complex I in the human brain. *J Cereb Blood Flow Metab*. 2021;41:771-779.

78. Reichard P. Interactions between deoxyribonucleotide and DNA synthesis. *Annu Rev Biochem*. 1988;57:349-374.

79. Yamamura T, Narumi K, Ohata T, et al. Characterization of deoxyribonucleoside transport mediated by concentrative nucleoside transporters. *Biochem Biophys Res Commun*. 2021;558:120-125.

80. Vickers MF, Kumar R, Visser F, et al. Comparison of the interaction of uridine, cytidine, and other pyrimidine nucleoside analogues with recombinant human equilibrative nucleoside transporter 2 (hENT2) produced in Saccharomyces cerevisiae. *Biochem Cell Biol*. 2002;80:639-644.

81. Toy G, Austin WR, Liao H-I, et al. Requirement for deoxycytidine kinase in T and B lymphocyte development. *Proc Natl Acad Sci U S A*. 2010;107:5551-5556.

82. Eriksson S, Munch-Petersen B, Johansson K, Eklund H. Structure and function of cellular deoxyribonucleoside kinases. *Cell Mol Life Sci*. 2002;59:1327-1346.

83. Saiki Y, Yoshino Y, Fujimura H, et al. DCK is frequently inactivated in acquired gemcitabine-resistant human cancer cells. *Biochem Biophys Res Commun*. 2012;421:98-104.

84. Lotfi K, Juliusson G, Albertioni F. Pharmacological basis for cladribine resistance. *Leuk Lymphoma*. 2003;44:1705-1712.

85. Bunimovich YL, Nair-Gill E, Riedinger M, et al. Deoxycytidine kinase augments ATM-Mediated DNA repair and contributes to radiation resistance. *PLoS One*. 2014;9:e104125.

86. Yang C, Lee M, Hao J, et al. Deoxycytidine kinase regulates the G2/M checkpoint through interaction with cyclin-dependent kinase 1 in response to DNA damage. *Nucleic Acids Research*. 2012;40:9621-9632.

87. Nyhan WL. Disorders of purine and pyrimidine metabolism. *Mol Genet Metab*. 2005;86:25-33.

88. Giblett ER, Anderson JE, Cohen F, Pollara B, Meuwissen HJ. Adenosine-deaminase deficiency in two patients with severely impaired cellular immunity. *Lancet*. 1972;2:1067-1069.

89. Giblett ER. ADA and PNP deficiencies: how it all began. *Ann N Y Acad Sci*. 1985;451:1-8.

90. Griffith DA, Jarvis SM. Nucleoside and nucleobase transport systems of mammalian cells. *Biochim Biophys Acta*. 1996;1286:153-181.

91. Nair-Gill E, Wiltzius SM, Wei XX, et al. PET probes for distinct metabolic pathways have different cell specificities during immune responses in mice. *J Clin Invest*. 2010;120:2005-2015.

92. Austin WR, Armijo AL, Campbell DO, et al. Nucleoside salvage pathway kinases regulate hematopoiesis by linking nucleotide metabolism with replication stress. *J Exp Med*. 2012;209:2215-2228.

93. Salas JR, Chen BY, Wong A, et al. 18F-FAC PET Selectively Images Liver-Infiltrating CD4 and CD8 T Cells in a Mouse Model of Autoimmune Hepatitis. *J Nucl Med*. 2018;59:1616-1623.

94. Radu CG, Shu CJ, Nair-Gill E, et al. Molecular imaging of lymphoid organs and immune activation by positron emission tomography with a new [18F]-labeled 2'-deoxycytidine analog. *Nat Med*. 2008;14:783-788.

95. Brewer S, Nair-Gill E, Wei B, et al. Epithelial uptake of [18F]1-(2'-deoxy-2'-arabinofuranosyl) cytosine indicates intestinal inflammation in mice. *Gastroenterology*. 2010;138:1266-1275.

96. Ho DH. Distribution of kinase and deaminase of 1-beta-D-arabinofuranosylcytosine in tissues of man and mouse. *Cancer Res*. 1973;33:2816-2820.

97. Kim W, Le TM, Wei L, et al. [18F]CFA as a clinically translatable probe for PET imaging of deoxycytidine kinase activity. *Proc Natl Acad Sci U S A*. 2016;113:4027-4032.

98. Compston A, Coles A. Multiple sclerosis. *Lancet*. 2008;372:1502-1517.

99. Traugott U, Reinherz EL, Raine CS. Multiple sclerosis: distribution of T cell subsets within active chronic lesions. *Science*. 1983;219:308-310.

100. Wingerchuk DM, Carter JL. Multiple sclerosis: current and emerging disease-modifying therapies and treatment strategies. *Mayo Clin Proc*. 2014;89:225-240.

101. Bai R, Gao H, Han Z, et al. Long-Term Kinetics of Immunologic Components and Neurological Deficits in Rats Following Repetitive Mild Traumatic Brain Injury. *Med Sci Monit*. 2017;23:1707-1718.

102. Ertürk A, Mentz S, Stout EE, et al. Interfering with the Chronic Immune Response Rescues Chronic Degeneration After Traumatic Brain Injury. *J Neurosci*. 2016;36:9962-9975.

103. Brochard V, Combadière B, Prigent A, et al. Infiltration of CD4+ lymphocytes into the brain contributes to neurodegeneration in a mouse model of Parkinson disease. *J Clin Invest*. 2009;119:182-192.

104. Laurent C, Dorothée G, Hunot S, et al. Hippocampal T cell infiltration promotes neuroinflammation and cognitive decline in a mouse model of tauopathy. *Brain*. 2017;140:184-200.

105. Dong T, Zhi L, Bhayana B, Wu MX. Cortisol-induced immune suppression by a blockade of lymphocyte egress in traumatic brain injury. *J Neuroinflammation*. 2016;13:197.

106. Yilmaz G, Arumugam TV, Stokes KY, Granger DN. Role of T lymphocytes and interferon-gamma in ischemic stroke. *Circulation*. 2006;113:2105-2112.

107. Grønberg NV, Johansen FF, Kristiansen U, Hasseldam H. Leukocyte infiltration in experimental stroke. *J Neuroinflammation*. 2013;10:115.

108. Varvel NH, Neher JJ, Bosch A, et al. Infiltrating monocytes promote brain inflammation and exacerbate neuronal damage after status epilepticus. *Proc Natl Acad Sci U S A*. 2016;113:E5665-5674.

109. Airas L, Dickens AM, Elo P, et al. In vivo PET imaging demonstrates diminished microglial activation after fingolimod treatment in an animal model of multiple sclerosis. *J Nucl Med*. 2015;56:305-310.

110. Unterrainer M, Mahler C, Vomacka L, et al. TSPO PET with [18F]GE-180 sensitively detects focal neuroinflammation in patients with relapsing-remitting multiple sclerosis. *Eur J Nucl Med Mol Imaging*. 2018;45:1423-1431.

111. Radu CG, Shu CJ, Shelly SM, Phelps ME, Witte ON. Positron emission tomography with computed tomography imaging of neuroinflammation in experimental autoimmune encephalomyelitis. *Proceedings of the National Academy of Sciences*. 2007;104:1937-1942.

112. Gerwien H, Hermann S, Zhang X, et al. Imaging matrix metalloproteinase activity in multiple sclerosis as a specific marker of leukocyte penetration of the blood-brain barrier. *Sci Transl Med*. 2016;8:364ra152.

113. Miller SD, Karpus WJ. Experimental autoimmune encephalomyelitis in the mouse. *Curr Protoc Immunol*. 2007;Chapter 15:Unit 15.1.

114. Fedchenko N, Reifenrath J. Different approaches for interpretation and reporting of immunohistochemistry analysis results in the bone tissue - a review. *Diagn Pathol*. 2014;9:221.

115. Ma Y, Hof PR, Grant SC, et al. A three-dimensional digital atlas database of the adult C57BL/6J mouse brain by magnetic resonance microscopy. *Neuroscience*. 2005;135:1203-1215.

116. Loening AM, Gambhir SS. AMIDE: a free software tool for multimodality medical image analysis. *Mol Imaging*. 2003;2:131-137.

117. Salas JR, Chen BY, Wong A, et al. Noninvasive Imaging of Drug-Induced Liver Injury with 18F-DFA PET. *J Nucl Med*. 2018;59:1308-1315.

118. LaFrance-Corey RG, Howe CL. Isolation of brain-infiltrating leukocytes. *J Vis Exp*. 2011:2747.

119. Cansev M. Uridine and cytidine in the brain: their transport and utilization. *Brain Res Rev*. 2006;52:389-397.

120. Dai H, Marbach P, Lemaire M, Hayes M, Elmquist WF. Distribution of STI-571 to the brain is limited by P-glycoprotein-mediated efflux. *J Pharmacol Exp Ther*. 2003;304:1085-1092.

121. Pike VW. PET radiotracers: crossing the blood-brain barrier and surviving metabolism. *Trends Pharmacol Sci*. 2009;30:431-440.

122. Brown DA, Sawchenko PE. Time course and distribution of inflammatory and neurodegenerative events suggest structural bases for the pathogenesis of experimental autoimmune encephalomyelitis. *J Comp Neurol*. 2007;502:236-260.

123. Schmitt C, Strazielle N, Ghersi-Egea J-F. Brain leukocyte infiltration initiated by peripheral inflammation or experimental autoimmune encephalomyelitis occurs through pathways connected to the CSF-filled compartments of the forebrain and midbrain. *J Neuroinflammation*. 2012;9:187.

124. Bennett J, Basivireddy J, Kollar A, et al. Blood-brain barrier disruption and enhanced vascular permeability in the multiple sclerosis model EAE. *J Neuroimmunol*. 2010;229:180-191.

125. Cohen JA, Chun J. Mechanisms of fingolimod's efficacy and adverse effects in multiple sclerosis. *Ann Neurol*. 2011;69:759-777.

126. Shu CJ, Campbell DO, Lee JT, et al. Novel PET probes specific for deoxycytidine kinase. *J Nucl Med*. 2010;51:1092-1098.

127. Schwarzenberg J, Radu CG, Benz M, et al. Human biodistribution and radiation dosimetry of novel PET probes targeting the deoxyribonucleoside salvage pathway. *Eur J Nucl Med Mol Imaging*. 2011;38:711-721.

128. Engvall C, Ryding E, Wirestam R, et al. Human cerebral blood volume (CBV) measured by dynamic susceptibility contrast MRI and 99mTc-RBC SPECT. *J Neurosurg Anesthesiol*. 2008;20:41-44.

129. Barrio MJ, Spick C, Radu CG, et al. Human Biodistribution and Radiation Dosimetry of 18F-Clofarabine, a PET Probe Targeting the Deoxyribonucleoside Salvage Pathway. *J Nucl Med*. 2017;58:374-378.

130. Murphy JM, Armijo AL, Nomme J, et al. Development of new deoxycytidine kinase inhibitors and noninvasive in vivo evaluation using positron emission tomography. *J Med Chem*. 2013;56:6696-6708.

131. Calabresi PA, Radue E-W, Goodin D, et al. Safety and efficacy of fingolimod in patients with relapsing-remitting multiple sclerosis (FREEDOMS II): a double-blind, randomised, placebo-controlled, phase 3 trial. *Lancet Neurol*. 2014;13:545-556.

132. Thompson AJ, Baranzini SE, Geurts J, Hemmer B, Ciccarelli O. Multiple sclerosis. *The Lancet*. 2018;391:1622-1636.

133. Baecher-Allan C, Kaskow BJ, Weiner HL. Multiple Sclerosis: Mechanisms and Immunotherapy. *Neuron*. 2018;97:742-768.

134. Reich DS, Lucchinetti CF, Calabresi PA. Multiple Sclerosis. *N Engl J Med*. 2018;378:169-180.

135. Chen BY, Ghezzi C, Villegas B, et al. 18F-FAC PET Visualizes Brain-Infiltrating Leukocytes in a Mouse Model of Multiple Sclerosis. *J Nucl Med*. 2020;61:757-763.

136. Tsang JE, Urner LM, Kim G, et al. Development of a Potent Brain-Penetrant EGFR Tyrosine Kinase Inhibitor against Malignant Brain Tumors. *ACS Med Chem Lett*. 2020;11:1799-1809.

137. Fox JJ, Navarro HI, Hashimoto T, Garcia AJ, Goldstein AS. Mass cytometry reveals species-specific differences and a new level of complexity for immune cells in the prostate. *Am J Clin Exp Urol*. 2019;7:281-296.

138. Glatigny S, Bettelli E. Experimental Autoimmune Encephalomyelitis (EAE) as Animal Models of Multiple Sclerosis (MS). *Cold Spring Harb Perspect Med*. 2018;8:a028977.

139. Lyons JA, San M, Happ MP, Cross AH. B cells are critical to induction of experimental allergic encephalomyelitis by protein but not by a short encephalitogenic peptide. *Eur J Immunol*. 1999;29:3432-3439.

140. Chen BY, Ghezzi C, Villegas B, et al. 18F-FAC PET Visualizes Brain-Infiltrating Leukocytes in a Mouse Model of Multiple Sclerosis. *J Nucl Med*. 2020;61:757-763.

141. Poddar S, Capparelli EV, Rosser EW, et al. Development and preclinical pharmacology of a novel dCK inhibitor, DI-87. *Biochem Pharmacol*. 2020;172:113742.

142. Glatigny S, Bettelli E. Experimental Autoimmune Encephalomyelitis (EAE) as Animal Models of Multiple Sclerosis (MS). *Cold Spring Harb Perspect Med*. 2018;8.

143. Leuenberger T, Paterka M, Reuter E, et al. The role of CD8+ T cells and their local interaction with CD4+ T cells in myelin oligodendrocyte glycoprotein35-55-induced experimental autoimmune encephalomyelitis. *J Immunol*. 2013;191:4960-4968.

144. Saligrama N, Zhao F, Sikora MJ, et al. Opposing T cell responses in experimental autoimmune encephalomyelitis. *Nature*. 2019;572:481-487.

145. Van Gassen S, Callebaut B, Van Helden MJ, et al. FlowSOM: Using self-organizing maps for visualization and interpretation of cytometry data. *Cytometry A*. 2015;87:636-645.

146. Tusher VG, Tibshirani R, Chu G. Significance analysis of microarrays applied to the ionizing radiation response. *Proc Natl Acad Sci U S A*. 2001;98:5116-5121.

147. Sakaguchi S, Yamaguchi T, Nomura T, Ono M. Regulatory T cells and immune tolerance. *Cell*. 2008;133:775-787.

148. Klotz L, Eschborn M, Lindner M, et al. Teriflunomide treatment for multiple sclerosis modulates T cell mitochondrial respiration with affinity-dependent effects. *Sci Transl Med*. 2019;11:eaao5563.

149. Wisitpitthaya S, Zhao Y, Long MJC, et al. Cladribine and Fludarabine Nucleotides Induce Distinct Hexamers Defining a Common Mode of Reversible RNR Inhibition. *ACS Chem Biol*. 2016;11:2021-2032.

150. Chang JT. Pathophysiology of Inflammatory Bowel Diseases. *N Engl J Med*. 2020;383:2652-2664.

151. Tsokos GC. Autoimmunity and organ damage in systemic lupus erythematosus. *Nat Immunol*. 2020;21:605-614.

152. Batts KP. Acute and chronic hepatic allograft rejection: pathology and classification. *Liver Transpl Surg*. 1999;5:S21-29.

153. Manns MP, Czaja AJ, Gorham JD, et al. Diagnosis and management of autoimmune hepatitis. *Hepatology*. 2010;51:2193-2213.

154. Tiegs G, Hentschel J, Wendel A. A T cell-dependent experimental liver injury in mice inducible by concanavalin A. *J Clin Invest*. 1992;90:196-203.

155. Blom KG, Qazi MR, Matos JBN, Nelson BD, DePierre JW, Abedi-Valugerdi M. Isolation of murine intrahepatic immune cells employing a modified procedure for mechanical disruption and functional characterization of the B, T and natural killer T cells obtained. *Clin Exp Immunol*. 2009;155:320-329.

156. Clark PM, Flores G, Evdokimov NM, et al. Positron emission tomography probe demonstrates a striking concentration of ribose salvage in the liver. *Proc Natl Acad Sci U S A*. 2014;111:E2866-2874.

157. Evdokimov NM, Clark PM, Flores G, et al. Development of 2-Deoxy-2-[(18)F]fluororibose for Positron Emission Tomography Imaging Liver Function in Vivo. *J Med Chem*. 2015;58:5538-5547.

158. Macintyre AN, Gerriets VA, Nichols AG, et al. The glucose transporter Glut1 is selectively essential for CD4 T cell activation and effector function. *Cell Metab*. 2014;20:61-72.

159. Sergeev ME, Lazari M, Morgia F, et al. Performing radiosynthesis in microvolumes to maximize molar activity of tracers for positron emission tomography. *Commun Chem*. 2018;1:10.